ABSTRACT

KIM, SUNGJIN. Real-time characterization of III-V compound semiconductor epitaxy: application to '6.1' materials. (Under the direction of David E. Aspnes)

The antimonides are potentially highly useful materials for low-power electronic-device applications. However, unlike P and As the volatility of Sb is very low, comparable to that of Al and Ga. As a result surface stoichiometry during growth cannot be controlled simply by heating, which can result in defective material.

The objective of this work is to determine whether real-time optical diagnostics, specifically spectroscopic ellipsometry (SE) and reflectance-difference spectroscopy (RDS) can resolve this problem. We found SE to be essential, not only for reproducibly growing high-quality GaSb but also for obtaining new information about growth mechanisms. The SE data revealed that decomposition of the Sb precursor, trimethylantimony, was self-limiting in contrast to the Ga precursor, trimethylgallium. We also showed that laser light scattering (LLS) could provide the information necessary to optimize V/III flow ratios. This work represents the first uses of SE for real-time studies of antimonide growth and of LLS for real-time optimization of growth processes.

The SE data also showed the presence of crystalline GaSb during the earliest stages (first 10 s) of GaSb growth, revealing that the heteroepitaxial growth of GaSb on GaAs proceeds as a physical mixture of separate islands of GaAs and GaSb, in contrast to the expected mixing on the atomic-scale. All other post-deposition characterizations (AFM, SEM, XRD, TEM, and conductivity measurements) supported the information that the real-time optical data (SE, RDS, and LLS) revealed.

Real-time characterization of III-V compound semiconductor epitaxy: application to '6.1' materials

Sungjin Kim

A dissertation submitted to the Graduate Faculty of North Carolina State University in partial fulfillment of the requirements for the Degree of Doctor of Philosophy

Materials Science and Engineering

Raleigh, NC

May 2004

APPROVED BY

Gregory N. Parsons

Nadia A. El-Masry

George A. Rozgonyi
Co-Chair

David E. Aspnes
Chair

DEDICATION

In memory of my late mother and

To all my families as well

BIOGRAPHY

The author, Sungjin Kim, was born in Korea and raised in a very rural area with two brothers and two sisters. He married Sangeun Yun and has two children, Anica and Samuel. His good friend, Mr. John French, director of NC State University Club, sponsored him to be a certified USPTA tennis teaching professional. The author will not soon forget the Saturday Morning Tennis Training Program (SMTTP) that he established and managed for about 10 months for free.

He strongly believes that Jesus Christ is good even during the hard times when he is struggling, and envisions who he will be 10 years from now.

ACKNOWLEDGEMENTS

First of all, I am especially thankful to Dr. David Aspnes, who supervised, encouraged, and inspired me during my research here at North Carolina State University, and whom I respect from the bottom of my heart due to his integrity, his attitude towards his students, ,and eagerness towards research. Thanks also to co-chair Dr. Rozgonyi and to thesis committee members Drs. El-Masry, Parsons, and Hren, who all gave me valuable comments on my thesis. I would also like to thank Ms. Edna Deas for her competence in administrative matters.

I also give everlasting great thanks to my mother, who passed away 18 years ago from stomach cancer when she was just 46; to my father and stepmother, who are still farmers where I was born; and to my mother-in-law and father-in law, who is president of the Constitutional Court of Korea, who supported me mentally and financially. Special thanks are also given to my brothers and sisters, and my wife's sister and brothers' families.

I also owe a debt of gratitude to my colleagues at my lab: Mr. Muharrem Asar, Mr. Nick Stoute, Mr. Haijiang Pen, Mr. Eric Adles, Mr. In Kyo Kim, and former students Dr. Klaus Flock in Germany, Dr. Ji-Fuh Wang in Tennessee, and visiting scientist Dr. Jon Hansen in Norway.

I thank Mr. Jin-Soo Choi of UNID, who encouraged me when I worked at the chemical plant, and my colleagues at UNID. Thanks also to Profs. Shanefield and Sigel of Rutgers, Dr. Ludwik Kordas, Mr. Ji-Soo Park, Mr. Changwoong Chu, Dr. Sangmin Lee, and the Christian families, the White family, Mr. Terry Dover, Mr. Jim Wetterau and pastor, who supported me with prayer to God in depth.

Last but not least, I am very grateful for the considerable patience and support of my wife Sangeun, my daughter Anica, and my son Samuel during seven and half years in which we stayed in the U.S.

Raleigh, North Carolina, U.S.A

TABLE OF CONTENTS

List of Figures

List of Tables

Chapter 1 Introduction

In most semiconductors bandgaps range from nearly zero (InSb) to about 6 eV (AlN). Photons that have sufficient energy can excite electrons from the filled valence bands to the empty conduction bands. If the photon energy is less than the electronic bandgap but well above any phonon energies, the absorption coefficient of the material is zero or very small.

Optical techniques, for instance, spectroscopic ellipsometry (SE) and reflectance-difference spectroscopy (RDS), are highly attractive for investigating surfaces and interfaces of samples in as-prepared conditions because optical probes are noninvasive, nondestructive, and can function in any transparent ambient [1]. As a result the use of ellipsometry in semiconductor processing has been extensive and continues to grow. However, this growth has been mainly in off-line measurements. Real-time diagnostics for monitoring and ideally controlling material processing, especially of thin film growth, have been a challenge of many researchers so far. Yet real-time monitoring and control of each step in growth processes has enormous potential to advance materials science through the optimization of new materials and, in microelectronic and optoelectronic technologies, through the optimization of new processes for device fabrication. Some results have already been reported. SE has been used to successfully demonstrate sample-driven closed-loop feedback control of epilayer composition [2-4] including graded compositions[5], thicknesses[6, 7], growth rates[8], and sample temperatures[7].

In our group previous students have developed a combined multi-wavelength combined ellipsometer/reflectance difference spectrometer that is integrated in an organometallic chemical vapor deposition (OMCVD) system and can acquire and process 1024-pixel

spectral information from 240 to 830 nm at the rate of 4 per second. This instrument has been used to demonstrate sample-driven closed-loop feedback control of the composition of InGaP layers deposited epitaxially on GaAs.

The antimonides are a highly promising and potentially important semiconductor material. Antimonides have the smallest bandgaps of the III-V semiconductors, with values ranging from the GaSb value of 1.6 μm (0.73 eV) to the 11 μm (0.11 eV) value for indium thallium antimonide. Therefore, optoelectronic devices fabricated from these materials can cover much of the infra-red wavelength range[9], which is particularly important for gas sensing at the ppb level[1].

GaSb-based devices in particular are promising candidates for a variety of military and civil applications that require wavelengths in the 2~14 μm range for photonic devices such as lasers, detectors, and photovoltaic cells. Recently, GaSb-based LEDs and lasers have been demonstrated [9]. With its 0.73 eV bandgap GaSb is often referred to as an intermediate-gap semiconductor. Its favorable combination of a bandgap energetically just below the 1.5 μm wavelength important for photonics and low effective mass (a consequence of its low bandgap), which translates into high electron and hole mobilities, make GaSb an ideal candidate for high-speed optoelectronic applications. In addition, its lattice constant matches solid solutions of various ternary and quaternary III-V compounds with bandgaps covering the wide spectral range of ~0.3 to 1.58 eV[10].

Subekti et al.[11] found that the optical and electrical properties of GaSb depend strongly on growth conditions. GaSb epilayers were grown on GaAs (lattice mismatch with GaSb; 7.83%) substrate in a vertical rotating disk OMCVD reactor operated at 60 Torr for

various growth temperatures, ranging from 550 to 570°C. The morphology of GaSb layers is extremely sensitive to the V/III ratio[12], as previously reported[13].

Among antimonides, GaSb is the most widely studied[14, 15]. It is known that Sb is non-volatile in contrast to P and As, which makes us to grow GaSb successfully.[9, 16-21] Thus the composition of epitaxially grown GaSb is in principle not self-regulating but can be affected by accumulated Ga or Sb resulting in nonstoichometry. Since the vapor pressure of Sb is much lower that of either or P, too high an Sb partial pressure may result in the formation of a second condensed phase, metallic Sb droplets on the surface. The group III metals are also not soluble in the semiconductor so any excess metal on the surface will also appear as second phase [22]. The presence of a second phase for Sb deposited on GaAs was recently demonstrated by Pitts et al. [23]using reflectance difference spectroscopy (RDS). On the other hand, if the V/III ratio is too low, then Ga droplets result [24]. Thus to grow stoichiometric GaSb by MBE the effusion rates of Ga and Sb must be controlled very carefully, nominally to parts in 10^4, and the same is expected for OMCVD. Haywood et al. [25]reported good morphologies for substrate temperatures of 550 and 600°C with near-unity V/III ratios using TMGa and TMSb.

At present, GaSb technology is in its infancy and significant progress has to be made both in materials growth and processing aspects before it can be employed for device applications [26]. Pitts et al. [23] showed with reflectance difference spectroscopy (RDS) that the vapor pressure of Sb is very low so that Sb atoms remain on the GaAs surface.

Our method of choice for GaSb on GaAs and GaSb is organometallic chemical vapor deposition (OMCVD), also known as MOCVD (metalorganic chemical vapor deposition) and OMVPE (organometallic vapor phase epitaxy). An understanding of OMCVD growth

requires knowledge about the chemical reactions between the substrate surface and the atoms or molecules such as TMGa and TMSb, which are used as precursors. In addition, we need to understand the processes taking place on the surface, for instance, diffusion, nucleation, adsorption and desorption. The overall OMCVD process is a complex interplay between fluid mechanics, heat and mass transport, and gas-phase and surface chemical reactions. Understanding, modeling, and controlling this interplay in typical OMCVD reactors is exceedingly difficult[27]. This means that despite its capabilities for epitaxial growth, OMCVD is not well understood. At least part of this lack of understanding has been the lack of any diagnostic tool that could obtain information in the OMCVD growth environment.

With respect to OMCVD mechanisms, Stringfellow[24],Moon [28], Aardvark et al[9], and Breiland et al [27] all provide good explanations, including brief looks at the origins of OMVPE and the early OMVPE history relative to compound semiconductors. Oleander [29] first suggests the use of rotating disks for better uniform deposition in chemical vapor deposition. Frolov et al [30] report in the OMCVD growth of GaAs using TMGa and AsH_3 that rotation of the pedestal on which the substrate sits increases the growth rate. Since this would decrease the thickness of the mass transport boundary layer, this finding is also consistent with the hypothesis that the growth rate is limited by mass transport. Even though OMCVD is highly complex, it has emerged as a flexible and powerful synthesis technology for a wide range of epitaxial compound semiconductors.

The standard way, and in fact up to now the only way, of studying OMCVD growth of GaSb was to grow the samples then analyze them to support our optical data after growth by optical microscope, AFM, SEM,TEM, X-RD, AES. Here, for the first time we obtain SE data as a real-time probe. The broad spectral response and fast acquisition times of this

system make it ideal for studying growth. The addition of a laser light scattering (LLS) capability has proven to be useful in that it allows macroscopic surface roughness to be detected, which is not possible with either SE or RDS.

The remainder of the thesis is organized as follows. Chapter 2 provides the theoretical background used to draw conclusions about sample physical properties from optical data presented. Chapter 3 describes experimental details. Results and discussion are provided in Ch. 4. Finally, we summarize and present our conclusions in Ch. 5.

Chapter 2 Background and Summary

The purpose of this chapter is to provide a context for the techniques used and data presented. We begin with a discussion of optical techniques for analyzing thin film growth in Sec. 2.1. Next, we describe the optical response of semiconductors, which includes an overview of the linear optical response and its relation to electronic band structure and sample properties. The optical response of structured materials is described in Sec.2.2, followed by an overview of SE and RDS. In Sec.2.4 we review OMCVD.

2.1 Optical techniques for analyzing thin film growths

For characterization of growing surfaces during OMCVD, optical techniques such as ellipsometry or RDS have found widespread use since electron-beam techniques such as reflection high-energy electron diffraction (RHEED) cannot be used in non-ultra high vacuum environments. Optical reflection techniques are one way that growth surfaces can be accessed, including the near-surface region of growing materials. Further details are introduced in the following.

2.1.1 Classification

Optical techniques can be classified as specula and nonspecular, as indicated in the Table below. In our experiments we concentrate on spectroscopic ellipsometry and the non-normal version of RDS, since these provide direct information about the growth surfaces. Although nonspecular measurements have been used on occasion to assess crystal growth,

for the semiconductors that we are interested in here they are used mainly to assess material quality after growth and so are not of direct interest for real-time measurements.

Table 2.1. Optical measurements

Specular	Non-specular
Modulated reflectance: Electroreflectance (ER) Photoreflectance (PR) Reflectance Difference Spectroscopy (RDS)	Photoluminescence (PL) Photoluminescence Excitation Spectroscopy (PLE) Cathodoluminescence (CL) Photoconductivity (PC) Raman Scattering Thermal Wave
Ellipsometry: Single-wavelength Spectroscopic (SE)	
Transmittance / absorptance (mainly IR)	
Second-harnomic generation (SHG)	

2.1.2 Ellipsometry

Ellipsometry is a sensitive optical technique for investigating properties of surfaces, interfaces, thin films, and multiplayer stacks[31]. Ellipsometry is most commonly used to analyze thin films. Through the analysis of the change in polarization state of light that is reflected from the sample, ellipsometry yields information about layers that are thinner than the wavelength of the light itself, down to single atomic layers or less. In its simplest form linearly polarized light is generated by passing a beam through a polarizer, and then reflected

at oblique incidence from the surface under investigation. The reflected light is in general elliptically polarized. The shape and orientation of the ellipse depend on the angle of the incidence, the polarization state of the incident light, and the reflection properties of the sample. Fig. 2.1 [32] lists the most commonly used ellipsometric configurations.

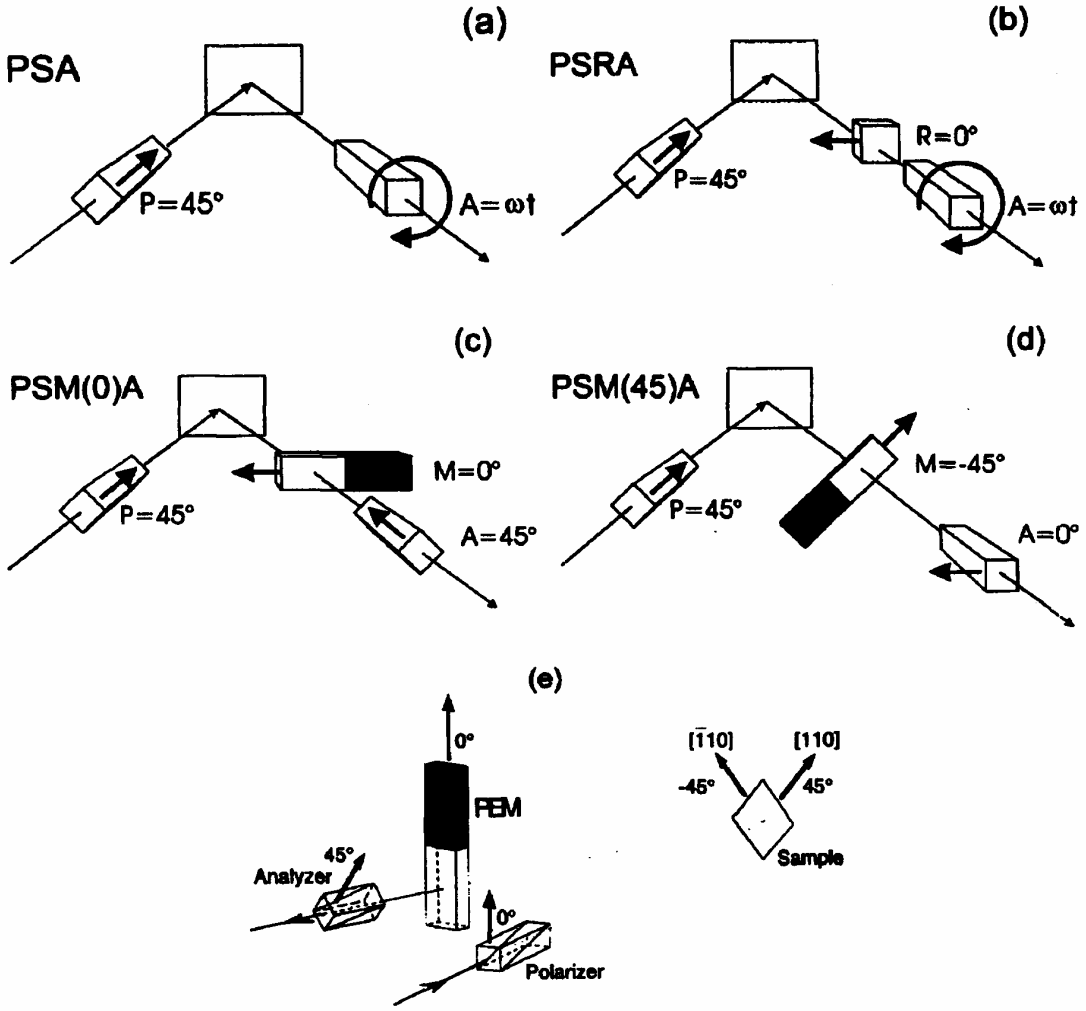

Figure 2.1. An overview over the basic types of ellipsometric configurations: (a) fixed Polarizer-Sample-rotating Analyzer (b) fixed Polarizer-Sample-fixed retarder-rotating-Analyzer (c) fixed Polarizer-Sample-PEM(0)-fixed Analyzer (d) fixed Polarizer-Sample-PEM(45)

An ellipsometer determines two ellipsometry angles, Ψ and Δ, which describe the change in the polarization state of the beam upon reflection from the sample. The ratio of the

amplitude of the polarization within the plane of incidence (P) to the amplitude of the polarization perpendicular to the plane of incidence (S) is represented by tanΨ. The difference in the phase changes upon reflection is Δ. Ψ and Δ essentially depend on the optical constants, n and k, of the layer materials and substrate, the physical thickness of the individual layers and the surface roughness. For a given material, the magnitude of the change in Ψ and Δ is different at different angles of incidence. A larger change gives more accurate results, and for this reason data tend to be taken at or near Brewster's angle, where the changes are largest.

Using the Jones matrix formalism, we can describe the operation of the ellipsometer in terms of the optical components and the Fresnel reflection coefficients r_p and r_s of the sample. For the SE configuration shown in Fig. 2.2, which consists of a fixed polarizer, sample, rotating compensator (PSCA), and fixed analyzer we have

$$\begin{pmatrix} E'_x \\ E'_y \end{pmatrix} = \begin{pmatrix} 1 & 0 \\ 0 & 0 \end{pmatrix} \begin{pmatrix} \cos A & \sin A \\ -\sin A & \cos A \end{pmatrix} \begin{pmatrix} \cos(\omega t - C) & -\sin(\omega t - C) \\ \sin(\omega t - C) & \cos(\omega t - C) \end{pmatrix} \begin{pmatrix} 1 & 0 \\ 0 & e^{-i\delta} \end{pmatrix} \begin{pmatrix} \cos(\omega t - C) & \sin(\omega t - C) \\ -\sin(\omega t - C) & \cos(\omega t - C) \end{pmatrix} \begin{pmatrix} r_p & 0 \\ 0 & r_s \end{pmatrix} \begin{pmatrix} \cos P & -\sin P \\ \sin P & \cos P \end{pmatrix} \begin{pmatrix} 1 & 0 \\ 0 & 0 \end{pmatrix} \begin{pmatrix} E_x \\ E_y \end{pmatrix} \quad (2.1)$$

where A and P define the analyzer and the polarizer angles, respectively, and C denotes the angle of the compensator fast axis measured with respect to the plane of incidence.

By multiplying the matrix out, evaluating the field at the detector, and taking the absolute square we obtain the transmitted intensity.

$$I(t) = I_{dc}\{(1 + \alpha_2 \cos 2(\omega t - C) + \beta_2 \sin 2(\omega t - C) + \alpha_4 \cos 4(\omega t - C) + \beta_4 \sin 4(\omega t - C)\} \quad (2.2)$$

where C is the reference azimuth of the compensator and ω is its mechanical rotation rate.

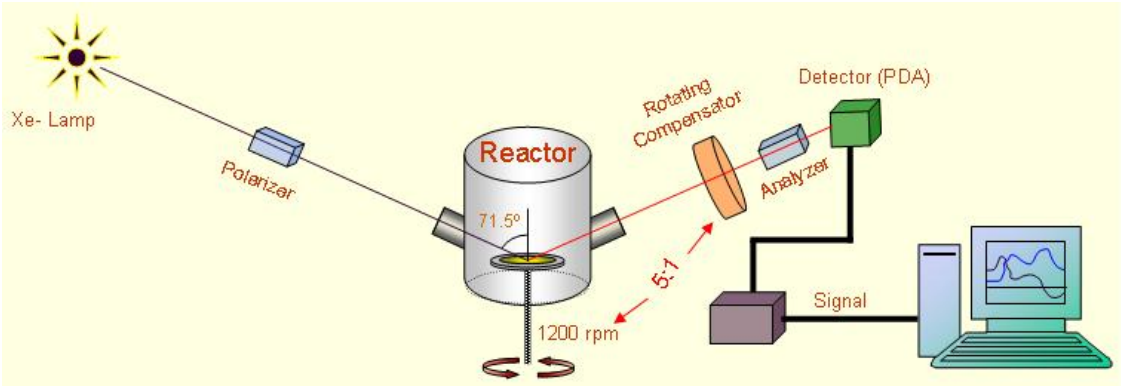

Figure 2.2. Schematic of the rotating-compensator multichannel spectroscopic ellipsometer

From the measured normalized coefficients we can derive ψ and Δ as follows:

$$Q = \frac{1}{2}\tan^{-1}\left(\frac{\beta_4}{\alpha_4}\right) - A \tag{2.3}$$

$$\chi = \frac{1}{2}\tan^{-1}\left[\frac{\alpha_2 \cos 2(A+Q)\tan(\frac{\delta}{2})}{2\alpha_4 \sin A}\right] \tag{2.4}$$

Therefore,

$$\cos 2\psi = \frac{\cos 2P - \cos 2Q \cos 2\chi}{1 - \cos 2Q \cos 2\chi \cos 2P} \tag{2.5}$$

$$\sin \Delta = \frac{\sin 2\chi(\cos 2\psi \cos 2P - 1)}{\sin 2\psi \sin 2P} \tag{2.6}$$

$$\cos \Delta = \frac{\cos 2\chi \cos 2Q(1 - \cos 2\psi \cos 2P)}{\sin 2\psi \sin 2P} \tag{2.7}$$

Since sinΔ and cosΔ are measured simultaneously it is not necessary to consider whether the sign of Δ is positive or not.

The result of the above calculation is the complex reflectance ratio ρ:

$$\rho = \frac{r_p}{r_s} = \tan\psi \exp^{i\Delta}. \qquad (2.8)$$

For a bare substrate we can connect this to the dielectric function ε of the substrate using the Fresnel equations. We find

$$\rho = \frac{r_p}{r_s} = \frac{\varepsilon_s}{\varepsilon_a} = \varepsilon = \sin^2\theta + \sin^2\theta \tan^2\theta \left(\frac{1-\rho}{1+\rho}\right)^2. \qquad (2.9)$$

ε is related to the complex refractive index by $\varepsilon = (n + ik)^2$ where $(n + ik)$ is the complex index of refraction. If the sample is covered with one or more ovelayers we can still use Eq. (2.9), but in this case we get what is called the pseudodielectric function <ε>. The concept of <ε> is best reserved for cases where the overlayers are very thin, as for example natural oxides or microscopic roughness. If the layer thicknesses are comparable to the wavelength of light, the sample must be modeled with the Fresnel reflectance equations, with each layer represented by its own dielectric function and thickness.

With a good model, n, k and the physical properties of the material can be determined by matching the modeled Ψ and Δ to the experimentally acquired Ψ and Δ from the unknown sample. In this way the technique can be routinely used for determining the properties of compounds of unknown composition, as well as the thickness of the individual layers in multilayer stacks.

2.1.2.1 Spectroscopic sllipsometer

Spectroscopic ellipsometry (SE) is a particularly useful form of ellipsometry because it can be used to determine the optical and physical properties of thin-film materials through their spectral responses as well as layer thicknesses through interference phenomena. SE is a non-contact technique that is also nondestructive, and can determine sample properties with

very good precision. This SE is an effective real time assessment technique. In SE the change in the polarization state of a beam of polarized light reflected from the sample being characterized is determined at many discrete wavelengths over a broad wavelength range, in our case from 1.5 to 6.0 eV. As with single-wavelength ellipsometry the change in the polarization state can be traced to the physical properties of the thin film by means of an optical model with the aid of regression analysis. SE has been used routinely for the characterization of already grown multilayer III-V compound semiconductor structures for many years.

SE instruments use a white light source, and individual wavelengths are selected for detection by either a motor-driven monochromator or a multichannel detector that can detect many wavelengths simultaneously. Increasing the number of angles of incidence and wavelengths at which data are acquired improves analysis precision, especially for complicated epitaxial structures. However the need to isolate the growth environment from the atmosphere requires the use of windows on the OMCVD growth chamber. Hence for the configuration used here we can obtain ellipsometric data only at a single angle of incidence.

2.1.2.2 Reflectance difference spectroscopy

Reflectance difference spectroscopy (RDS) is also an effective *in situ* technique of the surface reconstructions of compound semiconductors during growth by molecular beam epitaxy and organometallic chemical vapor deposition. RDS measures the relative difference in the near-normal-incidence reflectance of light polarized along the two principal axes of the surface [33]. RDS can also sense the relative surface concentrations of anion and cation dimer bonds and is therefore sensitive to the local electronic structure. This means that RDS is also sensitive to the elemental composition of the surface as well as to submonolayer

coverages of adsorbates[34]. Since the reflection probe senses optical anisotropy, RDS is also called reflectance anisotropy spectroscopy (RAS).

In isotropic materials like cubic semiconductors, the bulk is optically isotropic and hence the anisotropy arises entirely from the surface region. The surface anisotropy may arise from due to the different geometric ordering of atoms in two orthogonal directions parallel to the surface. The normalized reflectance-difference measurement is given by

$$\frac{\Delta r}{r} \equiv \frac{2(r_x - r_y)}{r_x + r_y} \tag{2.10}$$

where r_x and r_y are the complex reflectance of light polarized linearly along the indicated directions within the surface, for instance, for a (001) surface r_x and r_y become $r_{<\bar{1}10>}$ and $r_{<110>}$. Normally, the order of magnitude of the signal is about 10^{-3}, as indicated schematically below. Fig. 2.3 [35] shows a typical RD spectrometer used for crystal-growth measurements.

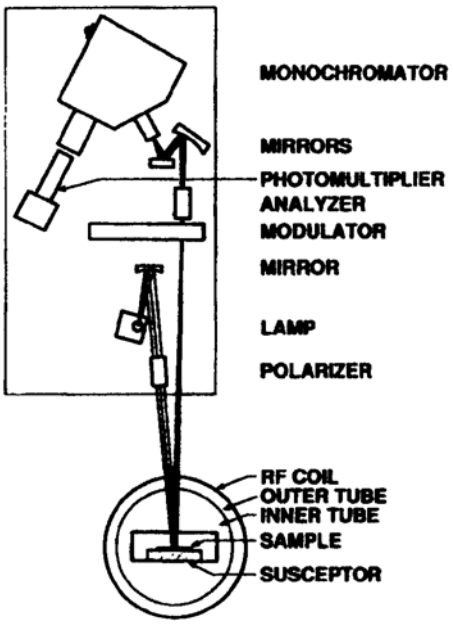

Figure 2.3. Schematic of typical RDS spectrometer.

In our bench system the optical beam is not normal to the surface but enters at an angle of approximately 2°. Although a connection between normal-incidence spectra can be made, by analogy to the normal-incidence situation we provide the data in the form of the quantity actually measured, which for our system with a 5:1 ratio for the rotation rates of the sample and compensator is the 10^{th} harmonic of the detected signal. Changes in this harmonic allow us to make inferences about the nature of the surface termination, which for III-V semiconductor growth surfaces usually consists of Group III or Group V dimmers.

In the ideal case the intensity reaching the photo diode array (PDA) from a rotating-compensator, rotating-sample spectroscopic polarimeter (RCSSP) synchronized at 5:1 ratio has the form

$$I = a_0 + a_2 \cos\omega t + b_2 \sin 2\omega t + a_4 \cos 4\omega t + b_4 \sin\omega t + a_{10} \cos 10\omega t + b_{10} \sin 10\omega t \quad (2.11)$$

where the normalized Fourier coefficients $\alpha_2 = \frac{a_2}{a_0}, \beta_2, \alpha_4$, and β_4 carry the information for calculating $< \varepsilon >$ and α_{10} and β_{10} provide information about sample anisotropy, which is mainly due to surface dimers.

2.2 Optical response of semiconductors

The features in optical spectra provide a rich source of information about the electronic properties of materials [36]. For semiconductors, much of this structure occurs in the quartz-optics spectral range, between 1.5 and 6.0 eV, which provides a convenient means of accessing this information. In this section, we briefly address the dielectric response of materials, the information accessible over the near-ir-near-uv spectral range, and the techniques used here to probe that information. This section will also give an overview of the

dielectric response and the relationship between the dielectric function and electronic band structure of cubic materials, including the influence of sample properties, such as temperature, composition, and strain.

2.2.1 Dielectric function and polarization

2.2.1.1 Dielectric function

The dielectric function is the response of a material to an electromagnetic field. The dielectric function depends sensitively on the electronic band structure of a crystal, and investigations of the dielectric function by optical spectroscopy are very useful in understanding the overall band structure of a crystal.

The topic begins with Maxwell's Equations, which describe propagation and also the boundary conditions for the electric and magnetic fields at each interface. In Gaussian units these equations are:

$$\nabla \cdot \vec{D} = 4\pi\rho \tag{2.12}$$

$$\nabla \cdot \vec{B} = 0 \tag{2.13}$$

$$\nabla \times \vec{E} = -\frac{1}{c}\frac{\partial \vec{B}}{\partial t} \tag{2.14}$$

$$\nabla \times \vec{H} = \frac{4\pi}{c}\vec{J} + \frac{1}{c}\frac{\partial \vec{D}}{\partial t} \tag{2.15}$$

where $\vec{D}, \vec{B}, \vec{E}, \rho,$ and $\vec{J}$ are the displacement field, magnetic induction, electric field, magnetic field intensity, charge density, and current density, respectively. In optics, the charge density ρ and the current density $\vec{J}$ are both zero so that above Maxwell's equations simplify to

$$\nabla \cdot \vec{D} = 0 \tag{2.16}$$

$$\nabla \cdot \vec{B} = 0 \tag{2.17}$$

$$\nabla \times \vec{H} = \frac{1}{c}\frac{\partial \vec{D}}{\partial t} \tag{2.18}$$

and $\vec{B} = \mu\vec{H} = \vec{H}$ since in optics the magnetic permeability $\mu = 1$. Then (2.18) reads

$$\nabla \times \vec{B} = \frac{1}{c}\frac{\partial \vec{D}}{\partial t} \tag{2.19}$$

Now apply the curl to (2.14)

$$\nabla \times (\nabla \times \vec{E}) = -\frac{1}{c}\frac{\partial (\nabla \times \vec{B})}{\partial t} \tag{2.20}$$

Using the identity, for instance

$$\nabla \times (\nabla \times \vec{E}) = \nabla(\nabla \bullet \vec{E}) - \nabla^2 \vec{E} \tag{2.21}$$

and transforming the time derivative, we have

$$\nabla(\nabla \bullet \vec{E}) - \nabla^2 \vec{E} = -\frac{1}{c}\frac{\partial (\nabla \times \vec{B})}{\partial t} \tag{2.22}$$

Substituting from (2.19) for $(\nabla \times \vec{B})$, we obtain

$$\nabla^2 \vec{E} = \frac{1}{c^2}\frac{\partial^2 \vec{D}}{\partial\, t^2} \tag{2.23}$$

By definition the dielectric function ε is

$$\vec{D} = \varepsilon\vec{E} \tag{2.24}$$

Finally, the plane wave equation is

$$\nabla^2 \vec{E} - \frac{\varepsilon}{c^2}\frac{\partial^2 \vec{E}}{\partial t^2} = 0 \tag{2.25}$$

And the solution to this wave equation has the form

$$\vec{E}(\vec{r},t) = \vec{E}_0 e^{i\vec{k}\bullet\vec{r}-i\omega t} \tag{2.26}$$

Therefore, Eq. (2.25)

$$(\nabla^2 - \frac{\varepsilon}{c^2}\frac{\partial^2}{\partial t^2})\vec{E} = 0 \tag{2.27}$$

$$\begin{aligned}\nabla^2 &= \nabla \bullet \nabla \\ &= (\frac{\partial}{\partial x}\hat{x} + \frac{\partial}{\partial y}\hat{y} + \frac{\partial}{\partial z}\hat{z}) \bullet (\frac{\partial}{\partial x}\hat{x} + \frac{\partial}{\partial y}\hat{y} + \frac{\partial}{\partial z}\hat{z}) \\ &= \frac{\partial^2}{\partial x^2} + \frac{\partial^2}{\partial y^2} + \frac{\partial^2}{\partial y^2}\end{aligned} \tag{2.28}$$

and

$$\begin{aligned}\vec{k}\bullet\vec{r} &= (k_x\hat{x} + k_y\hat{y} + k_z\hat{z}) \bullet (x\hat{x} + y\hat{y} + z\hat{z}) \\ &= k_x x + k_y y + k_z z\end{aligned} \tag{2.29}$$

Therefore

$$\begin{aligned}\nabla^2\vec{E}(\vec{r},t) &= \nabla^2\vec{E}_0 e^{i\vec{k}\bullet\vec{r}-i\omega t} \\ &= \{\frac{\partial^2}{\partial x^2}e^{i\vec{k}\bullet\vec{r}-i\omega t} + \frac{\partial^2}{\partial y^2}e^{i\vec{k}\bullet\vec{r}-i\omega t} + \frac{\partial^2}{\partial z^2}e^{i\vec{k}\bullet\vec{r}-i\omega t}\}\vec{E}_0 \\ &= \{(ik_x)^2 e^{ik_x x+ik_y y+ik_z z-i\omega t} + (ik_y)^2 e^{ik_x x+ik_y y+ik_z z-i\omega t} + (ik_z)^2 e^{ik_x x+ik_y y+ik_z z-i\omega t}\}\vec{E}_0 \\ &= -(k_x^2 + k_y^2 + k_z^2)\vec{E}_0 e^{ik_x x+ik_y y+ik_z z-i\omega t} \\ &= -k^2\vec{E}(\vec{r},t)\end{aligned} \tag{2.30}$$

and

$$\frac{\varepsilon}{c^2}\frac{\partial^2 \vec{E}}{\partial t^2} = \frac{\varepsilon}{c^2}\frac{\partial^2}{\partial t^2}\vec{E}_0 e^{i\vec{k}\bullet\vec{r}-i\omega t} = -\frac{\varepsilon\omega^2}{c^2}\vec{E}(\vec{r},t) \tag{2.31}$$

Insert (2.30) and (2.31) into (2.25)

Then,

$$(k^2 - \frac{\varepsilon\omega^2}{c^2})\vec{E}(\vec{r},t) = 0 \tag{2.32}$$

Eq. (2.32) shows that the dispersion relation that relates k to ε and n.

$$(k^2 - \frac{\varepsilon\omega^2}{c^2}) = 0 \tag{2.33}$$

$$\varepsilon = \frac{k^2c^2}{\omega^2} \tag{2.34}$$

By definition

$$N^2 = \frac{k^2c^2}{\omega^2} \tag{2.35}$$

Then

$$N^2 = \frac{k^2c^2}{\omega^2} = \varepsilon = \varepsilon_1 + i\varepsilon_2 \tag{2.36}$$

.

From Eq (2.36)

$N = N(\omega) = n_r + ik$. n_r is the ordinary index of refraction and k is the extinction coefficient. Yet from Eq. (2.36) the fundamental response of the material is ε, so we must be

prepared to work in both representations. In essence, ε describes the material properties and N optical propagation. We can also express as follow:

$$n_r = \sqrt{\frac{1}{2}\left(\sqrt{\varepsilon_1^{\,2} + \varepsilon_2^{\,2}} + \varepsilon_1\right)} \tag{2.37}$$

$$k = \sqrt{\frac{1}{2}\left(\sqrt{\varepsilon_1^{\,2} + \varepsilon_2^{\,2}} - \varepsilon_1\right)} \tag{2.38}$$

or

$$\varepsilon_1 = n_r^{\,2} - k^2 \tag{2.39}$$

$$\varepsilon_2 = 2n_r k \tag{2.40}$$

We use three different substrates in these measurements: (100)GaAs, (100)GaSb, and Ga. Fig. 2.4 shows reference pseudodielectric function data <ε> from 1.5 to 6.0 eV for these three substrates [37]. These data were obtained with the samples at room temperature. These dielectric functions show considerable structure in the form of peaks, which arise from transitions between the filled valence bands to the empty conduction bands in crystalline semiconductors at critical points in the joint density of states. The dielectric functions have the same basic features but differ in details. For example, both real and imaginary parts of the E_1 and E_2 peaks of GaSb are lower than those of GaAs. The main differences occur near the energies of the critical-point transitions that give rise to the spectral features seen in the figure.

The dielectric function data previously available for GaSb is extremely limited. In addition to that given in ref. [38], Seraphin [39] and Bennett [40] list only the reflectance data.

The real and imaginary parts of GaAs and GaSb of the dielectric function measured by ellipsometry are shown in Fig.2.4[37]. The values for refractive index n_r, extinction coefficient k, and reflectance R calculated from these data given Table 2.2 for various wavelengths.

The dielectric function of the reference material, which means the curve can be identified by the decrease in peak energies with increasing temperature.

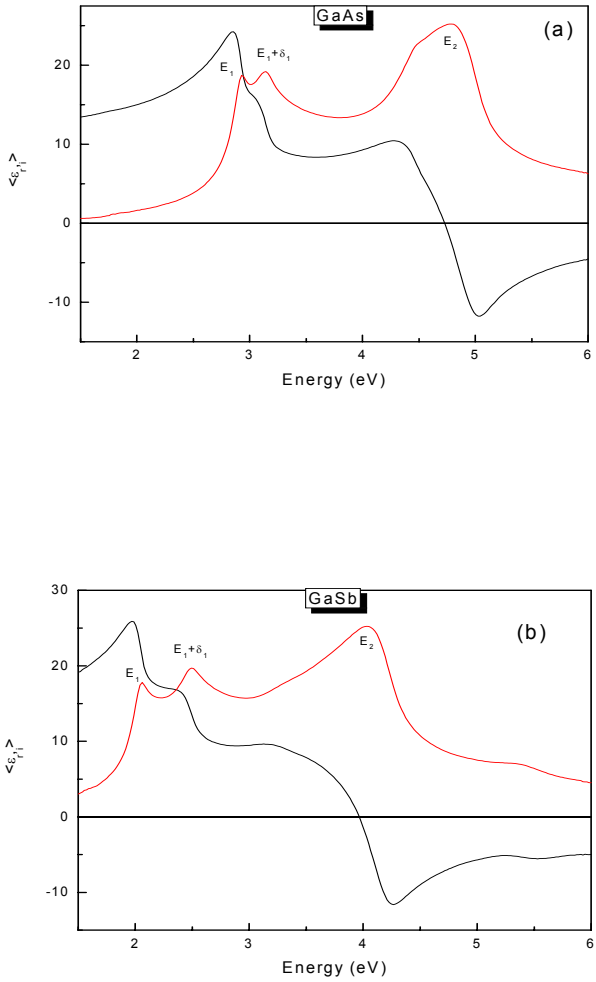

Figure 2.4. Dielectric functions of GaAs and GaSb.

Table 2.2. Optical constants of GaSb.

eV	ε_1	ε_2	n	k	R
1.5	19.135	3.023	4.388	0.344	0.398
2.5	13.367	19.705	4.312	2.285	0.484
3.5	7.852	19.267	3.785	2.545	0.485
4.5	-8.989	10.763	1.586	3.392	0.651
5.5	-5.527	6.410	1.212	2.645	0.592
6.0	-4.962	4.520	0.935	2.416	0.610

2.2.1.2 Relation to band structure

The dielectric function is closely related to energy band structure. As described in ref [36].

A typical example of a dielectric function relevant to the work done here is that of GaSb, which is shown in Fig. 2.5 [37], and its band structure Fig.2.6 [41]. The terminology used to describe the structures shown here is $E_1, E_1 + \Delta_1$, and E_2, which occur near 2.0,2.5, and 4.0 eV, respectively. This labeling convention was originally proposed by Cardona [42] according to the following:

1) E_o and $E_0 + \Delta_0$ (not shown here, but GaAs has) The '0' subscript stands for the center of the Brilliouin zone (Fig.2.8) and labels transitions along the <000> or Γ direction. For direct-gap zinc-blende semiconductors this is the energy at which ε_2 becomes appreciable. Δ_0 refers to the spin-orbit splitting at the zone center which is essential determined by the anion or Group V species.

2) E_1 and $E_1 + \Delta_1$. The '1' subscript refers to transitions occurring along the <111> or Λ direction. The spin-orbit splitting Δ_1 generally obeys the 'two-thirds rule' in that it is approximately $\frac{2}{3}\Delta_1$ in magnitude.

3) E_2. The '2' subscript refers to transitions along the X direction. However, the E_2 transition contains contributions from transitions occurring over a relatively large part of the Brillouin zone near the edges of the <100> and <110> directions. It has been shown that the height of the ε_2 peak as measured by ellipsometry is very sensitive to overlayers on the surface, e.g., oxides or roughness, and can therefore be as a measure of surface quality[43].

The directions mentioned above follows Figs. 2. 7 (a) and (b). In Fig.2.7 (a) three important direction in k-space are inserted into the first Brillion zone of the bcc lattice. They are the [100] direction from the origin, Γ, to the *H*, the [110] direction from Γ or *N*, and the [111] direction from Γ or *P*. These directions are commonly labeled by the $\Delta, \Sigma,$ and Λ, respectively.

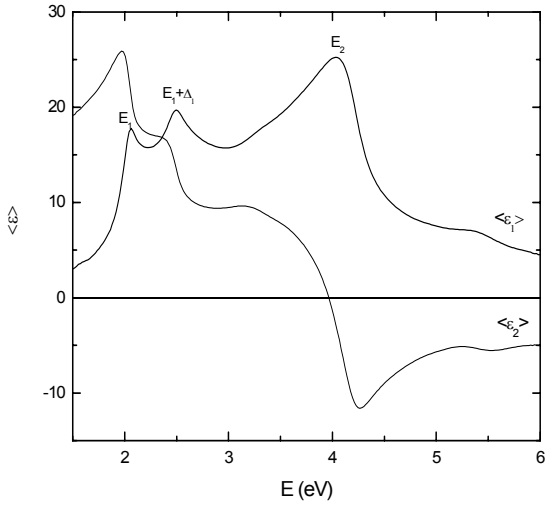

Figure 2.5. Pseudodielectric function of crystalline GaSb.

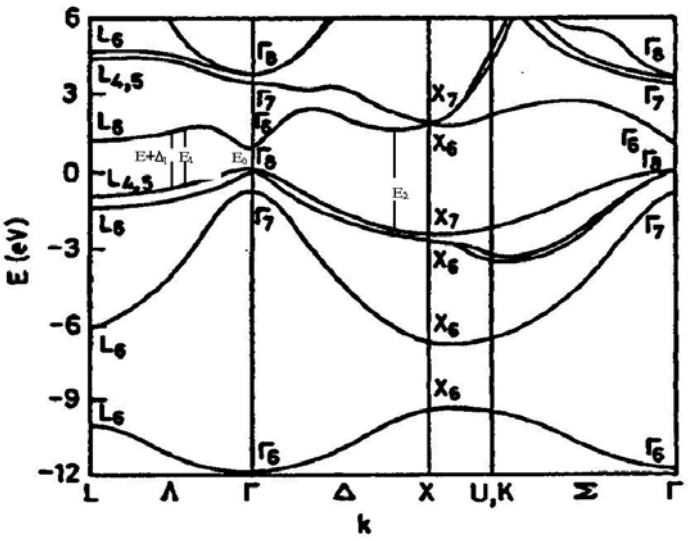

Figure 2.6. Energy band structure of GaSb.

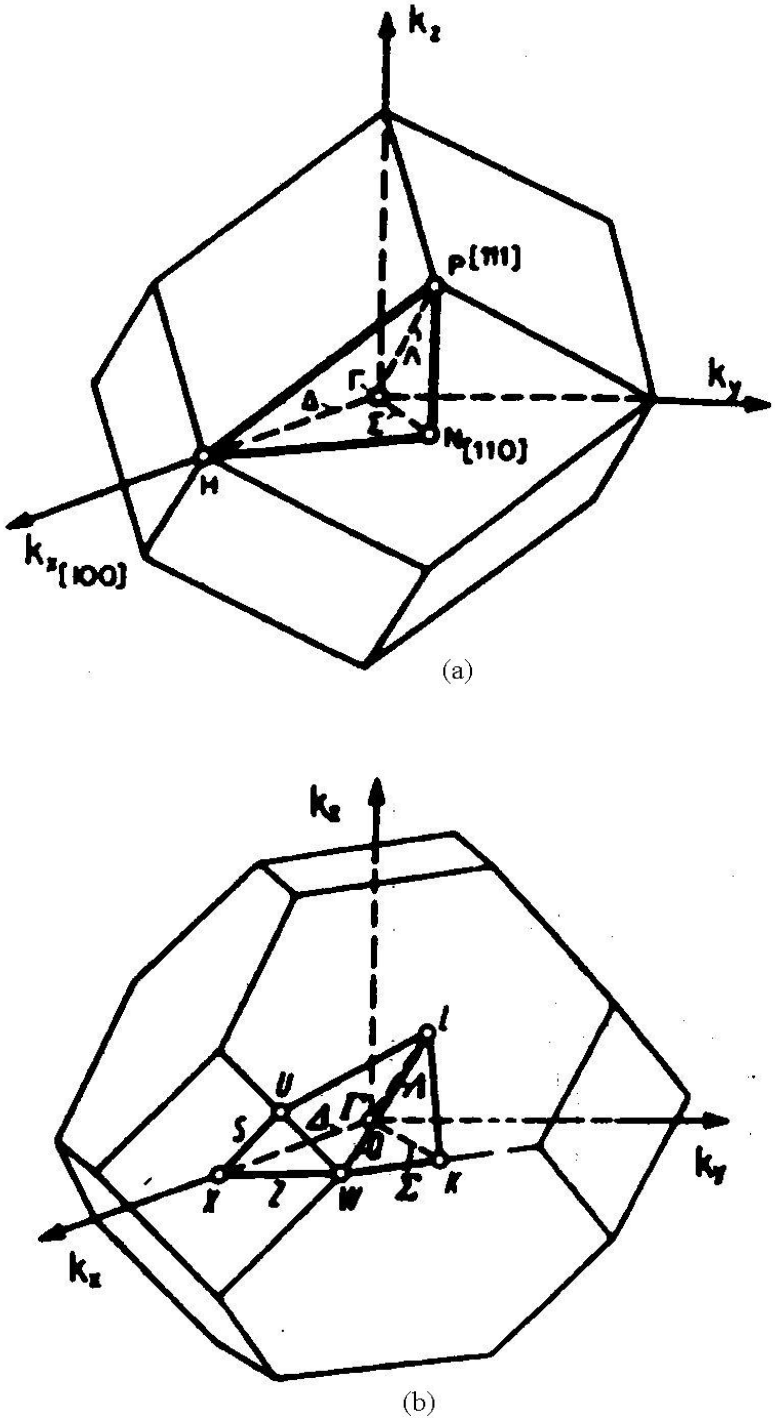

Figure 2.7. First Brillouin zone of the bcc crystal structure (a) and fcc (b).

2.3 Laminar Model

Optical modeling depends on relating measured quantities to sample properties by model calculations. Heteroepitaxial systems are by definition multilayer systems, so we consider here the description of the optical properties of two- and three-phase systems.

2.3.1 Two-phase model

We first consider the two-phase model (Fig. 2.8), which is the simplest reflecting system, consisting only of an optically thick bare substrate and transparent ambient with isotropic dielectric, respectively:

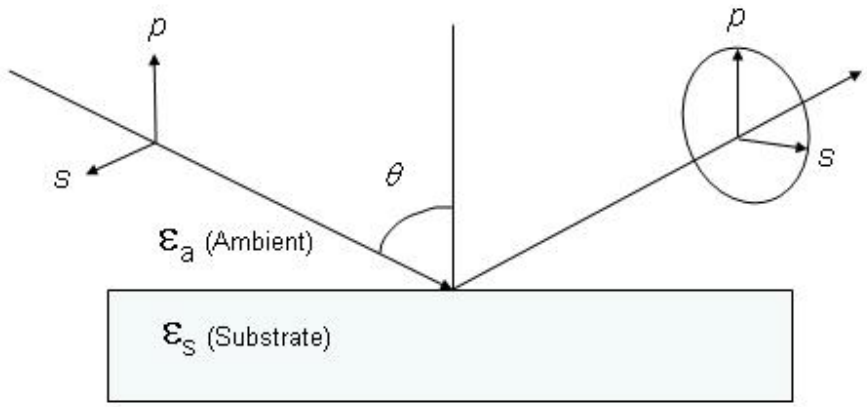

Figure 2.8. Two-phase model

Here, p and s are the directions parallel (p) and perpendicular (s) to the plane of incidence, $\varepsilon_a, \varepsilon_s$ are the dielectric functions of the ambient and substrate, respectively, and θ is the angle of incident.

The reflected field vectors, $\vec{E}_{rp}$ and $\vec{E}_{rs}$, can be described in terms of the incident field vectors via the complex Fresnel reflectance coefficients r_p and r_s as

$$\begin{pmatrix} \vec{E}_{rp} \\ \vec{E}_{rs} \end{pmatrix} = \begin{pmatrix} r_p & 0 \\ 0 & r_s \end{pmatrix} \begin{pmatrix} \vec{E}_{ip} \\ \vec{E}_{is} \end{pmatrix} \tag{2.41}$$

The Fresnel equations [44] for the complex reflectance at the ambient (a) and substrate (s) are given by

$$r^{p}{}_{sa} = \frac{\left|E_{rp}\right|}{\left|E_{ip}\right|} = \frac{\varepsilon_s n_{a\perp} - \varepsilon_a n_{s\perp}}{\varepsilon_s n_{a\perp} + \varepsilon_a n_{s\perp}} \tag{2.42}$$

and

$$r^{s}{}_{sa} = \frac{\left|E_{rs}\right|}{\left|E_{is}\right|} = \frac{n_{a\perp} - n_{s\perp}}{n_{a\perp} + n_{s\perp}} \tag{2.43}$$

where *a* corresponds to the ambient, in this case $n_a = \sqrt{\varepsilon_a} = 1$ and *s* to the substrate. The corresponding indices of refraction for non-normal incidence $n_{j\perp}$ are defined as $n_{j\perp} = \sqrt{\varepsilon_j - \varepsilon_a \sin^2\theta}$. The elliptically measured complex reflectance ratio is defined as $\rho = \frac{r_p}{r_s}$ which can be inverted to give the dielectric function of the substrate as discussed above.

$$\frac{\varepsilon_s}{\varepsilon_a} = \sin^2\theta + \sin^2\theta \tan^2\theta \left(\frac{1-\rho}{1+\rho}\right)^2 \tag{2.44}$$

This can be used for establishing a database of the bulk optical properties at growth-relevant temperatures of the most important semiconductors. It the ambient medium is vacuum or a gas, then $\varepsilon_a = 1$ and the right-hand side is the direction function of the substrate, ε_s.

2.3.2 Three-phase model, thin-film limit

We now consider the effect of an overlayer of thickness d. In this case two interfaces must be considered and the resulting expressions will contain all the parameters of the system, the dielectric functions $\varepsilon_s, \varepsilon_o$ and ε_a of the substrate, overlayer, and ambient, and the thickness of the film. For surface-physics work it is useful to consider first the situation where d/λ << 1, in which case we can do a small-term expansion and write to first order

$$< \varepsilon >= \varepsilon_s + \frac{4\pi i d}{\lambda} \frac{\varepsilon_s(\varepsilon_s - \varepsilon_o)(\varepsilon_o - \varepsilon_a)}{\varepsilon_o(\varepsilon_s - \varepsilon_a)} \sqrt{\frac{\varepsilon_s}{\varepsilon_a} - sin^2\,\theta} \qquad (2.45)$$

where <ε> is the pseudodielectric function mentioned above. If $|\varepsilon_s| >> |\varepsilon_o| >> |\varepsilon_a| = 1$ then Eq. (2.45) simplifies significantly to become

$$< \varepsilon > \cong \varepsilon_s + \frac{4\pi i d}{\lambda} \varepsilon_s^{\frac{3}{2}} \qquad (2.46)$$

which is independent of ε_o. If $\varepsilon_s = |\varepsilon_s| e^{i\phi}$, then

$$< \varepsilon > \cong |\varepsilon_s| e^{i\phi} + \frac{4\pi d}{\lambda} |\varepsilon_s| e^{i(\frac{3}{2}\phi + \frac{\pi}{2})} \qquad (2.47)$$

The expressions for larger values of d are sufficiently complicated, especially when absorbing materials are involved, that they are most easily evaluated numerically.

2.3.3 Effective medium theory

Using the definition, Eq (2.24) it follows that

$$\varepsilon = f_a \varepsilon_a + f_b \varepsilon_b \qquad (2.48)$$

$$\frac{1}{\varepsilon} = \frac{f_a}{\varepsilon_a} + \frac{f_b}{\varepsilon_b} \qquad (2.49)$$

where f_a and f_b represent the volume fractions of regions a and b, respectively. Eq (2.48) is the optical equivalent of capacitor in parallel. Eq (2.49) is the optical equivalent of capacitors in series.

The real purpose of effective medium theory is to take into account the effect of the screening charge that accumulates on boundaries between regions in a microscopically inhomogeneous medium. Since that is not practical, typical inhomogeneous systems are represented by "standard" effective medium expressions [45]. The generalized form can be written as

$$\frac{\varepsilon - \varepsilon_h}{\varepsilon + 2\varepsilon_h} = f_a \frac{\varepsilon_a - \varepsilon_h}{\varepsilon_a + 2\varepsilon_h} + f_b \frac{\varepsilon_b - \varepsilon_h}{\varepsilon_b + 2\varepsilon_h} \tag{2.50}$$

where ε_h is a "host" dielectric function, ε_a and ε_b are the dielectric functions of media "a" and "b", and f_a and f_b are the relative volume fractions of a and b in the composite such that $f_a + f_b = 1$, and the 3 in the denominator is a screening factor appropriate to spherical inclusions. The two most common effective medium theories are those by Maxwell-Garnett and Bruggeman. The Bruggeman model best describes an aggregate or random microstructure, where neither medium is the host and both are treated equally. Generally, the Bruggeman model is more generally applicable to semiconductor materials, which tend to be random in nature. One application of the Bruggeman effective theory is to describe microscopically rough material. Here, the roughness in much shorter than λ . Roughness is typically represented as a Bruggeman mixture of the material being measured and voids, where voids represent holes or defects in the crystal structure.

2.4 Real-time diagnostics in OMCVD epitaxial growth

Real-time diagnostics refers to measurements with the sample in the setting in which growth is taking place, while it is taking place. After deposition samples can be characterized by many techniques, for example photoluminescence (PL), high-resolution crystal x-ray diffraction (HXRD), Hall mobility, C-V profiling, sheet resistivity, Scanning electron microscopy (SEM), transmission electron microscopy (TEM), optical transmission and reflectance, Raman scattering, and Fourier transform infrared spectroscopy (FTIRS) and ellipsometry. However, these provide information well after growth has taken place and do not provide a means for assessing mechanisms or for correcting growth processes if errors are occurring. Techniques for studying growth while it is occurring include RHEED, reflective optical probes including SE and RDS, and x-ray scattering, but all except optical probes are restricted to high or ultrahigh vacuum. As a result optical probes are becoming more sophisticated and have reached the point where they can control growth in real time. Aspnes [46] has provided an excellent review of this topic.

The relatively high pressure environment of OMCVD eliminates the use of electron-based *in-situ* techniques except when used with the help of an OMCVD-UHP transfer system. The common probes used to assess OMCVD growth are (RDS) [46] and SE[47]. Recently, ellipsometry has been used for the compositional control of InP-containing GaInAs/AlInAs HEMT and BT structures in a multi-wafer OMCVD rotating disk reactor [48]. With the increasing industrial use of MOCVD, the desire for more control became stronger, e.g. VCSEL (vertically surface-emitting laser) growth and nanoscale growth situations concerned with interface engineering, nanostructures such as quantum dots, and thin interlayers. The difficulties with optical probes are that they need direct access to the

growth surface for both incident and reflected beams. This means optical windows or ports that do not become coated during growth, although the technology of strain-free windows to provide this access is now well developed.

2.5 Epitaxial growth techniques

The term ‘epitaxy’ has come to mean the growth of one layer in a particular crystallographic orientation to the underlying, or substrate layer. The word , epitaxy’ comes from two ancient Greek words; epi (placed upon) and taxis (ordered), referring to the ordered single-crystal film formation on top of the underlying substrate crystal substrate.

Vapor-phase epitaxial is a subject with considerable practical application, most obviously related to the production of semiconductor devices, but also to a whole range of other items. Many thin films are required to be single crystals with low defect density, and are produced via expitaxial growth processes.

There are several major techniques in epitaxial thin film growth (Table 2.3) [49]. Among these techniques, molecular beam epitaxy (MBE) and OMCVD are the principal techniques widely used today for the deposition of compound semiconductor materials. These two techniques are sometimes competitive. Both MBE and OMCVD have produced a wide range of very high-purity semiconductor materials with excellent optical and electrical properties. There has been a developing interest in narrow-bandgap Sb-containing alloys for optoelectronic applications. There are a number of hybrid techniques that combine MBE and OMCVD. These all typically utilize the ultrahigh vacuum of MBE but use materials other than the elements as sources. Most of these hybrid techniques were developed to overcome some obstacles (frequent need to break vacuum to load sources) that MBE has and generally incorporated elements of OMCVD.

Table 2.3. Overview of epitaxial techniques.

Technique	Strengths	Weaknesses
Hydride vapor-phase epitaxy	Well developed. Large scale.	No Al alloys. Sb alloys difficult. Complex process/rector. Control difficult. Hazardous precursors.
Liquid-phase epitaxy	Simple. High purity.	Scale economics. Inflexible.
Chemical-beam epitaxy	Uniform. Abrupt interfaces. Direct control of fluxes. In-situ monitoring. Selective growth.	Low throughput. No large-scale reactors. Expensive (capital). Expensive reactants. Hazardous precursors.
Molecular-beam epitaxy	Simple process. Uniform. Abrupt interfaces. In0situ monitoring.	As/P alloys difficult. Sb alloy difficult. 'Oval' defects. Low throughput. Expensive (capital)
Organometallic chemical vapor deposition	Most flexible. Abrupt interfaces. High purity. Simple reactor. Robust process. Uniform. Large scale. High growth rates. Selective growth. In-situ monitoring	Expensive reactants. Most parameter to control accurately. Hazardous precursors.

Other epitaxial techniques such as liquid phase epitaxy (LPE), magnetron sputtering have also been developed for the epitaxial growth of III-V compound semiconductors, however all have limitations that restricted their use to simpler devices.

In this section, we overview the MBE and OMCVD in a little more detail.

2.5.1 MBE

Molecular beam epitaxy was first developed by Arthur [50]and Cho [51] for the growth of III-V semiconductor epitaxial layers. In contrast with other techniques, MBE is elegantly simply in concept. In MBE, the basic elements - In, Ga, etc.- are evaporated from effusion cells as atomic or molecular beams onto a hot crystalline substrate. This necessarily occurs in UHV. The chambers are typically pumped by a combination of an ion pump, cryopump, diffusion pump, and/or turbomolecular pumps when high vapor pressures sources are being used. While MBE may be the ultimate research tool for the production of complex and varied structures, it has limitations for commercial application. Its primary advantage is the capability to access growing layers with UHV-compatible *in situ* characterization and diagnostic tools such as LEED, RHEED, and mass spectrometry to provide information on crystal perfection during growth. These diagnostic tools can be used to control the growth process to define layer thickness down to a single molecular layer (ML) and composition.

The primary disadvantages of MBE are the requirement to periodically open the chamber to add source materials to the evaporation sources, nonuniform deposition, and the difficulty of growing materials with volatile species such as P. Not surprisingly, P- based compounds such as InP have not been extensively grown by MBE [52]. However, the valued cracker sources have recently been shown to remove the practical difficulty with growing phosphides by solid- source MBE, and to allow the growth phosphorus-containing heterostructures with excellent optical properties[53]. Substrate rotation is always used to minimize lateral variations in growth rate and composition.

As an example the growth of GaAs on GaAs (001) has very widely been investigated. It can be understood in simple terms. Ga evaporates in monomer form. As evaporates as the

tertramer As_4 from elemental sources and as the dimer As_2 from cracker cells. The two react on the growth surface to form GaAs. The fact that MBE works at all is that As (and P) is highly volatile at growth temperatures and will be incorporated only if a crystallographic site is available. Thus growth always occurs with excess As (or P) being present, with stoichiometry automatically maintained and the growth rate determined by the arrival rate of the cation species to the growth surface. GaAs is unstable above a congruent evaporation temperature near 600°C.

The growth mechanisms of other compounds are similar to GaAs, with the exception of the antimonides owing to the fact that Sb is essentially nonvolatile. Consequently, the growth of antimonides by MBE is difficult, requiring constant monitoring of the arrival rates of the cationic and Sb species so that they remain in balance. This is one of the motivations for the present work.

2.5.2 OMCVD

OMCVD is also called metalorganic chemical vapor deposition (MOCVD) and metal-organic vapor phase epitaxy (MOVPE). Stringfellow [24] and Moon[28] have explained OMCVD in detail. Aardvark et al.[9] and Breiland et al. [27] also provide brief reviews of the origins of OMCVD in particular relative to compound semiconductors. In OMCVD growth occurs as a synthesis of semiconductor materials based on the reaction of special chemicals called organometallic and hydride precursors brought to the surface in the vapor phase. Even though OMCVD is highly complex, the extra dimension of chemistry makes it a flexible and powerful epitaxial materials synthesis technology for a wide range of elemental and compound semiconductors. The overall OMCVD process consists of a complex interplay between fluid mechanics, heat and mass transport, and gas-phase and

surface-chemical reactions. Understanding, modeling, and controlling this interplay in the absence of real-time information is exceedingly difficult[28], which means that despite its capabilities OMCVD is still not well understood. The flow dynamics in typical OMCVD reactors is so complex that most of our understanding comes from complex computer simulations. Simplified principle of OMCVD of GaSb growth is illustrated in Fig. 2.9 [54, 55]; the precursors are carried to the GaAs or GaSb substrate by H_2 carrier gas. After being decomposed Ga and Sb get adsorbed on the surface of the substrate where they diffuse to their incorporation sites. Finally all other organics and unreactants are carried away to scrubber.

OMCVD systems consist of a gas handling system, a reaction chamber, scrubbers to remove toxic materials, and associated safety equipment. The gas handling system controls the incoming gases and directs them to the chamber using pressure regulators, mass flow controllers, pressure controllers, and valves. A carrier gas, usually H_2 for semiconductor

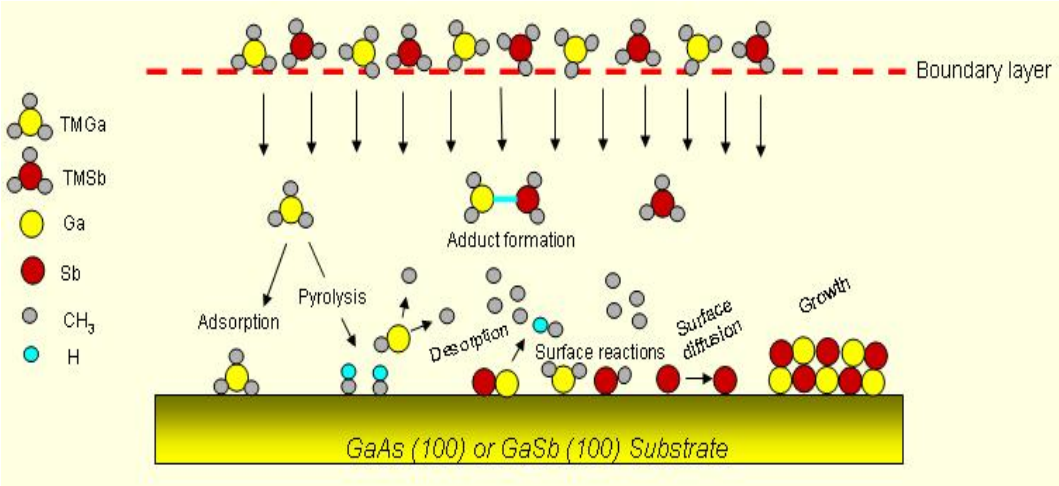

Figure 2.9. Principle of OMCVD.

materials, transports the reactants to the substrates and carries away the byproducts of the reaction.

The three primary mechanisms that govern OMVCD growth are thermodynamics, kinetics, and hydrodynamics. Since OMCVD basically an exothermic process, the maximum possible growth rate will be limited by thermodynamic forces trying to restore equilibrium, and will decrease as the temperature of the reaction site increases. If kinetics dominates the reaction rate will limit the growth rate and the growth rate will increase as the temperature increases. When the growth rate is governed by the mass transport of reactants to the substrate surface, the process is relatively temperature-independent.

There are two types of OMCVD reactors; horizontal and vertical configuration. The horizontal configuration is probably the most widely used for OMCVD growth. Drawbacks are nutrient depletion, transverse flow nonuniformity due to sidewalls, and sidewall deposits, which affect uniformity and surface quality and a have a tendency to create recirculation cells. However, most of these disadvantages have been solved by engineering or process optimization.

In a vertical reactor, modeling investigations have shown that there are three general categories regarding the boundary layer over the wafer. These are stagnation-point flow, impinging-jet flow; and rotating-disk flow. Most vertical reactors attempt to emulate the stagnation-point model. As in the horizontal configuration, to overcome recirculation flows and buoyancy effects from the highly heated susceptor, the carrier gas flow must be carefully balanced for each operating condition to achieve true stagnation-point flow. The impinging-jet condition is not used much in practice because it has a strong tendency to create recirculation cells. Rotating-disc reactors avoid many of these difficulties, because the effect

of rotation is to create a pumping action that pulls the gases down and across the substrates on the disk. Olander [29] first suggested the use of rotating disks to promote more uniform deposition in OMCVD. OMCVD preferentially operates under mass-transport-limited growth conditions, where the growth rate depends on the transport of the reactant gases to the surface and layer composition and uniformity can be controlled by the reactor geometry and flow conditions. Frolov et al [30] report in the OMCVD growth of GaAs using TMG and AsH_3 that rotation of the pedestal on which the substrate sits increases the growth rate. Since this would decrease the mass transport boundary layer thickness, this finding is also consistent with the hypothesis that the growth rate is limited by mass transport.

During OMCVD growth several types of reactions may take place. Reactions that occur entirely in the gas phase are termed homogeneous, and those that occur at a solid surface are heterogeneous. The processes in the gas phase are reasonably well understood. However, the processes on the growth surface are not. This situation is in contrast to molecular beam epitaxy (MBE), where considerable knowledge about growth processes has already been obtained. The optimum OMCVD performance depends on system elements such as the gas handling system that meters the incoming gases and directs them to the entrance of the reactor.

At the atomic level understanding OMCVD requires knowledge of chemical reactions that occur between the substrate surface and molecular precursors such as TMG and TMSb. In addition, we need to understand processes that take place on the surface, for instance diffusion, nucleation, adsorption, and desorption. Growth kinetics is largely determined by only a few categories of atomistic rate processes, which form the basis also for more complex growth situations. Unfortunately, the absence of suitable diagnostic tools has severely

impeded the development of our understanding of OMCVD relative to that of MBE in this regard.

We comment finally on safety issues. MBE is a relatively safe growth process since everything is contained within a stainless steel shell except when the chamber is opened as for example replenishing effusion cells. On the other hand, OMCVD uses precursor species such as AsH_3, which are extremely toxic and must be handled with great care. This requires OMCVD growth systems to be monitored constantly by toxic gas monitors, and personnel who work with OMCVD growth to be fully trained in the handling of toxic materials, the use of self-contained breathing apparatus (SCBA) gear, and how to respond in emergency situations. These safety procedures add considerably to the cost of OMCVD setups, but in industrial situations this added cost is usually counterbalanced by increased production rates and by avoiding the need to open up the reaction chamber on occasion to replenish the reaction species.

2.6 Crystal structure and defects

2.6.1 Crystal structure

Most III-V semiconductors crystallize into the cubic zincblende form shown in Fig. 2.10. The unit cell, the smallest division of the lattice into identical repeating

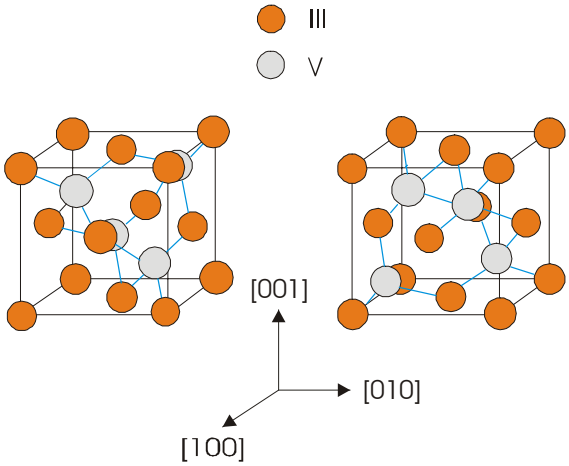

Figure 2.10. Two possible orientations of the zinc-blende crystal structure common to many of the III-V compound semiconductors such as GaAs, GaSb, and GaP.

parallelepipeds, of the cubic zincblende structure is same as that of diamond except that the two sublattices are occupied by different atoms. One lattice is composed of group III, and the other of group elements. The crystal is uniquely identified by description of the atomic arrangement within a layer and the placement of consecutive layers relative to each other.

2.6.2 General crystal defects

Single-crystal thin films are of technological importance in modern electro-optics and electronics because they are the real estate upon which everything is built. A successful thin-film technology may rapidly develop new electronic and electro-optic devices by bypassing the more expensive approach of bulk crystal development. However, to ensure that the resulting devices perform efficiently, the films must be as defect-free as possible.

Common point defects in crystals occur when an atomic site is substituted for the wrong kind of atom and vacant or interstitial sites are occupied, as shown in Fig. 2.11. Substitutional and interstitial defects can arise by introduction of an impurity to the lattice or by displacement of an atom in the parent lattice from its ideal position. For example as-

grown GaSb is generally p-type owing to the incorporation of large quantities of Ga on Sb sites, where it acts as an acceptor.

The simplest point defect is a lattice vacancy, which is a missing atom or ion in the crystal structure of an elemental crystal, also known as **s** Schottky defect. If the absence of an atom on a lattice site causes no changes in the rest of the crystal, we can apply in a simple way the principles to the case of vacancies in elemental crystals. The crystal will consist of N atoms and n vacant lattice sites (vacancies). The probability of finding an unoccupied state – assuming that the energy to create such a vacancy is given by E_v (eV) - is related to the energy required to produce the vacancy and the temperature of the crystal. This probability that a given site is vacant is proportional to the Boltzmann factor (k_B) for thermal equilibrium.

$$P_v = \frac{n}{N + n} = \frac{\exp(-E_v / k_B T)}{1 + \exp(-E_v / k_B T)} \qquad (2.47)$$

where N is the number of atoms and n is the equilibrium number of vacancies. If n << N, then

$$\frac{n}{N} = \exp(\frac{-E_v}{k_B T}) \qquad (2.48)$$

Eq. (2.48) shows that at temperatures above absolute zero, elemental crystals at equilibrium contain vacancies. The equilibrium concentration of vacancies decreases as the temperature decreases.

Actually, the absence of an atom on a lattice site changes the vibration patterns of neighboring atoms. The actual concentration of vacancies will be higher that the equilibrium value if the crystal is grown at an elevated temperature and then cooled abruptly, thereby freezing in the vacancies.

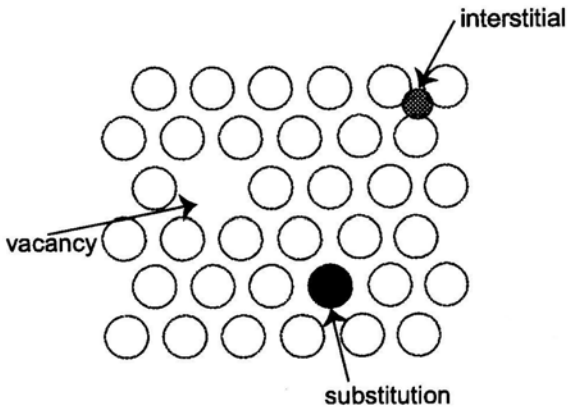

Figure 2.11. Examples of point defects.

The other major defect that occurs in epitaxially grown material is the line imperfection known as a dislocation or linear lattice defect. These are the major way by which stress caused by lattice mismatch is released. Dislocations come in several basic types. We first describe an edge dislocation.

Fig. 2.12 shows edge dislocations in a simple cubic lattice [56]. These correspond to the insertion or removal of a partial plane of dislocations from the crystal, which displaces the planes of either side. In Fig. 2.12 (b) a partial plane of dislocations has been inserted in the break formed by the plane ABCD. This is a positive edge dislocation. A negative dislocation would occur if an extra plane were inserted below ABCD.

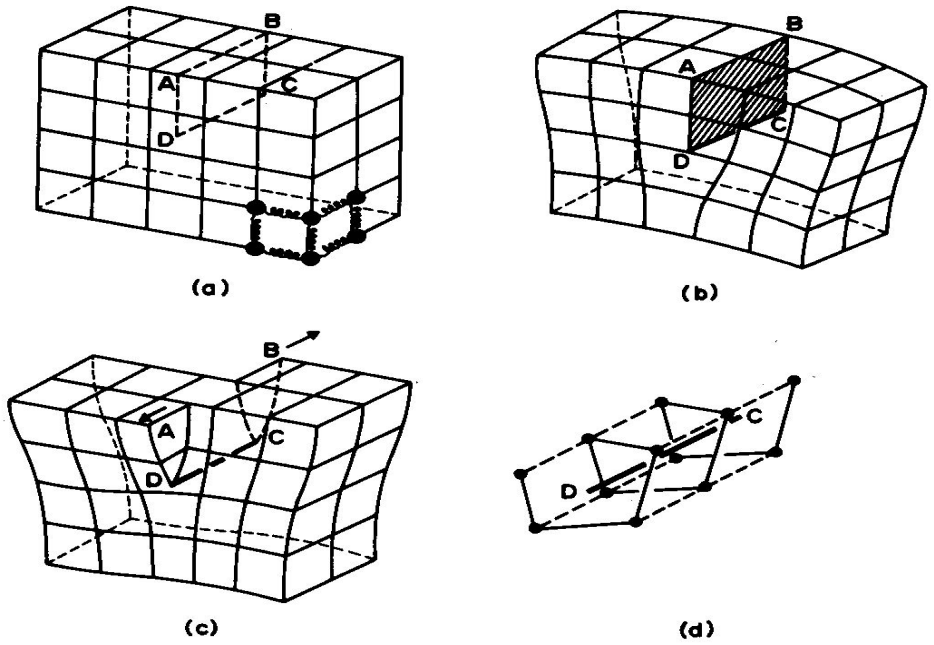

Figure 2.12. Illustration of edge and screw dislocations. (a) Model of a simple cubic lattice; the atoms are represented by filled circles, and the bonds between atoms by springs, only a few of which are shown; (b) positive edge dislocation DC formed by inserting an extra half-plane of atoms in ABCD; (c) left-handed screw dislocation DC formed by displacing the faces ABCD relative to each other in direction B; (d) spiral of atoms adjacent to the line DC in (c).

The mechanism responsible for the mobility of a dislocation is shown in Fig. 2.13 [57]. Two neighboring atoms (1 and 3) on sites adjacent across the slip plane are displaced relative to each other by the Burgers vector when the dislocation glides past. The movement of one dislocation across the slip plane to the surface of the crystal produces a surface slip step equal to the Burgers vector. If atoms on one side of the slip plane are moved with respect to those on the other side, atoms at the slip plane will experience repulsive forces from some neighbors and attractive forces from others across the slip plane.

The second simple type of dislocation is the screw dislocation. A screw dislocation marks the boundary between slipped and unslipped parts of the crystal. Screw dislocations correspond to the insertion of removal of a partial plane of dislocations from the crystal,

which displaces the planes on either side. In figure 2.12 (c) the crystal on the side of ABCD has been displaced relative to the crystal on the other side, with the displacement in the direction of the line $\overline{AB}$. Imagine taking the line $\overline{AD}$ and rotating it anticlockwise with $\overline{DC}$ as the axis of rotation. After 360^{o} rotation it has moved down one lattice position in an unbroken plane. The set of parallel planes initially perpendicular to $\overline{DC}$ have been transformed into a single surface, and the spiral nature is clearly demonstrated by the atom positions.

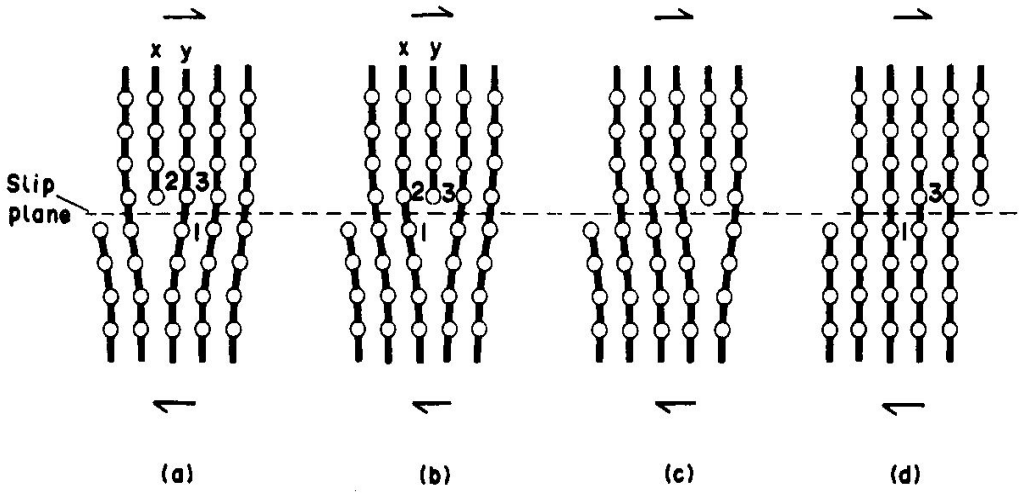

Figure 2.13. Movement of an edge dislocation: the arrows indicate the applied shear stress tending to move the upper surface of the specimen to the right.

This $\overline{DC}$ is a screw dislocation transforms successive atom planes into the surface of a helix; this accounts for the name of the dislocation. It is important to realize that in both the edge and the screw dislocations described the registry of atoms across the interface ABCD is identical to that before the bonds were broken. The presence of a screw dislocation in the crystal provides a step (or multiple step), which spirals under the flux of adatoms[58].

Ichimura et al.[59] carried out a thermodynamic calculation of native defect concentrations in $Al_xGa_{1-x}Sb$ alloys. The theoretical model they used is extended from that of Van Vechten [60]. The enthalpies of vacancy of formations used here were calculated by Van Vechten on the basis of his macroscopic cavity model. In his model, the formation enthalpy of a vacancy is mainly the surface energy of a cavity. The formation enthalpy of V_{Sb} is larger than that of V_{Ga} because the covalent radius of Sb is larger than those of Ga [59]. The results of these theoretical calculations which give the concentration of each of the native defects like V_{Ga}, V_{Sb}, Ga_{Sb} and Sb_{Ga} for crystals grown from Ga and Sb melts as a function of temperature are shown in Figs.2.14 and 2.15.

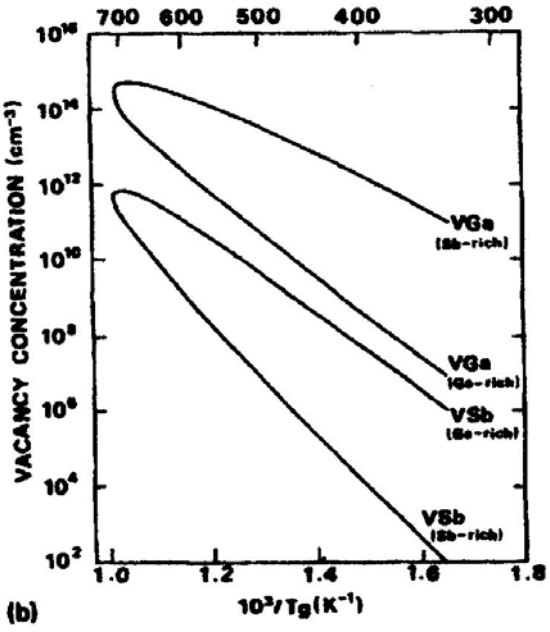

Figure 2.14. Temperature dependence of vacancy concentrations in GaSb.

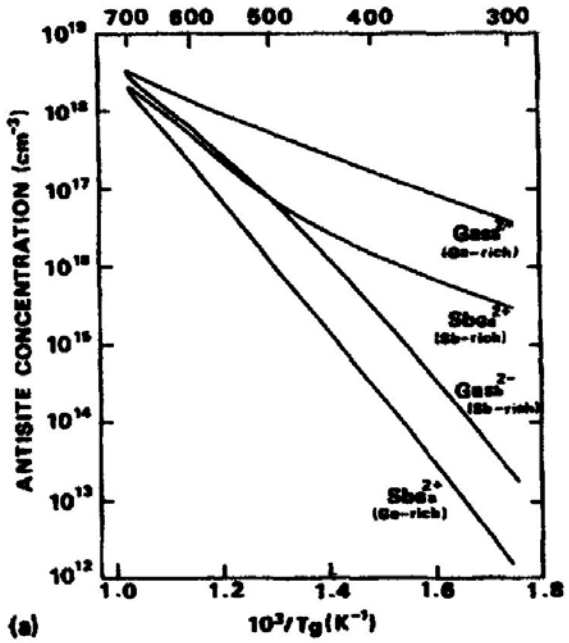

Figure 2.15. Temperature dependence of antisite concentration in GaSb.2.7 Thin Film Growth

Thin films are deposited on substrates to achieve properties obtainable or not easily obtainable in the substrates alone. Additional functionality in thin film growth can be achieved by depositing multiple layers of different materials. This section handles fundamentals for thin film growth.

2.6.3 Growth modes

The epitaxial growth of a thin on a substrate can occur in one of three main different growth modes: Frank-Van der Merwe, which is 2D layer-by-layer growth, Volmer-Webber, where the deposited atoms form islands on the surface or three-dimensional growth, and Stranski-Krastanov, where the atoms first wet the surface but again form islands. These are shown in Fig. 2.16. The particular growth mode of a given system depends on the interface energies and on the lattice mismatch. Shchukin et al.[61] discussed theoretically on the growth patterns.

Frank-Van der Merwe growth is the most desirable and is most used in device production. This is the usual growth mode for lattice-matched materials with high interfacial bond energies. It occurs when cohesive energy between the film and substrate atoms is greater than the cohesive energy of the film, but monotonically decreases as each new film layer is added. In Frank-van der Merwe growth atoms more strongly bound to substrate than to each other. As a result the atoms first aggregate to form monolayer islands which then expand and coalesce to form the first monolayer. 2D growth can be enhanced if the islands in the first incomplete layer are small because an atom on top of a smaller island will visit the island edges more frequently, thereby increasing its chance to hop down and form part of the growing crystal.

Volmer-Webber (island) growth results in the formation and growth of isolated islands. This phenomenon occurs when the cohesive energy of the film atoms is greater than the cohesive binding between the film and substrate atoms. In this mode, deposited atoms are more strongly attracted (bond) to each other than to the substrate. Thus they will first aggregate to form islands and as deposition continues theses islands will grow and finally form a continuous film. For highly mismatched combinations of semiconductor materials, the layer grown often crystallizes in the Volmer-Weber growth mode, which means that islands or clusters are formed on an unwetted substrate surface. Island diffusion can proceed by many different mechanisms, but smaller islands diffuse faster than large islands.

In Stranski-Kranstanov growth mode the atoms will first grow two-dimensionally to form either a single monolayer or a small number of monolayers thin film. However, when growth proceeds further the additional atoms of the thin film start to form three-dimensional islands on top of the thin film as in the Volmer-Weber mode. This phenomenon occurs when

the monotonic decrease in binding energy with each successive layer is energetically overridden by some factor such as strain energy due to lattice mismatch and island formation becomes more favorable. That is to say, the formation of Stranski-Krastanow islands is closely related to an epitaxial misfit and the accumulation of elastic strain energy in the epilayer. Strain relaxation occurs through the rearrangement of the deposited material when 3D islands are formed. The formation of 3D islands the strain situation completely. In this mode, the stress caused by the mismatch of the lattices of the film and the substrate produces a thermodynamic driving force that modifies structure and morphology. Deposition begins with complete wetting of the substrate. The continuous thin film is often referred to as the wetting layer. The total energy of the system decreases until the substrate is covered by one monolayer of deposit. This wetting is due to the energy contribution from the substrate/epilayer interface. The formation of islands changes the strain distribution in the wetting layer. The strain relaxation in the islands brings an energy minimum on the surface of the dot. This minimum energy is the driving force for the growth of the islands. The maximum energy around the edge of the island is due to the high compressive strain in this region. It was traditionally believed that an array of 3D islands is always unstable and that large islands will grow at the expense of evaporation or dissolving of small islands. This process is known as Ostwald ripening [62].

Semiconductors with lattice constants different from that of the substrate can be grown pseudomorphically-without dislocations at the interface- if the grown layer is thinner than a certain critical thickness. Low supersaturation, i.e. a low concentration of mobile excess material at the surface, is used to overcome any tendency to 3D growth. High surface mobility also increases the probability that the reactants reach the substrate steps and hence

also favors layer-by-layer growth. If the deposited layer is slightly mismatched to the substrate the deposited film will be strained so that its in-plane lattice constant fits the lattice constant of the substrate. Here, let us assume that the lattice mismatch between the epitaxial layer thin film and the substrate is not too large, say only around 1% of their lattice constants. To minimize this small mismatch between the two kinds of atoms, the thin film will develop a kind of lattice defect known as a dislocation (see also section 2.6.2). For example, if the lattice constant of the thin film is smaller than the substrate then the mismatch can be compensated by periodically inserting an extra plane of atoms again. This kind of dislocation is known as a misfit dislocation.

Growth may continue pseudomorphically (a pseudomorph is an altered crystal form whose outward appearance is the same of another crystal species) until the accumulated elastic strain energy is high enough to form dislocations. The thickness at which dislocations are formed is essentially determined by the extent of lattice mismatch. The trade-off is between the strain energy in the strained pseudomorphic film and the energy required to form misfit dislocations in the unstrained film. The strain energy increases with the volume of the film while the dislocation energy depends only on the area of the film. As a result pseudomorphic growth dominates when the film thickness is small. However, as the film thickness increased it will become energetically more favorable for dislocations to form.

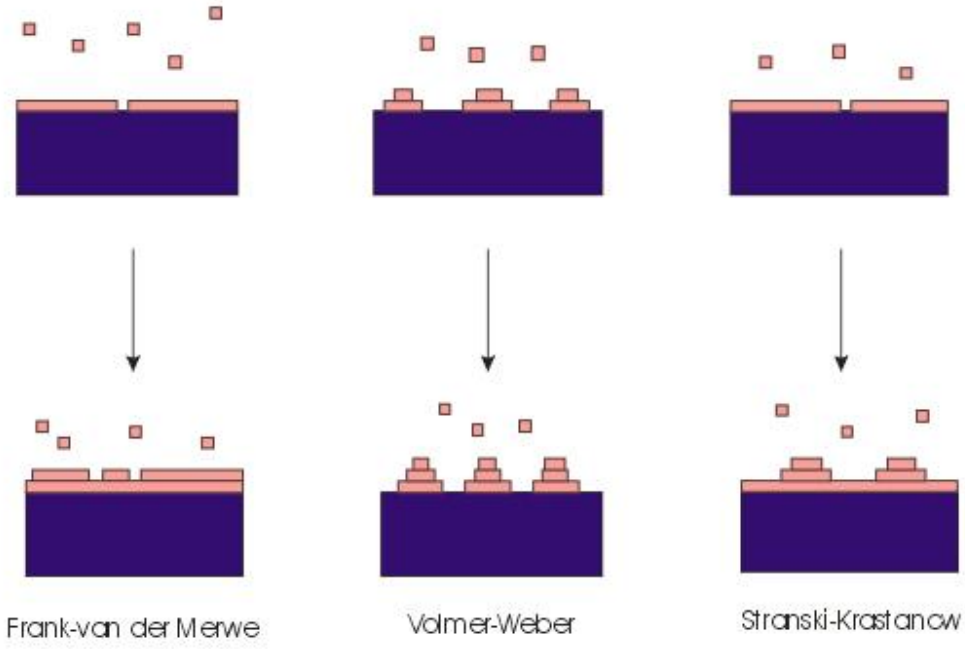

Figure 2.16. The three modes of heteroepitaxial growth.

2.6.4 Kinetics

It is well known that reactor parameter settings such as the growth pressure, bubbler pressures, growth temperature, bubbler temperatures, mass flow controller and pressure controller in the precursors and carrier gas, and so on, affect critically to the growth.

For the gas-phase epitaxy, the film growth kinetics is largely determined by a few categories of atomistic rate processes, which form the basis also for all more complex growth situations. Here, real-time diagnostics will help to analyze and understand the basic mechanism of epitaxial growth and help for technological growth control as well.

In OMCVD the rate of decomposition of precursor molecules influences the overall rate of film growth. Because the precursor decomposition rate depends strongly on the growth temperature, and the deposition rates are no longer independent, and the flux and diffusion rates cannot be independently controlled.

The concept of a boundary layer is useful in understanding the gas flow kinetics. The velocity of a fluid at the substrate or a constraining wall must be zero, while in the bulk of the fluid it is some uniform value. The region in which the velocity is changing because of the presence of the wall or the substrate is called the boundary layer. At the gas velocity increases, this layer becomes thinner. Ideally the bulk flow should be smooth or laminar, but practically, changes in the cross-sectional area, density gradients, turbulence, and temperature gradients can all cause recirculation cells to occur.

In our system we can assume that the fluid flowing into the reactor is mostly H_2 with trace quantities, for instance, $10 \mu mol / \min$, of the group III and group V precursors. The gas velocity v on the substrate surface must be low enough to let the gases have time to diffuse to the substrate surface and react there before being swept out of the reactor. However, if the

substrate is being rotated the velocity changes over the radius. The natural velocity of the substrate, which depends on the viscosity and density of carrier gas and the substrate spin rate ω, is in rad/s:

$$v = 0.8838\sqrt{(\omega m_k)} \tag{2.49}$$

where the kinematic viscosty, m_k, which is equal to $m_{k,ref}(\frac{p_{ref}}{p})(\frac{T}{T_{ref}})$, $m_{k,\text{ref}}$ is 1.09 cm^2/s. We can guess how much the total flow rate (Q: in sccm), mostly hydrogen, needs to be allowed to flow[30]. We can relate this v to the volume flow rate, Q.

$$Q = 60 \cdot v \cdot \pi \cdot r^2 (\frac{p}{760Torr})(\frac{273.15}{T}) \tag{2.50}$$

Adsorption and arrival rate of atoms at a surface(R) and boundary layer thickness:

We can assume that the growth rate is limited by the rate of arrival of film precursors to the surface .The gaseous precursors are also assumed to immediately decomposed upon contact with the hot substrate surface. This is a reasonable assumption for high temperatures and agrees well with reports.

Supposing that atoms strike a solid surface exposed to a monoatomic gas at temperature T and pressure P. It is important to determine the arrival rate of the atoms μ defined as the number of atoms striking the surface per unit per unit time. We can simply deduce μ in terms of P,T, and atomic mass, M.

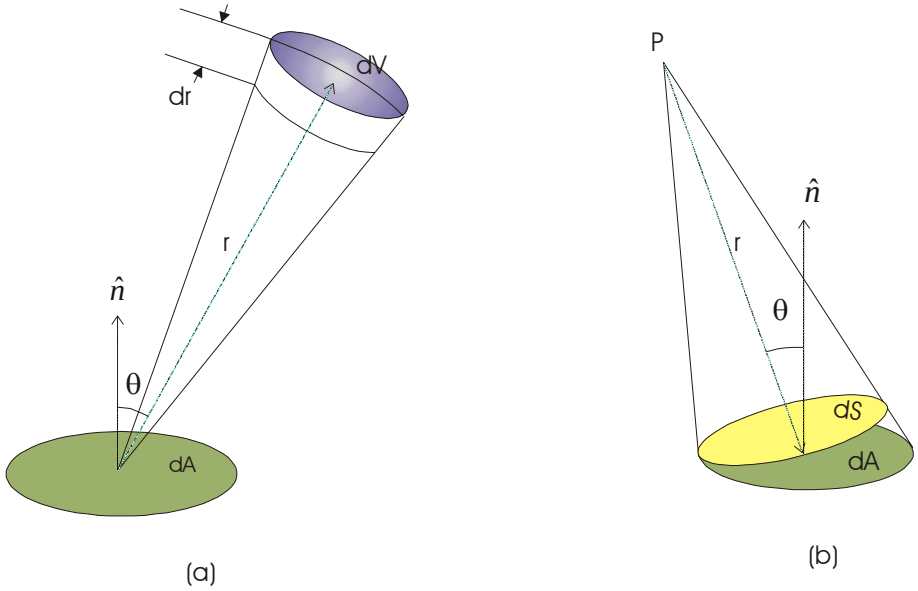

Figure 2.17. (a) An element of area on the surface, dA, and volume element in the gas, dV. (b) particles emitting from a volume element at P arrive the element of area dA on the surface

In Fig. 2.17 (a) an element of area *dV* of the surface is drawn as well as volume element *dV* in the gas distance *r*. The vector joining *dA* and *dV* makes an angle θ. The radial extent of *dV* is *dr*. The number of atoms in *dV* is *dN=ndV*, where n is the number of atoms per unit volume. Consider only the subset of atoms that directed approximately at *dA* will impinge it at a time $t = \frac{r}{v}$ later, over a duration lasting $dt = \frac{dr}{v}$. Therefore, the volume element can be expressed as $dV = r^2 d\Omega v dt$, where $d\Omega$ is the solid angle subtended by *dV* at *dA*. The fraction of atoms emitting from *dV* that strike dA is determined by the solid angle subtended by dA by a typical point in dV, P. In Fig.2.17 (b) the solid angle is $d\Omega' = \frac{dS}{r^2}$,where dS is the projection of dA onto a plane perpendicular to r, and is given

by $dS = dA\cos\theta$. The desired fraction is $df = \frac{dA\cos\theta}{4\pi r^2}$, where the solid angle has been divided by 4π steradians.

The differential rate is

$$d\mu = \frac{df}{dA}\frac{dN}{dt} = \frac{nv}{4\pi}\cos\theta d\Omega \tag{2.51}$$

By integrating $d\mu$ over hemisphere(using $d\Omega' = 2\pi\sin\theta d\theta$, where $0 \le \theta \le \frac{\pi}{2}$) the net flux is

$$\mu = \frac{n\bar{v}}{4} \tag{2.52}$$

$\bar{v}$ is an average over all speeds.

Arrival rate (R)

The arrival rate , R, of atoms on a surface in a vacuum chamber is expressed as

$$R = \frac{P}{\sqrt{2\pi M k_B T}} \tag{2.53}$$

in unit of number of atoms arriving/m^{2}s.

Monolayer arrival time(τ)

If N_o is the number of atoms in a monolayer then

$$\tau = \frac{N_o}{\mu} \tag{2.54}$$

It can be defined in terms of the substrate, the deposit or the gas molecules. The definition of the monolayer arrival time only makes sense if we have a well-defined substrate.

Diffusion

Diffusion in a solid surface is defined a motion of particles on a distinct lattice. Through the knowledge of diffusion we can understand the changes that occur in solids at high temperatures and learn more how atoms move in solids. Diffusion plays key role in many solid-state phenomena such as crystal growth, nucleation, and solid-state chemical processes like oxidation.

Fig.2.18 [63] shows the behavior of diffusion after atom arrival on the surface of the substrate. In the initial stages of heteroepitaxy in the island growth regime, newly arrived atoms have random positions on the substrate (Fig.2.18 (a)), and atoms are on the substrate. Even at room temperature, the surface mobility is enough to allow the atoms to diffuse over the surface. Therefore, horizontal jumps-movement on the terrace-are found to be much more frequent than vertical jumps-movement from terrace to lower position. Fig.2.18 (b) is more stable that Fig. 2.18 (a) since both atoms have joins a growing island, thus decreased their number of the dangling bonds. The result of this first diffusion process is a decrease of the surface roughness. If atom arrival rate increases, however, second atom may land on the island before the first one could reach (b). If the two atoms that are on the island cluster, they stabilize their presence on the island, and thus they stabilize a situation with increased surface roughness. If sufficiently high heat is applied to the system, another secondary diffusion mechanism occurs. This is demonstrated as the step from Fig.2.18 (b) to (c). Both types of secondary diffusion processes take many more steps than the primary process Fig. 2.18 (a) to (b).

When the concentrations of specific atoms vary spatially in a solid, the system may not be in thermodynamic equilibrium. The thermally activated motion of atoms and defects

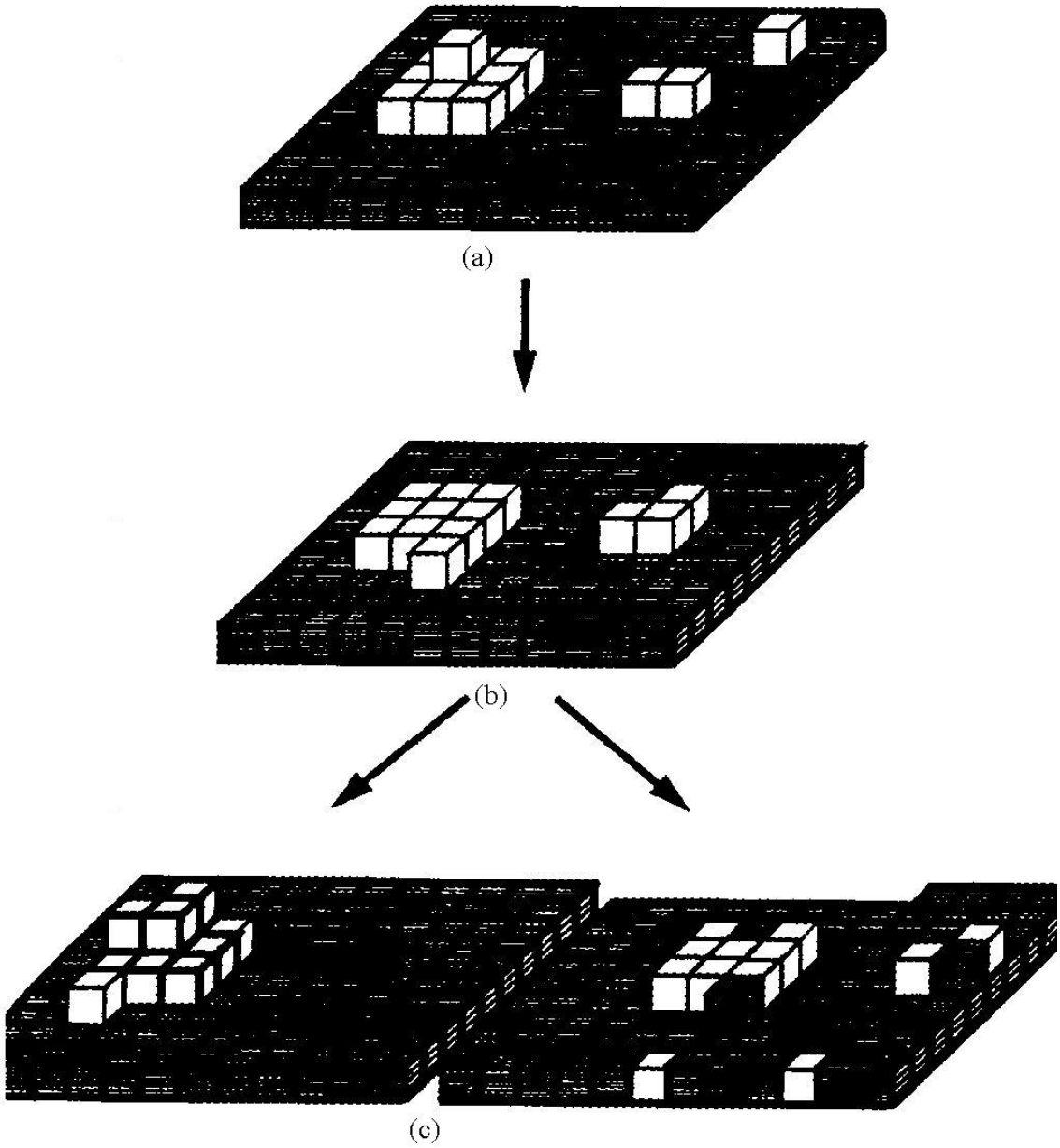

Figure 2.18. Diffusion process.

through solids often tends to eliminate concentration gradients via the mass transport processes. The thermodynamic driving force for diffusion is the increase in the configurationally or mixing entropy resulting from increased randomness when the concentration gradients are eliminated.

The transition from convection to diffusion is gradual upon approaching the surface. Viscous friction needs that the convection velocity drop to zero at the surface whatever the profile, so the final transport of reactants to the surface has to occur by diffusion through a relatively stagnant boundary layer of gas.

The diffusion constant is often found to vary with temperature as

$$D = D_o \exp(-E / k_B T) \tag{2.55}$$

where E is the activation energy for the process. To diffuse, an atom must overcome the potential energy barrier presented by its nearest neighbors. We treat the diffusion of impurity atoms between interstitial sites and vacant lattice sites as well.

If υ is a characteristic atomic vibrational frequency, the probability p that sometime during unit time the atom will have enough thermal energy to pass over the barrier is

$$p \approx \upsilon \exp(-E / k_B T) \tag{2.56}$$

It is important to define diffusion distance as a function of temperature because its value related to features such as terrace width, dictates the condensation regime. The root mean square diffusion distance , Γ , is defines as

$$\Gamma = m^{\frac{1}{2}} = \left(\frac{\upsilon_d}{\upsilon_a}\right)^{\frac{1}{2}} \exp\left(\frac{(E_a - E_d)}{2k_B T}\right) \tag{2.57}$$

where v_d and v_a are vibrational frequencies, and E_a and E_d are the activation energies for adsorption and diffusion, respectively.

2.6.5 Mismatch and linear thermal expansion coefficients

Lattice constant mismatch GaAs with GaSb is considerable, which causes many defects to be created and propagate from the interface. Strains may result from the mismatch of atomic spacing. Table 2.5 shows the lattice constant of the substrates used for the growth.

Table 2.4. Lattice constant

	GaAs	GaSb
Lattice Constant ($\overset{o}{A}$)	5.65325	6.0593

The temperature dependence of the lattice parameter of GaSb up to 680°C is given by

$$a = a_o + a_1 T + a_2 T^2 + a_3 T^3 + a_4 T^4 \qquad (2.58)$$

where T is in °C. The values of the constants a_1, a_2, a_3 and a_4 are 6.0958 $\overset{o}{A}$, $3.4963\times10^{-5}\ \overset{o}{A}/°C, 3.456\times10^{-8}\ \overset{o}{A}/°C^2, -4.6309\times10^{-11}\ \overset{o}{A}/°C^3$ and $2.6369\times10^{-14}\ \overset{o}{A}/°C^4$, respectively [19].

For films exceeding a critical thickness, most semiconductor heterostructures with small lattice mismatches, e.g., AlSb/GaSb, relax by forming misfit dislocations at the film/substrate interface [64].

While most materials expend upon heating, some semiconductors such as Si, Ge, and GaAs exhibit negative thermal expansion at low temperatures [62, 65, 66]The knowledge of

thermal expansion coefficient is very important in single growth experiment [67], in the choice of substrate for epitaxial growth [68], and in the understanding of the temperature dependence of the electronic properties [69].

Kumar *et al* [70] calculated the thermal expansion coefficient (Table 2.6) of binary semiconductors using plasmon energy data. The bond length is also important in the studies of dielectric constant, energy gaps and various structural properties of semiconductors.

The thermal expansion coefficient of the species used for OMCVD growth is listed in Table 2.5 [70].

Table 2.5. Linear thermal expansion coefficient

Materials	Si	GaP	GaAs	GaSb
Linear thermal expansion coefficient $(\times 10^{-6}/^{o}C)$	2.6	4.65	5.73	7.75

Table 2.6. Bond length and linear thermal expansion coefficient of compounds.

	Bond length (angstrom)	Temp (K)	Thermal expansion coefficient $(\times 10^{-6}/^{o}C)$	At 300 K
AlSb	2.669	1300	2.551	4.2~4.5
GaAs	2.448	1510	6.928	5.4~7.2
GaSb	2.640	980	8.866	6.1~6.5
GaP	2.360	1750	6.899	5.3~6.1

The table shows some interesting features. For example GaP will exert a compressive stress on Si during cool down, as will GaSb on GaAs. Using a novel in-situ stress monitor, Han et al [71] investigate on the grown-in tensile strain of thin film coming from a lattice mismatch. Wang et al. [72]addressed a long-standing problem involving lattice and polarity mismatch in heteroepitaxial growth of III-V alloys on silicon substrates through *Ab intio* investigations.

2.7 Growth of gallium antimonide

2.7.1 Why GaSb?

Dutta et al [19] have published a comprehensive review of the material and structural properties of GaSb. Antimony-containing III-V compounds such as gallium antimonide (GaSb) and aluminum antimonide (AlSb) have attracted much interest due to their many potential applications in novel optoelectronic devices. Antimony based III-V compounds have the smallest bandgaps, which mean applications involving the longest wavelengths of any of the III-V family of semiconductor compounds. Bandgaps range from that of gallium antimonide (1.6μm) to that of indium thallium antimonide (> 11μm). The small bandgap materials are of interest for many devices, including tandem solar cells and thermal photovoltaics. Their high electron mobilities, also a consequence of the small band gaps, makes these materials potentially useful for cryogenic ultrahigh-speed electronic devices. Thus the Sb-containing semiconductor compounds are potentially extremely useful for infrared detectors and emitters ranging from 1.3 to 1.55 μm range of interest for fiber optic systems through the 3-5 μm range of interest for chemical sensor systems, infrared countermeasures, and future extremely long distance communication systems using non-SiO_2

fibers [73], and even into the 8-12 μm regime of interest for night vision and infrared imaging application [24].

However, GaSb and related compounds remain to this day relatively unexplored in comparison with other III-V compounds [74]. Measurements on other antimony-based compounds, in particular InSb, show that stoichiometric growth does not take place with a large excess of group V flux. Excess antimony can incorporate into the InSb layer due to the relatively low Sb vapor pressure comparable to In[75].

GaSb has been grown by MBE [40, 76-80] and OMCVD[12, 81-87]. The growth of GaSb by OMCVD was first reported by Manasevit [88]. The typical precursor for Sb in OMCVD is trimethlyantimony (TMSb). TMSb is the most stable of the antimony alkyls with respect to decomposition energy. Its high vapor pressure, for example 78.6 Torr at 20 °C, makes TMSb the preferred source for near-atmospheric-pressure growth conditions. The choice of the whole precursor system must be carefully selected to correspond to the source decomposition characteristics for stoichiometry control during growth. Cooper et al. [89]used TMG and TMSb as precursors to grow GaSb. On the other hand, Menna et al. [90]used stibine (SbH_3) for an electrochemical hydride antimony source since it reduces the number of carbon-bearing molecules in the precursor species. Since the vapor pressure of liquid Sb is much lower than that of either As or P, too high a partial pressure of Sb may result in the formation of second condensed phase [24]. Chen et al [91]. use tertiarybutyldimethylantimony (TBDMSB) as an antimony source with the idea of also reducing possible C incorporation.

Our reasons for investigating the Sb systems starting with GaSb is that real-time diagnostics, in particular the capability of measuring optical anisotropy, may provide a means

of assessing the types of dimers on the growth surface and therefore the relative concentrations of Ga and Sb atoms. If this is the case, then we have a means of assessing stoichiometry during growth, and therefore possibly overcome the problems of nonstoichiometry of the grown material. In addition, the ellipsometric capability can assess growth rates and therefore determine kinetic parameters for the system. Virtually no work has been done on real-time diagnostics of the growth of Sb-containing systems, so essentially whatever we learn will be new information. Figure2.19 illustrates the phase diagram of Ga-Sb[92]. More details on the properties of gallium antimonide are given in section 4.2.

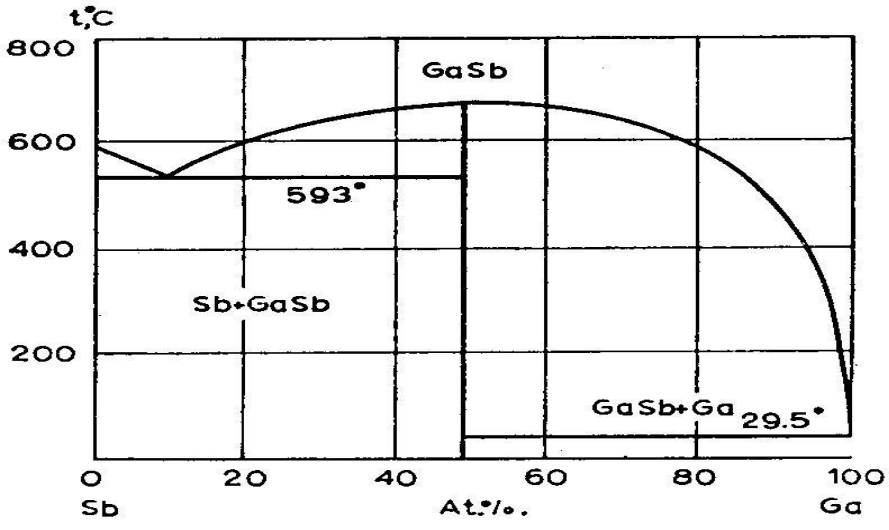

Figure 2.19. Phase diagram of the system gallium antimonide.

2.7.2 Why GaP?

Gallium Phosphide (GaP) is commercially one of the most promising III-V semiconductor compounds due to its application to opt-electronics because of wide bandgap and thermal stability. The atoms of gallium and phosphorus have 3 and 5 electrons respectively outside a core of closed shell with an s^2p^1 and s^2p^3 electronic configuration. Between them, therefore atoms have an average of four valence electrons per atom available

for bonding. These are three possible bonding in combination of gallium and phosphorus; covalent, ionic, and neutral.

For covalent bonding each phosphorus atom donates an electron to gallium atom each with four valence electrons. These combine to form sp^3 hybrid and tetrahedral bond. For pure ionic bonding we may suppose that gallium donates three electrons to phosphorus, forming Ga^{3+} and P^{3-} ions, each with spherically symmetrical closed shells configuration. These ions would be hold together in the crystal by purely electrostatic forces. The properties of a material may provide information on its ionic character. In the neutral bond gallium and phosphorus retain their electrons so that there is no charge difference between theses atoms.

It is noticed that the thermal expansion coefficients of GaP and Si are quite different and that the lattice mismatch increases with the temperature.

2.8 Surface reconstructions

The most commonly used substrate for III-V compound semiconductor growth is As-terminated (001) GaAs. In MBE growth typically occurs on the (2×4) reconstruction. This consists of a single outermost layer of As terminated with dimers that lie in the $(\bar{1}10)$ direction and occurs over a wide range of As partial pressures characteristic of MBE growth. For OMCVD the As partial pressure is typically orders of magnitude higher, so the standard reconstruction is c(4×4), which consists of 2 outermost layers of As with the As dimers oriented in the (110) direction. As might be expected, growth of well-ordered crystal of III-V compound semiconductors requires the incorporation of both constituents in the correct stoichiometric amounts.

During growth the atoms on the surface are close to the same positions that they are in the substrate, although the extra degree of freedom provided by the absence of crystal atoms on the ambient side results in rearrangements termed reconstructions, as indicated in the preceding paragraph. The driving force for reconstruction is the minimization of the surface free energy. There is a simple criterion for determining reconstructions, called the electron-counting rule, which acts surprisingly well. It is energetically favorable for dangling bonds of Group V or VI atoms to be filled and Group III or II dangling bonds to be emptied out. Thus in the case of III-V semiconductors the reconstructions that are favored are those that fill all Group-V orbitals and empty all Group-III orbitals. This describes quite naturally the absence of every fourth dimer on nearly all stable reconstructions on (001) GaAs, a result that is borne out by total energy minimization calculations.

2.9 Metallic Ga and Sb

To gain an understanding of the growth process we also need to understand the fundamental decomposition mechanisms of the precursors used in our research. The thermodynamics of gaseous $Ga(CH_3)_3$ (TMGa) have been calculated using molecular constants determined both experimentally [93] and theoretically [94, 95].

In particular, Tirtowidjojo and Pollard [96] developed a comprehensive mathematical model for the deposition of GaAs from TMGa and AsH_3 on a Ga (111) substrate using OMCVD in H_2 at atmospheric pressure. The analysis included 60 species and 232 reactions in the gas phase and 19 species and 115 reactions at the surface, reflecting very high complexity [97]. Tanaka et al. [98] also investigated this problem, using 16 elementary reactions for TMGa decomposition in H_2 carrier gas:

$$Ga(CH_3)_3 \rightarrow Ga(CH_3)_2 + \cdot CH_3 \quad (2.59)$$

$$Ga(CH_3)_2 \rightarrow GaCH_3 + \cdot CH_3 \quad (2.60)$$

$$Ga(CH_3)_3(g) \rightarrow Ga(g) + 3CH_3(g). \quad (2.61)$$

The two reactions (4.1) and (4.2) involving Ga have been investigated both experimentally and computationally [94]. At very high temperatures the decomposition process becomes kinetically controlled [96] . Trachtman et al.[95] calculated the energy required to break a Ga-C bond in TMG. They found that the values of Ga-C bonds in $Ga(CH_3)_3$ are 35.4 ~ 77.6 kcal/mol depending on how many methyl radicals are attached [95, 98, 99]. This means that a significant amount of energy is required to decompose TMG, even to eliminate the first radical.

These energy differences are reflected in the Ga-C bond length as seen from Fig. 2.20, since the bond length changes with configuration [94] as a result of the net positive charge on the Ga atom, which decreases along the series $Ga(CH_3)_3$, $Ga(CH_3)_2$, and $GaCH_3$.

In contrast to TMGa, the decomposition of TMSb has not been well studied. Winters et al.[100] investigated on the ionization and subsequent dissociation of TMSb using mass spectrometric techniques. They calculated the heat of formation of gaseous TMSb along with probable process (Table. 2.6). Bond energy of Sb-CH_3 is 47 kcal/mol.[101]. This bond energy is similar to the bond energy of Ga-C bonds, resulting in almost identical decomposition rate between TMGa and TMSb as shown in Fig. 3.6.

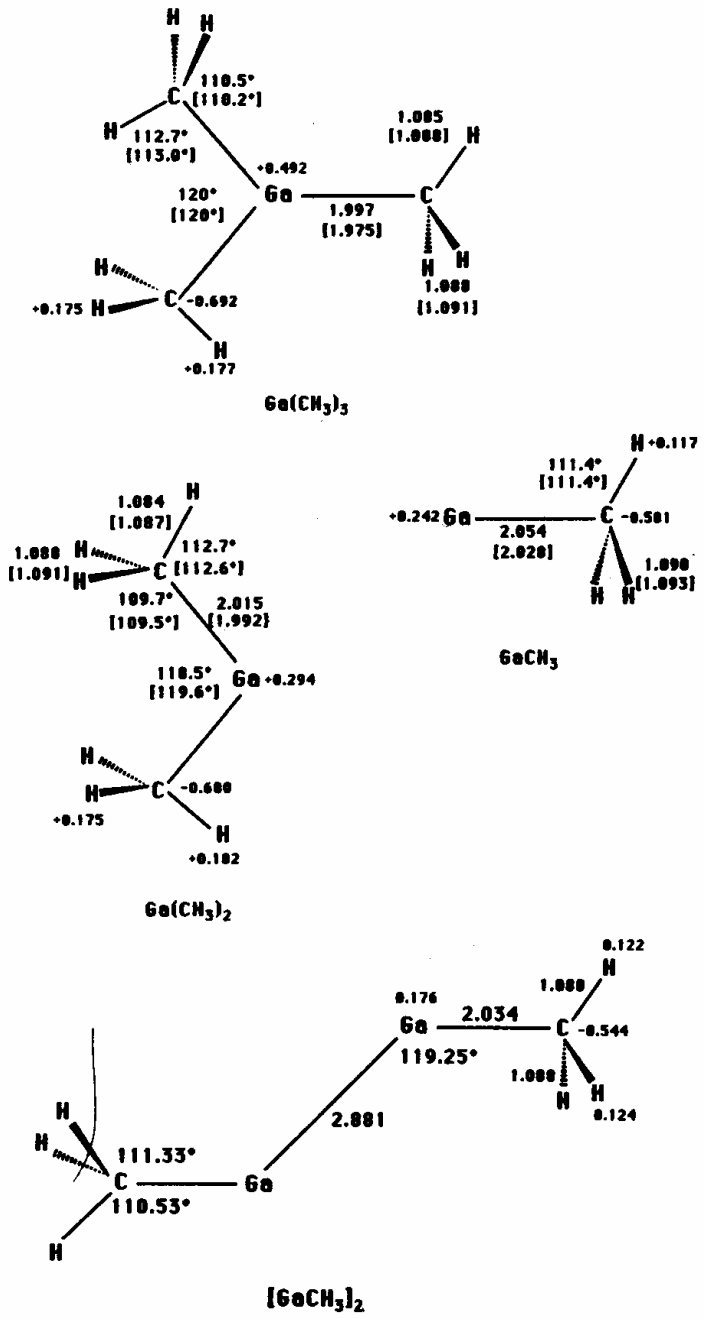

Figure 2.20. Geometries of Ga $(CH_3)_3$, $Ga(CH_3)_2$, and $GaCH_3$. Distances are in angstrom, and angles in degrees. Therefore we can summarize the above steps into one overall reaction.

Table 2.6. Heats of formation of the principal positive ions produced from TMSb.

Ion	Probable process	$\Delta H_f(ion)(kcal/mole)$
$Sb(CH_3)_3^+$	$Sb(CH_3)_3 \rightarrow Sb(CH_3)_3^+$	192
$Sb(CH_3)_2^+$	$Sb(CH_3)_3 \rightarrow Sb(CH_3)_2^+ + CH_3$	217
$Sb(CH_2)_3^+$	$Sb(CH_3)_3 \rightarrow Sb(CH_2)_2^+ + CH_3 + H_2$	265
$HSbCH_3^+$	$Sb(CH_3)_3 \rightarrow HSb(CH_3)^+ + CH_3 + CH_2$	215
$SbCH_3^+$	$Sb(CH_3)_3 \rightarrow SbCH_3^+ + 2CH_3$	272
$SbCH_2^+$	$Sb(CH_3)_3 \rightarrow SbCH_2^+ + 2CH_3 + H$	239
$SbCH^+$	$Sb(CH_3)_3 \rightarrow SbCH^+ + 2CH_3 + H_2$	258
SbH_2^+	$Sb(CH_3)_3 \rightarrow SbH_2^+ + CH_3 + 2CH_2$	154
SbH^+	$Sb(CH_3)_3 \rightarrow SbH^+ + 2CH_3 + CH_2$	209
Sb^+	$Sb(CH_3)_3 \rightarrow Sb^+ + 3CH_3$	252

Among metals Ga has one of the lowest vapor pressures (very nonvolatile) and one of the highest boiling points (~2204^{o}C). These properties make Ga very stable thermally as an element but also extremely difficult to evaporate. The temperature dependence of the vapor pressure of Ga is expressed by the equation [92].

$$\log P_{atm} = 8.540 - \frac{12000}{T} - 0.844 \log T \qquad (2.62)$$

where T is ^{0}K.

Chapter 3 Experiment

This chapter deals with the practical aspects of OMCVD growth with our present system, including procedures, settings, etc. With the integrated system OMCVD growth is a complex process requiring not only a knowledge of OMCVD technology including vacuum engineering, gas-flow dynamics, thermodynamics and kinetics of epitaxial growth, and the handling of hazardous materials, but also a knowledge of the optical equipment and how optical properties can be interpreted to determine properties of the growth surface and growing sample, and finally of the data-acquisition software and hardware including computer control of the OMCVD reactor. Unfortunately, the complexity also tends to result in a short mean-time-to-failure among the different components, so sooner or later one becomes familiar with essentially all aspects of the system.

Since the primary goal here is crystal growth, the main emphasis in this chapter is on the OMCVD part of the system. The optical calibration procedure gets less attention, since the development of the optical system and methods of alignment and calibration were the subject of a previous thesis project. Although the OMCVD part was also investigated earlier, the new aspect here is growth of GaSb, which as described in Ch. 2 has been a particular challenge owing to the low volatility of Sb.

3.1 Experimental procedure

All films were grown in our modified GS3300 reactor manufactured by Emcore. This system is a vertical rotating-sample type capable of growth on various substrates of two inches in diameter. The original 12 inch diameter chamber of the GS3300 was replaced with a 6 inch diameter chamber incorporating ports to allow optical access to the sample at about

71.5° angle of incidence. A graphite resistive heater is used underneath the susceptor, which is continuously rotating. The temperature is measured at the sample holder with a thermocouple. Our system is designed for fast gas switching with vent/run pressure balanced control of a wide variety of alkyls and hydrides. Precursor gases are mixed in a mixing block before entering the reactor. These precursors include trimethylaluminum (TMAl) and trimethylgallium (TMGa) as the group III sources, and trimethylantimony (TMSb), phosphine (PH_3), and arsine (AsH_3) as the group V precursor compounds. The vertical rotating-disk reactor utilizes a mesh screen to ensure uniform gas mixing and flow into the reactor. The Mo susceptor assembly is mounted on a magnetically coupled rotary-linear transfer Mo rod.

The carrier gas generally used is H_2, although N_2 is also a possibility. The purity of the carrier gases used in these experiments is summarized in Table 3.1 below.

Before starting growth, the growth camber was pumped by mechanical pump down to 2.7×10^{-2} Torr, then turbomolecular pump to obtain a base pressure of 1.0×10^{-6} Torr, and backed the system for the growth, and then set the growth pressure at 60 Torr.

Table 3.1. Impurity levels of various reactants.

	Impurity	Level (ppm)
H_2	O_2	1.0
	H_2O	3.0
	CO,CO_2	N/A
N_2	O_2	1.0
	H_2O	2.0
	CO,CO_2	0.5

3.1.1 Reactor considerations

Sample heating

The growth process needs high temperatures for precursor decomposition, and for removing native oxides. The deoxidation appears to be occurring from 550 to 700°C. [82, 102]. For this purpose we heated the substrates unto 700°C. The temperature distribution across the substrate must be as homogeneous as possible so the film characteristics are essentially the same over the entire area. Since the graphite heating element is itself nonuniform, this is one of the reasons why the susceptor is rotated, specifically to average the temperature. The graphite heater becomes brittle with use, so it must be handled with extreme care.

For completeness Fig. 3.1 shows the measured dependence of sample temperature on the voltage used to drive the heater.

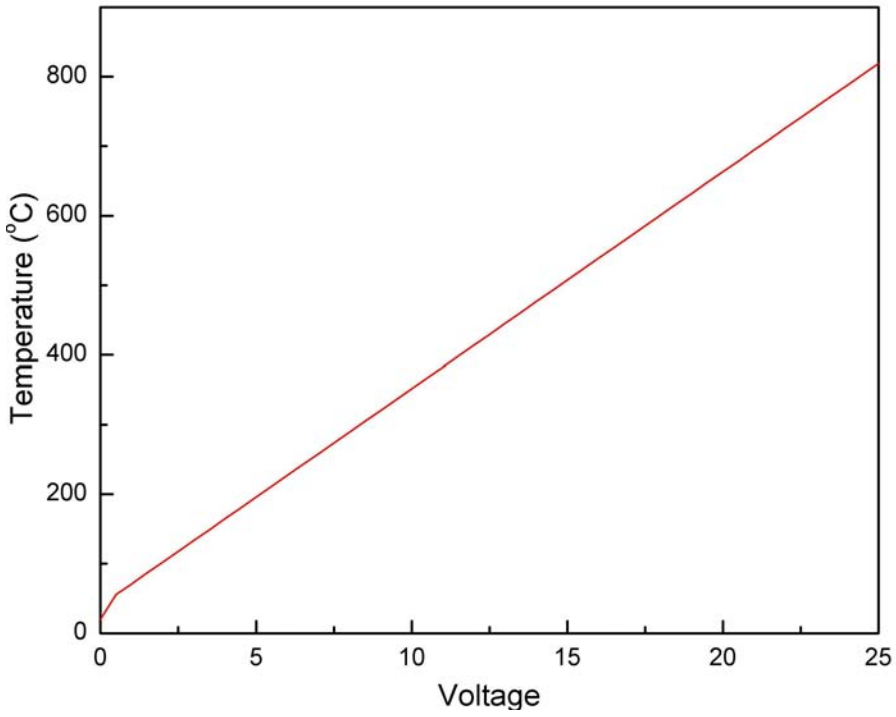

Figure 3.1. Temperature dependence of heater as a function of applied voltage.

Sample rotation

Rotating the sample is essential not only for achieving uniform heating but also uniformity and repeatability in thickness and composition of alloys in epitaxial film growth. In addition, rotation creates a pumping action to pull the incoming gas over the spinning sample. This flow also results in a reduction in the boundary layer thickness as the radius increases, thereby compensating for the loss of reactant species as the gas flows outward. The result is much more uniform growth than could otherwise be achieved, thereby avoiding one of the difficulties with horizontal-flow reactors.

The Emcore reactor is designed for the spindle to operate at approximately 1200 rpm using H_2 as the carrier gas. This number is arrived at by consideration of the flow characteristics of H_2 and its thermal conductivity and density at typical growth pressures of 60 Torr. At this rotation speed flow is essentially laminar, with no recirculation cells forming. For N_2 rotation rates must be impracticably high to achieve the same results, so for high quality growth purposes we use H_2 instead of N_2, in addition to taking advantage of the reducing properties of H_2.

Synchronization

A third reason for sample rotation is that it provides us access to surface chemistry through the optical anisotropy of the sample, which originates mainly in surface dimers. At the same time the optical anisotropy affects the ellipsometric data. If the rotation rate were essentially random, the anisotropy would cause what appeared to be noise in the ellipsometric data. In the previous rotating-polarizer configuration we avoided this by synchronizing the rotation of the polarizer and spindle at a 1:3 ratio. Since rotation by 180°

brings the system back to the same optical configuration for both polarizer and sample, in this case the ellipsometric data were obtained from analysis of the dc and 2ωt components in the transmitted intensity, and the surface anisotropy from the 6ωt component [103]. This synchronization was achieved by using the polarizer drive as the master clock, and running the spindle through a Baldor vector synchronous motor by means of pulses derived from the polarizer drive.

In the present rotating-compensator system the polarizer is fixed and the compensator is rotated. A rotating-compensator system generates ellipsometric information with the dc, 2ωt, and 4ωt components of the transmitted intensity, so to avoid crosstalk we rotate the spindle at a 5:1 ratio relative to the compensator. In this case the surface-anisotropy information is obtained from the 10ωt component of the transmitted intensity.

Prevention of sample contamination; vacuum-pump considerations

In the chemical vapor deposition process the process pump removes byproducts and unreacted precursor gases. If the quality of the grown films is unacceptable, we need to consider to what degree are contaminants responsible. While contaminants can be introduced through the source gases, during transport and deposition, and analysis [104], another source of contamination is oil backstreaming from the pump.

To understand the solutions to the oil backstreaming problem it is important to understand the types of flow found in vacuum systems. In rough vacuums above about 10^{-2} mbar (1 Pa) we find viscous flow conditions. In viscous flow the gas acts like a fluid as it moves from areas of high pressure to low pressure. Each molecule moves essentially coherently with the molecules around it. If the forward flow rate is faster than the backwards diffusion rate there can be no backstreaming in viscous flow conditions.

At high vacuums below about 10^{-5} mbar (10^{-3} Pa) we find molecular flow conditions. The mean free path between molecular collisions is now long enough so that each molecule acts independently of the movement of surrounding molecules. In this range vacuum pumps act by capturing the molecules that arrive and prevent them from returning to the vacuum chamber. To pump efficiently under molecular flow conditions wide pump openings are needed to capture the maximum number of molecules. At pressures between the pure viscous and molecular flow conditions there is a transitional flow region (Knudsen flow) where flow characteristics have the properties of both. In this region the back diffusion rates become larger and viscous flow becomes less effective at preventing backstreaming as the pressure drops.

As pressure drops, oil backstreaming (basically a molecular flow phenomenon) becomes more of a problem for pumping oils. The prevention of oil backstreaming basically becomes that of stopping the back migration of oil molecules to the sample chamber while the system is in transitional or molecular flow conditions. Surface creep of pump oil along the surfaces of the vacuum system must also be stopped. The basic ways to do this includes traps, changing types of pump oils, operational methods, or the use of dry vacuum pumps.

To avoid contamination it is important to be familiar with operational methods. In our case we deal mainly with viscous flow, except for the mass analyzer which operates in high vacuum. Since the mass analyzer was not used in these experiments, contamination from the process pump could be controlled simply by ensuring that the valve between pump and chamber was closed before the pump was turned off.

3.1.2 Calibration of the spectrometer

Before starting an experiment the optical equipment needs to be calibrated. This consists of four parts: finding the reference azimuths of the polarizer, compensator, and analyzer; calibration of the 1024 pixels of the photodiode array detector (PDA) relative to wavelength, determination of the background (scattered-light) intensity at the different pixels of the PDA, and finally the determination of the retardation angle of the compensator over wavelength range used here. These procedures have been described elsewhere [103], and for the present we have simply adopted these techniques without adding anything to them. In principle window-strain effects must also be considered, but since our measurements are typically done relative to the starting crystal surface, at the present stage of development these are small enough to be neglected.

Overall optical calibration requires both entrance and exit arms of the ellipsometer to be considered. The entrance arm contains the Xe arc lamp, focusing mirror, shutter, and analyzer prism. The only adjustment needed here is that of the focusing mirror, and that needs to be set only when the lamp is changed. In principle the same can be said of the exit arm, but since the exit arm is moved occasionally the alignment of the beam entering the rotating compensator is checked each time, along with that of the two mirrors directing the beam emerging from the polarizer into the spectrograph. The calibration of pixel number vs. wavelength depends to a certain extent on beam alignment.

Alignment of the exit arm optical components is done fairly simply by setting up the data-acquisition-and-analysis computer to display total counts as a function of pixel number, then adjusting components so that these are maximized corresponding to maximum detected intensity. Fig.3.2 shows the detected intensity as a function of pixel number. Wavelengths

[105] in Fig.3.2 in parenthesis are indicated. Once this is done, we block the beam and insert a Hg/Ar calibration lamp to generate an atomic line spectrum characteristic of Hg. By correlating the pixel numbers to the known wavelengths of the Hg calibration lamp, including second and third orders where appropriate, we obtain a calibration curve as shown in Fig.3.3.

Since we operate over a wide wavelength range, we cannot use filters to block higher orders of diffraction from the grating. Thus a final calibration must be done to assess the amount of second- and third-order diffracted light reaching the lower-numbered pixels corresponding to the long-wavelength end of the spectrum. This is done by a combination of bandpass and low-pass filters to block the long-wavelength parts first of the Hg lamp spectrum and then the Xe arc spectrum to determine how much of the short-wavelength light is scattered into second- and third-order beams. Following this step the optical system is ready to acquire data.

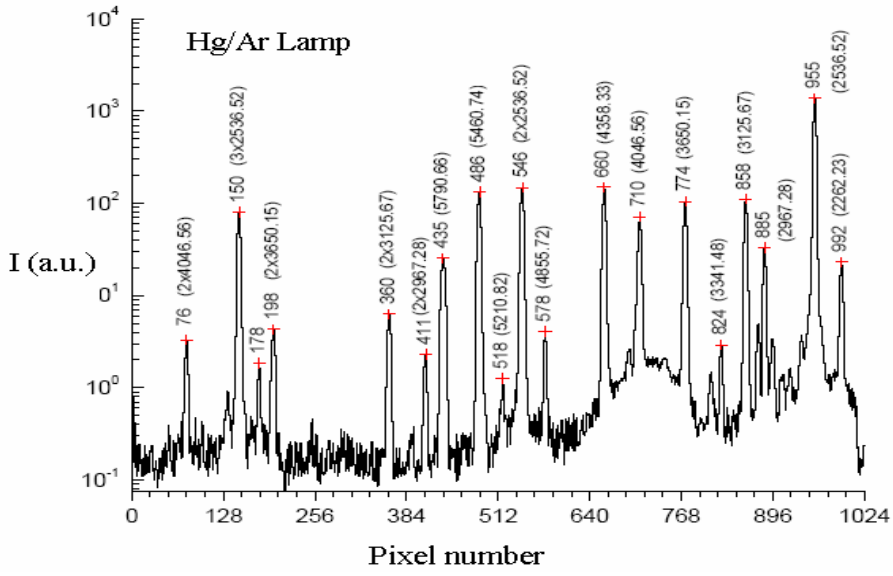

Figure 3.2. Hg calibration spectra. References are in parenthesis.

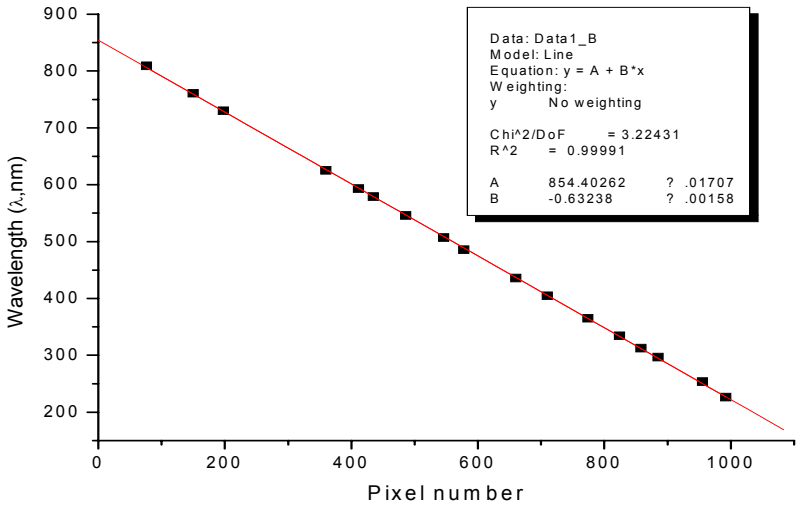

Figure 3.3. Wavelength fit vs. pixel number.

3.1.3 Gas and precursor control; Gas-handling aspects

The precursor species TMAl, TMG, TMI, and TMSb are highly flammable, and the hydride sources PH_3 and AsH_3 are highly toxic, so all must be handled in a safe manner. The hydrides are supplied as gases in high pressure containers and maintained in gas cabinets under continuous toxic-gas-monitor supervision. The organometallics are either liquids (TMAl, TMG, TMSb) or solid (TMIn) and are supplied and maintained in encapsulated bubblers of the type shown in Fig. 3.4.

Precise control over flow dynamics and growth rate requires careful control over the flow of these species. The rates of arrival of the carrier gas and precursors to the process chamber are controlled by mass flow controllers and pressure controllers.

For the metalorganics a small fraction of the carrier gas flow is routed through the organometallic liquid at a constant flow rate while the temperature of the liquid is controlled by a chiller.

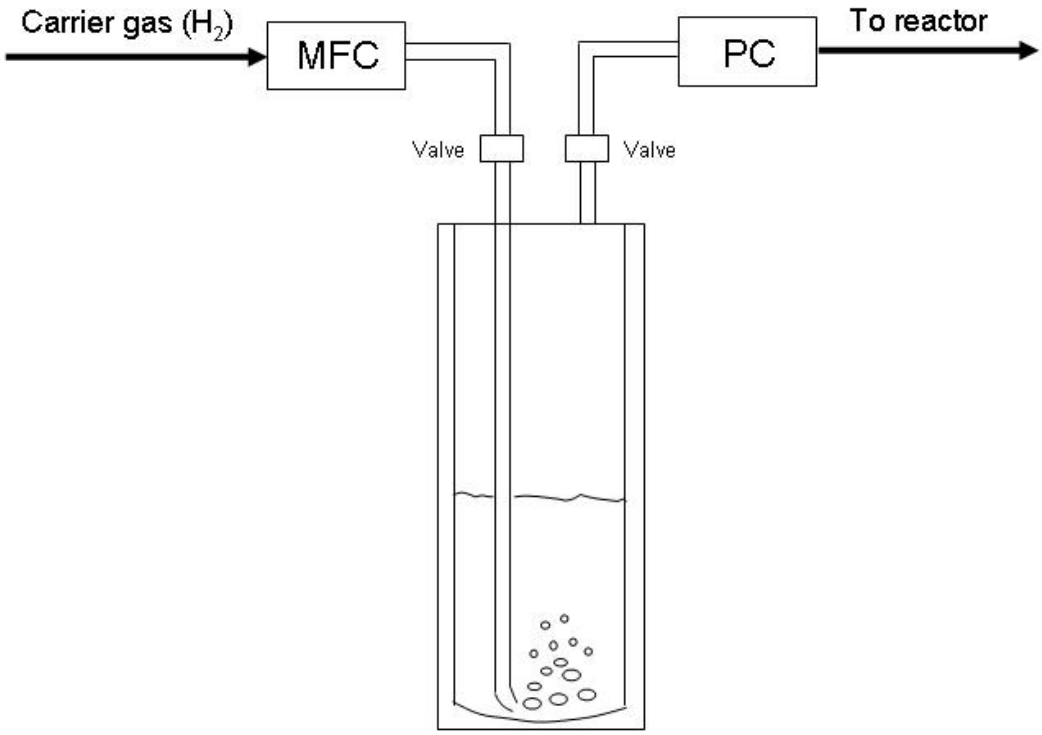

Figure 3.4. Schematic drawing of metal alkyl bubbler.

The general flow schematic for the reactants is illustrated in Fig. 3.5. The source gases (5 are shown here) go to individual valves on the mixing block and are routed either to the process chamber or to a vent line. The reason for switching gases in this way is to keep the flows through the bubblers or from the hydride sources uniform and thus avoid flow transients as the process gases are switched on and off. To accomplish this the pressure of the process and vent lines must be equal, which is accomplished through a combination of flow and pressure controllers.

Under normal operation the total pressure $P_{bubbler\ total}$ within a bubbler is approximately 800 Torr, depending on hydrogen flow rates $F_{hydrogen}$. Owing to the low vapor pressure of the chilled metal alkyls the gas is mainly carrier gas, which here we consider to be H_2. The flow rate $F_{metal\ alkyl}$ of metal alkyl out of the bubblers can be calculated using the equation [104].

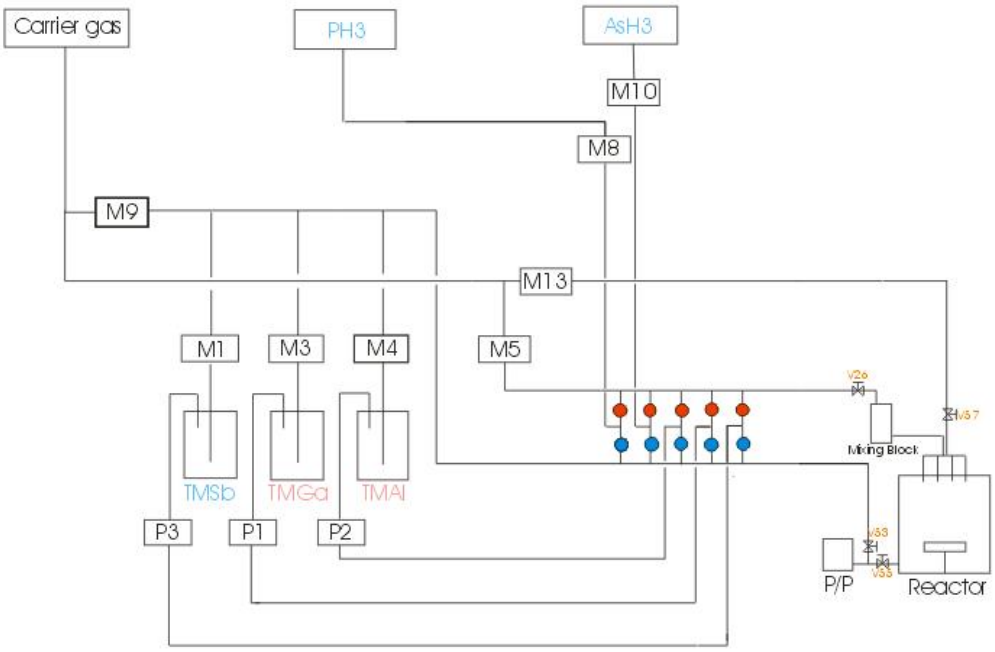

Figure 3.5. Mode: control of growth run.

$$F_{metalalkyl} = \frac{F_{hydrogen} P_{metalalkyl}}{P_{bubblertotal} - P_{metalalkyl}} \tag{3.1}$$

where $P_{metal\ alkyl}$ is the saturated pressure of the metal alkyl. The TMGa is kept at a bubbler temperature of approximately –4 °C, at which temperature its vapor pressure, calculated from [106] $\log P(mmHg) = 8.07 - \frac{1703}{T(^{\circ}K)}$, is 54.85 mmHg. TMSb is kept at a bubbler temperature of approximately –5 °C, at which temperature its vapor pressure, calculated from $\log P(mmHg) = 7.707 - \frac{1697}{T(^{\circ}K)}$, is 22.71 mmHg.

By this means we can calculate the approximate arrival rate of metal alkyl at the reactor, which in turn is proportional to the growth rate. Owing to the high volatility of As, the growth rate is determined by the arrival rate of the metal alkyls. In principle this

argument does not work for Sb, owing to its low volatility, but as we show below the decomposition of TMSb is apparently self-limiting during growth of GaSb, so even in this situation the growth rate is determined by the arrival rate of TMGa.

The arrival rate of the alkyl is only part of the procedure, since the alkyl must be decomposed by its interaction with the hot growth surface. Figure 3.6 shows the degree of alkyl pyrolysis for three common precursors [84]. The data were obtained by measuring the UV absorption at 200 nm in the exhaust line of the reactor. This data show that the decomposition temperatures of TMGa and TMSb are virtually indistinguishable. This has important implications for the growth of GaSb. It nominally means that the V/III ratio at the

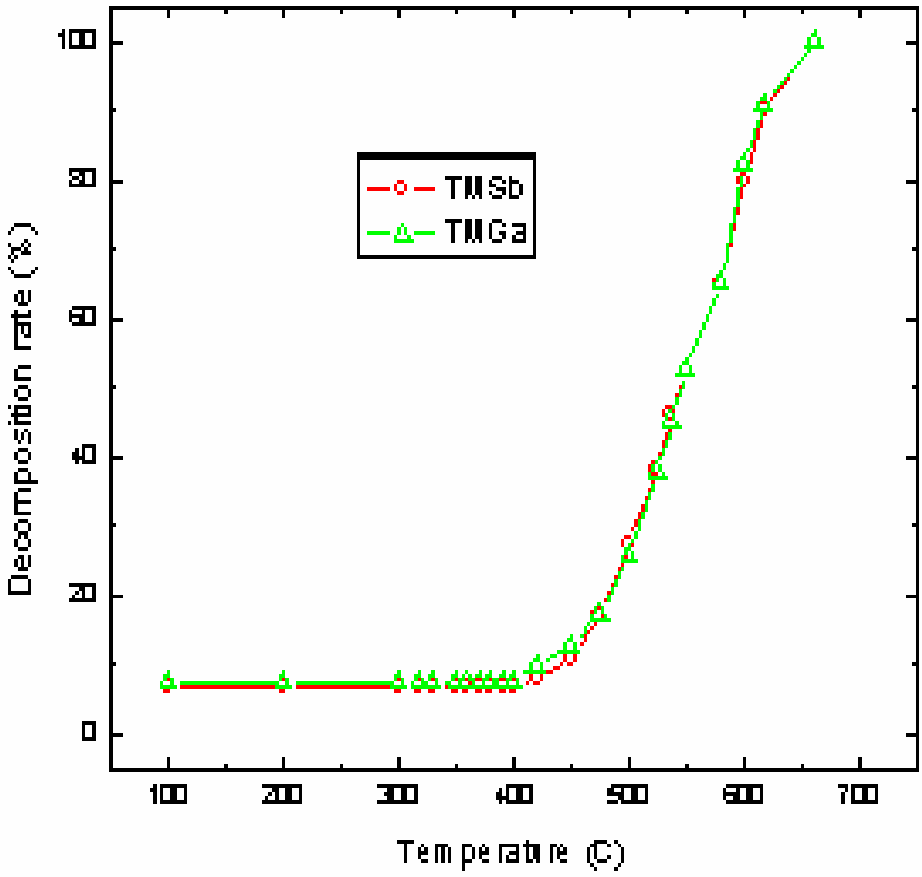

Figure 3.6. The decomposition rate of various alkyls as a function of temperature, measured by UV adsorption.

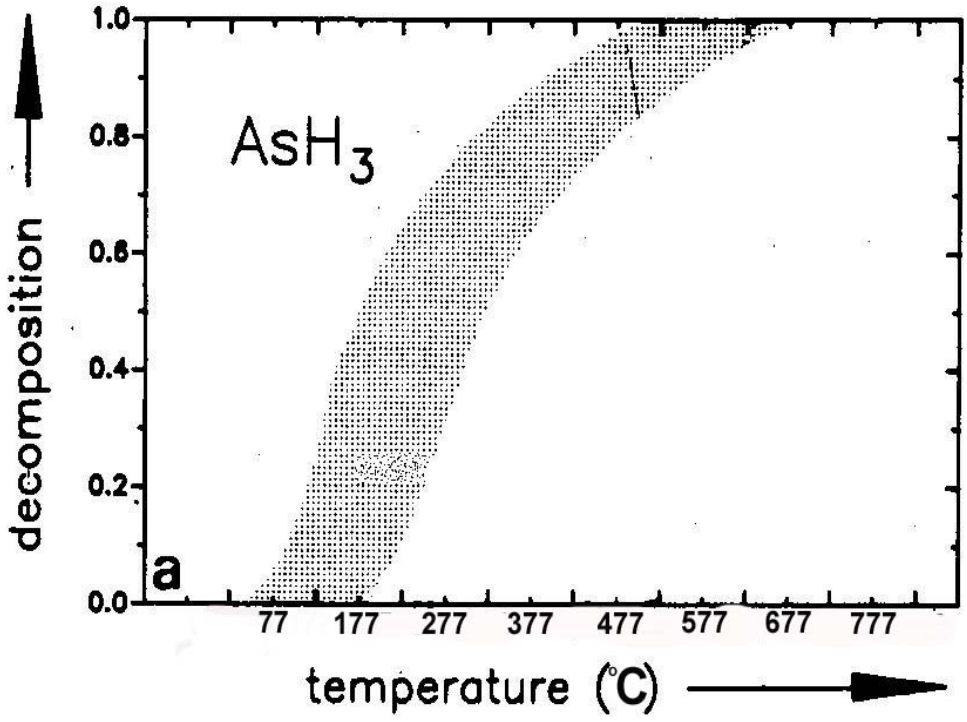

Figure 3.7. Degree of thermal decomposition of AsH_3.

the growth surface must very near unity to prevent either excess Ga or Sb from being deposited. Arsine begins to decompose at lower temperatures (Fig. 3.7) [107]. The activation energy of AsH_3 varies from approximately 12 kcal/mol at low temperatures to less than 5 kcal/mol at high temperatures.

3.2 Laser light scattering (LLS)

One of the consequences of nonstoichiometric surface concentrations of Ga or Sb is a roughening on a macroscopic scale, a difficulty that has been characteristic of previous work. Given the relative lack of sensitivity of RDS to surface species in this material system, we decided to implement laser light scattering (LLS) as a probe of macroscopic surface roughness to see whether it might provide useful information about optimum V/III flow rates.

The information provided by LLS is complementary to that provided by ellipsometry. SE can detect microscopic roughness whose characteristic dimension is much less than the wavelength of light. Microscopic roughness can be described by effective-medium theory as a dielectric layer on the substrate. On the other hand, if the roughness dimensions exceed the wavelength of light (macroscopic roughness), the light is scattered everywhere with very little getting into the SE. Consequently, SE is unable to measure macroscopic roughness, but it can be detected by scattering.

Our configuration for detecting macroscopic roughness is shown in Fig.3.8. The source is the same HeNe laser that is used to minimize runout of the spindle. The scattered light is collected by an optical fiber and routed to a Si detector after passing through a 632.8 nm interference filter. The beam is chopped at the laser at a 210 Hz rate, and detected by a lock-in amplifier to eliminate other contributions. The output of the lock-in amplifier is essentially proportional to the amount of macroscopic roughness present on the surface. Optimal growth conditions correspond to a minimum signal. Ideally this signal is zero, although this could not be achieved in practice.

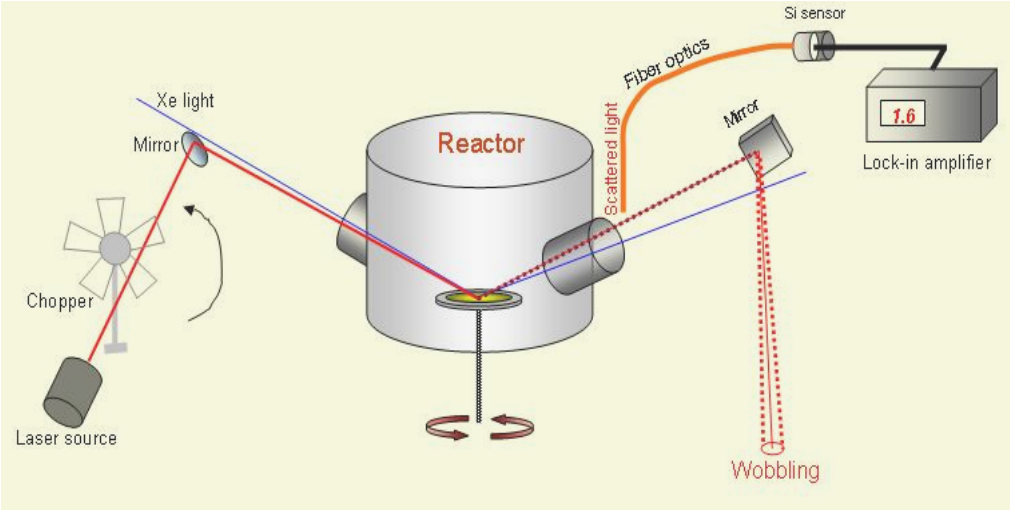

Figure 3.8. Schematic of LLS.

We found LLS be an effective way of determining the optimal V/III flow ratio as a result of the dependence of macroscopic roughness on surface stoichiometry during growth. Although LLS has long been used as a qualitative assessment of the presence or absence of roughness, we know of no prior instance where LLS has actually been used to optimize growth conditions.

3.3 Growth; a representative example

In this section we put together the above by an example, the growth of GaSb on GaAs. Here, we use a 2-in-diameter (100) GaAs substrate that is off-oriented by 2^{o} toward [011]. The substrates were manufactured by Wafer Technology LTD., England, and GaAs are p-type with a thickness of $350 \pm 25\ \mu m$. The epi-ready substrate was mounted on the Mo susceptor block and transferred into the growth chamber through the load lock. The growth pressure was 60 Torr. The total flow rate of H_2 was kept in the range of 5500 to 8000 sccm. To drive off possible contamination the sample was heated to about 400 °C for a few minutes, at which point the temperature was increased to 750 °C to drive off the native oxide.

Before starting to grow GaSb, TMGa and TMSb with different V/III ratios were fed into the reactor. Growth occurred at a sample temperature of 570 °C with TMG flow rates varied to obtain a balanced V/III ratio, which in flow-rate terms was found to be 4.12. The pseudodielectric function was recorded from the time the substrate was heated initially until it was cooled down after all exposures stopped. The results are described in detail in Sec. 4.12. Growth conditions for homoepitaxy are listed in Table 3.2, and those for heteroepitaxy in Table 3.3.

Table 3.2. Growth conditions for GaSb homoepitaxy.

		I	II	III	IV	V
TMSb (V)	F, H2 (sccm)	16	16	20	25	25
	P, out (torr)	500	500	500	500	500
	T, bub (oC)	-5	-5	-5	-5	-5
	P, TMSb.vp	23.71	23.71	23.71	23.71	23.17
	F, TMSb (sccm)	0.50	0.75	1.00	1.24	1.24
	n, TMSb, AsH3	3.56×10^{-5}	3.56×10^{-5}	4.44×10^{-5}	5.56×10^{-5}	5.56×10^{-5}
TMGa (III)	F,H2 (sccm)	7.5	5	5	3	2
	P, out (torr)	600	600	600	600	600
	T, bub (oC)	-4	-4	-4	-4	-4
	P, TMGa. vp	54.85	54.85	54.85	54.85	54.85
	F, TMGa (sccm)	0.75	0.50	0.50	0.30	0.20
	n, TMGa	1.35×10^{-5}	1.35×10^{-5}	1.35×10^{-5}	1.35×10^{-5}	8.96×10^{-6}
V/III	n, TMSb/NTMGa	1.06	1.58	1.98	4.12	6.18

Table 3.3. Growth conditions for GaSb heteroepitaxy on GaAs

		I	II	III	IV	V
TMSb (V) AsH3 (V)	F, H2 (sccm)	10	15	20	25	25
	P, out (torr)	500	500	500	500	500
	T, bub (oC)	-5	-5	-5	-5	-5
	P, TMSb.vp	23.71	23.71	23.71	23.71	23.17
	F, TMSb (sccm)	0.50	0.75	1.00	1.24	1.24
	n, TMSb, AsH3 (mol/min)	2.22×10^{-5}, 1.35×10^{-5}	3.33×10^{-5}, 1.35×10^{-5}	4.44×10^{-5}, 1.35×10^{-5}	5.56×10^{-5}, 1.35×10^{-5}	5.56×10^{-5}, 0
TMGa (III)	F,H2 (sccm)	3	3	3	3	3
	P, out (torr)	600	600	600	600	600
	T, bub (oC)	-4	-4	-4	-4	-4
	P, TMGa. vp	54.85	54.85	54.85	54.85	54.85
	F, TMGa (sccm)	0.30	0.30	0.30	0.30	0.30
	n, TMGa	1.35×10^{-5}	1.35×10^{-5}	1.35×10^{-5}	1.35×10^{-5}	1.35×10^{-5}
V/III	n, TMSb/NTMGa	1.65	2.47	3.30	4.12	4.12

Chapter 4 Results and Discussion

This chapter describes our real-time optical characterization results. In addition we list all other characterization results, which basically support the optical data. Since no prior real-time SE measurements were made for GaSb growth, this work extends our knowledge of GaSb growth by OMCVD, and demonstrates that optical characterization even in very simple light-scattering form provides enough information to significantly improve the grown material.

4.1 Preliminaries

4.1.1 Substrate preparation

The first step is to desorb adsorbed contaminants and then the oxide overlayers by heating the substrate in the OMCVD reactor. Campos et al. [108] investigated the morphologies of GaAs and GaSb surfaces annealed in this way. Voids appear in GaAs and GaSb substrates but these were found to disappear at 700 and 450^{o}C, respectively. The analysis of the ratio between the Raman intensity of TO to LO phonons suggested, according to the Raman selection rules, that the GaAs recrystallization had occurred. They also reported the presence of excess Sb in the superficial regions of the annealed samples [108] . This may also be due to binding energy differences in between Sb and Ga; the binding energy of Sb is higher than that of Ga [109].

4.1.2 Temperature calibration

The growth temperature is perhaps the most important parameter and needs to be determined accurately. The optical data were calibrated against the standard thermocouple of the OMCVD reactor. These data show the usual shifts of the energies of the different

features of the dielectric functions from higher to lower values, the usual increase in broadening, and the usual decrease in overall amplitude of the dielectric response with increasing temperature. All can be used as measures of temperature, although the shift of the energy features is the most reliable (and most common). A typical example of the behavior of the dielectric function of a GaAs substrate is shown in Fig. 4.1. The temperature here ranges from 100 to 600 °C.

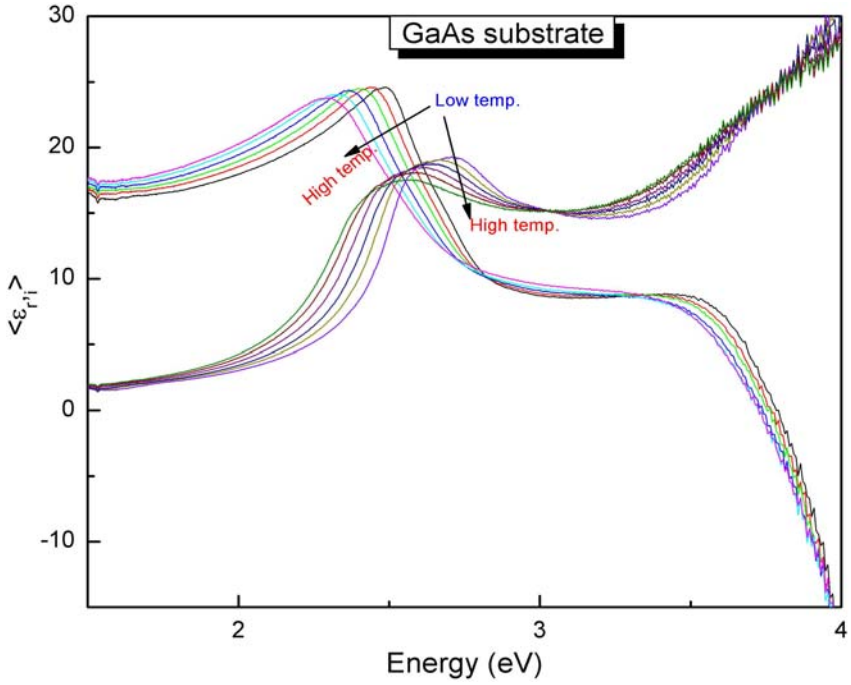

Figure 4.1. Dielectric function of a GaAs substrate at various temperatures from 100 to 600 ^{o}C.

4.1.3 GaSb

The surface instability mechanism of GaSb has been investigated by Schirm et al. [110] Low temperature processes can produce a nonequilibrium Ga_2O_3-Sb_2O_3 surface oxide according to

$$2GaSb + 3O_2 \rightarrow Ga_2O_3 + Sb_2O_3 \qquad (4.1)$$

The only stable phases that can exist in thermodynamic equilibrium with GaSb are Ga_2O_3 and elemental Sb. Any Sb_2O_3 should react with GaSb to yield Ga_2O_3 and free Sb as

$$2GaSb + Sb_2O_3 \rightarrow Ga_2O_3 + 4Sb \qquad (4.2)$$

This reaction takes place spontaneously ($\Delta G = -12 kCal/mol$) even at room temperature. Thus a GaSb surface exposed to air will form a native oxide layer consisting of Ga_2O_3, Sb_2O_3 and a fraction of a monolayer of free Sb. The binding energy of Sb (31.94 eV) is higher that of Ga (19.00 eV) [83].

The melting point of GaSb is 702-703 [92] or 712 °C [111]. The enthalpy of formation at 0^oC is $\Delta H = -4.97 \pm 0.4 kcal/mole$. The lattice parameter is $6.1347 \overset{0}{A}$, and the distance between adjacent atoms is $2.65 \overset{0}{A}$ [92].

4.1.4 Precursor decomposition

Ga droplets are known to deposit on GaSb surfaces when the V/III decomposition ratio is less than one, and Sb islands form for V/III decomposition ratios higher than certain values [25]. Not surprisingly, the surface morphology of GaSb thin films has also been reported to be highly sensitive to this ratio [12]. Finally, the stoichiometry affects the concentrations of native defects (particularly antisite defects) and dopant and impurity incorporation as well [24, 112]. Because of these difficulties the arrival rate of Ga and Sb must be controlled accurately [12, 113].

The origin of this problem is the low vapor pressure of Sb, as indicated in Table 4.1. This table provides vapor pressures of the metallic forms of the cation Ga and the anions P, As, and Sb. Although P, As, and Sb adsorption at a solid/vapor interface is reversible [54], the difficulty here is that in contrast to the situation for P and As, the vapor pressure of Sb is

not significantly different from that of Ga and hence cannot be easily reevaporated. The net result is that both Ga and Sb can accumulate on the growth surface depending on which is being deposited at the fastest rate. The decomposition parameters for TMG and TMSb, as discussed earlier, do not provide much encouragement either because both decompose at nearly identical temperatures (see Fig. 3.6). These data provide a strong argument for some type of real-time monitoring to determine the stoichiometry of the growth surface.

Table 4.1. Vapor pressure of III-V element.

Temp(^{o}C)	Ga (III)	As (V)	P (V)	Sb (V)
500	10^{-17}	$5x10^{-5}$	$6x10^{-5}$	$\sim10^{-14}$
570	10^{-15}	10^{-3}	10^{-1}	10^{-11}
600	10^{-14}	$2x10^{-2}$	2	$2.5x10^{-7}$
700	10^{-11}	2	$2x10^{1}$	10^{-4}

A simple confirmation of the temperature that corresponds to the threshold for decomposition is given in Fig. 4.2, where we investigate TMG and TMSb decomposition by

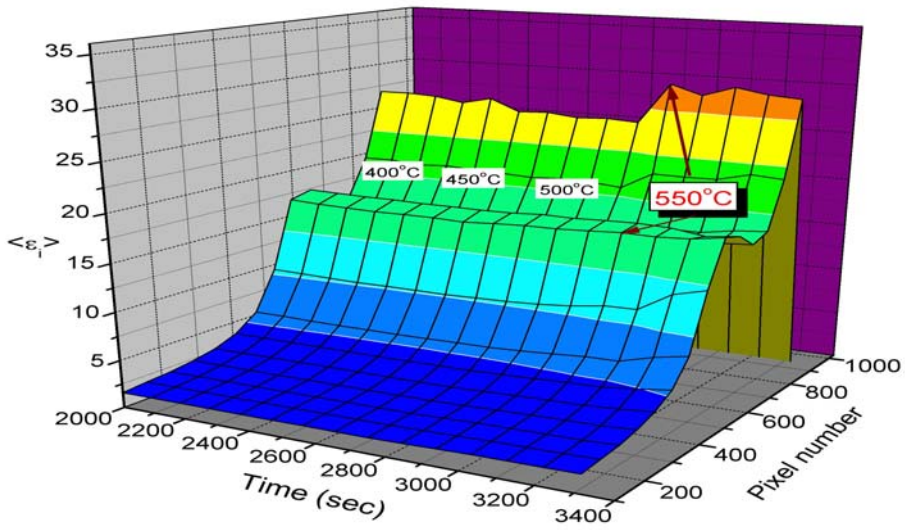

Figure 4.2. Reaction verification of TMGa and TMSb.

measuring the pseudodielectric function while dosing a temperature-cleaned GaSb sample with TMGa. Samples treated this way exhibit some microscopic roughness, but can be

recovered by growing a buffer layer. Except for the temperature dependence of the dielectric function, we see almost no change as the substrate temperature is increased from 400 to 500 ^{o}C. Clearly, the precursor molecules are passing directly though the reactor with very little chemical reaction on the surface. However, as the temperature is increased beyond 500 ^{o}C $\langle\varepsilon\rangle$ begins to change, reaching a peak value at about 550 °C. Taking this into account our growth experiments were performed at temperatures at or above 570 °C.

4.2 Homoepitaxy; initial run and discussion

Our initial homoepitaxy work was done on a GaSb substrate that had been inserted in the OMCVD reactor, cleaned, and then let sit in the reactor for a day to repair an unexpected failure of a mass flow controller. In the meantime the sample oxidized rather badly, but owing to its cost we decided to try to grow on it to see whether we could learn anything about the process. We were surprised to find through real-time optical monitoring that homoepitaxy was able to recover this microscopically degraded substrate, and performed further experiments on the recovered surface to determine the effects of individual and combined TMG and TMSb exposures. Our results on this sample hence have considerable value and are discussed here.

4.2.1 Surface recovery

Figure 4.3 shows $\langle\varepsilon_2\rangle$ data obtained at 3.56 eV on this (001) GaSb substrate as a function of time. This energy was chosen as it provides a good measure of the changes that occur as ambient conditions are changed. Here, flow rates were set to give a deposition rate of about 0.5 nm/s. The starting value of about 10 is relatively low compared to the final value of about 20. According to three-phase model predictions, this is what one would

expect if the surface were covered with an overlayer with a dielectric function value midway between that of the substrate and ambient. The overlayer here is microscopic roughness. The first exposures were to TMG, which resulted in even lower values of $<\varepsilon_i>$. Thus we can conclude that exposure of the surface to TMG alone in the absence of TMSb causes the surface to become further degraded. The detailed mechanism is not yet clear at this stage, but is presumably due either to the Ga attacking the surface or metallic Ga forming a large number of small islands.

At approximately 850 s into the run we turned on both TMG and TMSb, initiating homoepitaxial growth. The trend of the data to higher values data show that growth begins to improve the surface morphology immediately, a process that saturates at about 1150 s. About 30 s later we turned off both TMG and TMSb, noting that the surface remained stable under these conditions even though Sb was not present in the environment. We then reconfirmed the previous sensitivity of the surface to TMG exposure, and found that, as previously, this causes the surface to degrade. The combination of coverages near 1465 s will be used below to obtain an estimate of the scale of the observable anisotropy.

At about 1450 s we turned on the TMSb, finding that the surface nearly recovered and then remained essentially stationary until the next brief growth cycle at about 1525 s. The stationary nature of the trace was quite surprising, since it indicated that the (001)GaSb surface is actually stable in TMSb under our growth conditions. This observation is of significant importance, since it is generally accepted that excess TMSb causes Sb accumulation, just as excess TMG causes Ga accumulation.

This result together with the MBE observations suggests that the stability arises from the inability of the TMSb precursor to decompose completely under these conditions. It is

known for example that TMG decomposes rather readily to monomethyl gallium (MMG), and but that the removal of the last methyl radical requires substantially more energy. We speculate that a similar process occurs for TMSb, and that the removal of the final methyl radical, necessary for the accumulation of metallic Sb on the surface, requires a weakening of this bond through the attachment of the Sb to an available Ga and not an available Sb. Thus to a first approximation we can conclude that OMCVD growth here is self-regulating, in contrast to the situation for MBE, and apparently in contrast to the general perception in the literature [102]. However, our roughness measurements reported later in Ch. 4 show that macroscopic roughness does show some dependence on the V/III flow-rate ratio, so self-regulation is not 100% as is the case for growth of phosphides and arsenides. Given the nonvolatility of Sb this should not be considered surprising.

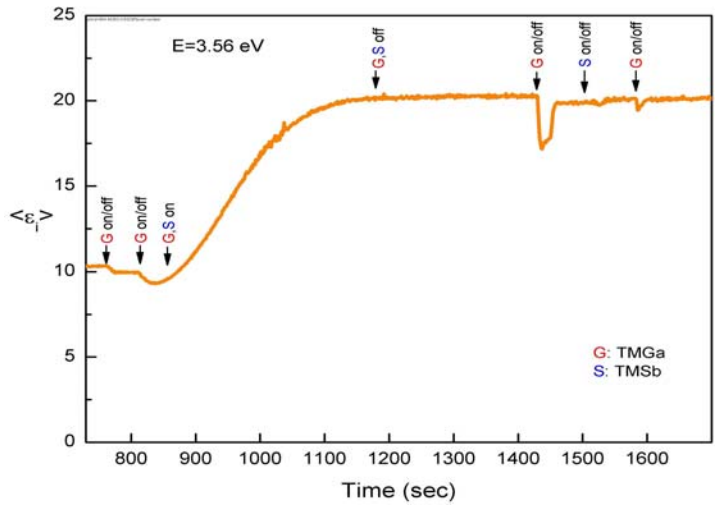

Figure 4.3. Evolution of the imaginary part of the pseudodielectric function for GaSb homoepitaxy on an initially degraded substrate under various combinations of precursor exposures.

The appearance of excess Ga and lack of appearance of Sb upon exposures of (001)GaSb to TMG and TMSb, respectively, is consistent with the relative binding energies

of the methyl groups in the two precursors. A second conclusion to be drawn from this is that excess TMG flow will certainly lead to the accumulation of excess Ga on the surface, whereas excess TMSb flow may not. Excess Ga should be readily detected after growth in that Ga tends to form antisite defects, leading to highly p-type material. The absence of heavy p-type doping can therefore be taken as evidence of the lack of excess Ga on the surface.

4.2.2 Surface reconstructions and surface optical anisotropy

In principle the α_{10} coefficient should provide information about surface termination. We investigate this by comparing the α_{10} spectra obtained for the pre-TMG-dosed, TMG-dosed, and TMSb-dosed regions of Fig. 4.4 near 1465 s. The spectra themselves showed considerable distortion, presumably as a result of residual roughness, so we present the data as differences between the pre-dosed coefficients and the TMG-dosed and TMSb-dosed coefficient in Fig. 4.4. The differences are of the order of 0.0003 for the pre- vs. TMSb-dosed coefficients and 0.001 for the pre- vs. TMG-dosed differences. These differences are small on the scale of (001) GaAs (see a later figure), but show that the termination, and therefore the chemistry of the TMG-dosed surface is different from that of the surface with Sb dosing.

A difference is clearly necessary to explain the fact that TMSb reacts to form GaSb if TMG is also present, but does not react to deposit excess Sb if only TMSb is present. However, the results also indicate that the difference in surface anisotropy is too small with the present stage of instrument sensitivity to be useful for monitoring surface homogeneity. This is one of the motivations for implementing the LSS capability, as described below.

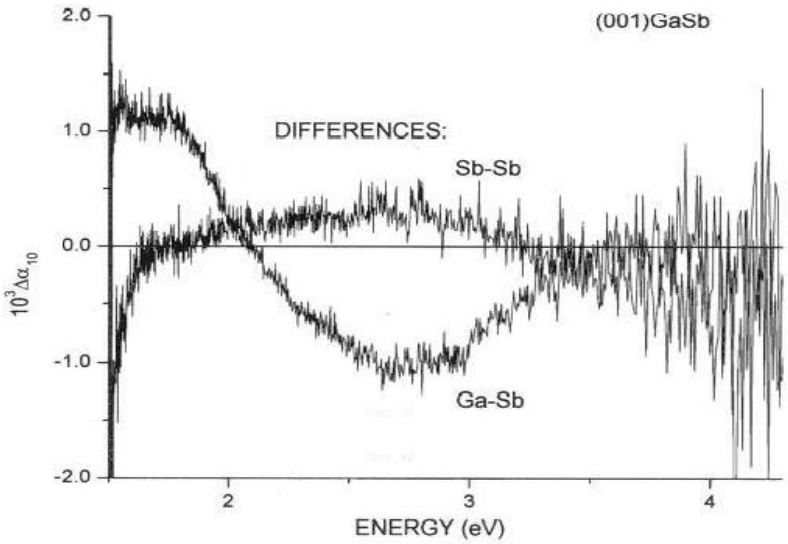

Figure 4.4. Differences in 10 coefficient spectra with TMSb and TMG exposures: Sb-Sb for before TMG exposure and after recovery; Ga-Sb for the TMG-exposed surface and its condition before TMG exposure.

In Fig. 4.5 (a) and (b), we can see that Ga dosing reduces the dielectric function of Sb-stabilized material whereas Sb dosing does not change anything. Fig. 4.6 shows time traces of recovery (2) after Ga dosing (1).

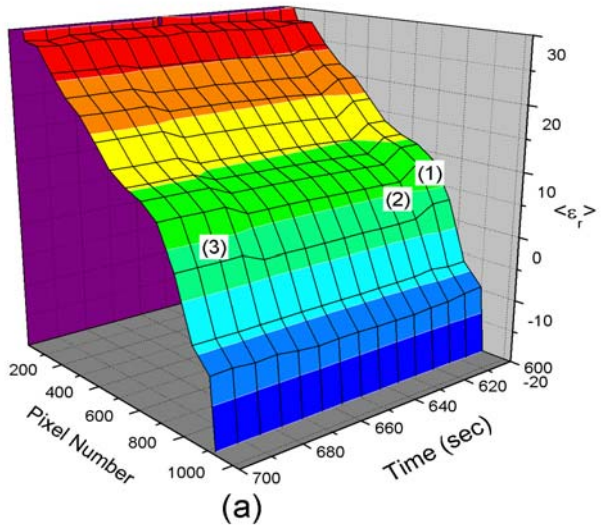

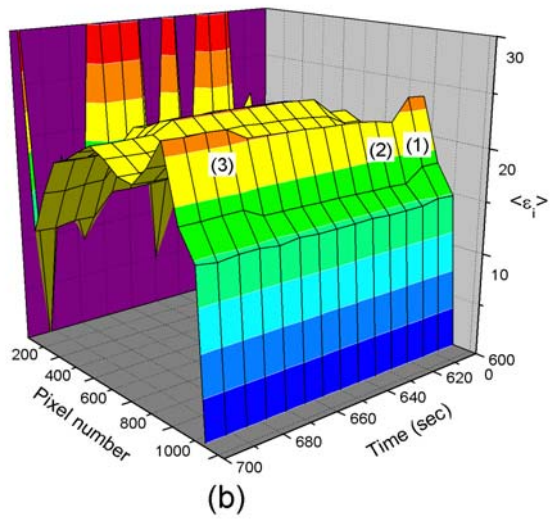

Figure 4.5. Dielectric function trend on GaSb substrate.

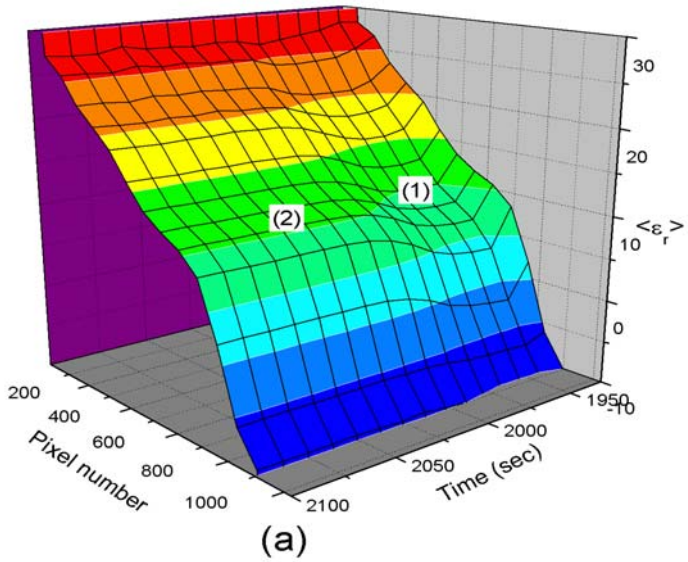

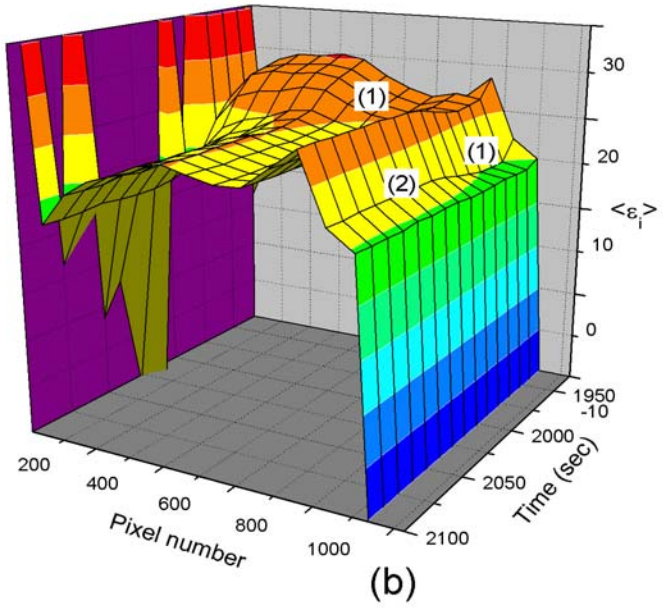

Figure 4.6. Spectral dependence of the recovery of a TMG-dosed (001) GaSb surface. TMG flow was initiated at 1930 s, and recovery started at 2000 s. Higher photon energies correspond to higher pixel numbers. Top: < r>. Bottom: < i>.

4.2.3 Post-growth characterization

As a final estimate of the nature of the growth run described above, we obtained SEM and AFM micrographs of the surface region at the location of the optical beam. These results are shown in Figs. 4.7 and 4.8, respectively. Both probes yield consistent results, revealing a large number of islands present on the surface with a characteristic height of the order of a few tens of nm and a characteristic spacing of 100 to 200 nm.

These islands are near the microscopic-macroscopic boundary for scattering. They are small enough so that they can be described approximately by the Bruggeman effective-medium theory for SE but large enough so that they will cause some light scattering. The height:width aspect ratio of about 1:4 is small enough so that the SE influence will actually be minor. On the other hand, the AFM results clearly show that these islands are elongated,

indicating a preferred growth direction. This provides an explanation of the relatively large background seen in the α_{10} data, which necessitates taking differences in order to obtain information about surface reconstructions.

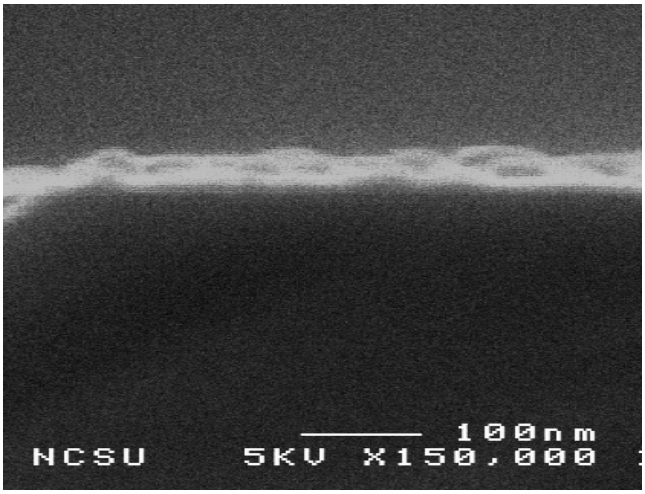

Figure 4.7. SEM image of the initial homoepitaxy sample.

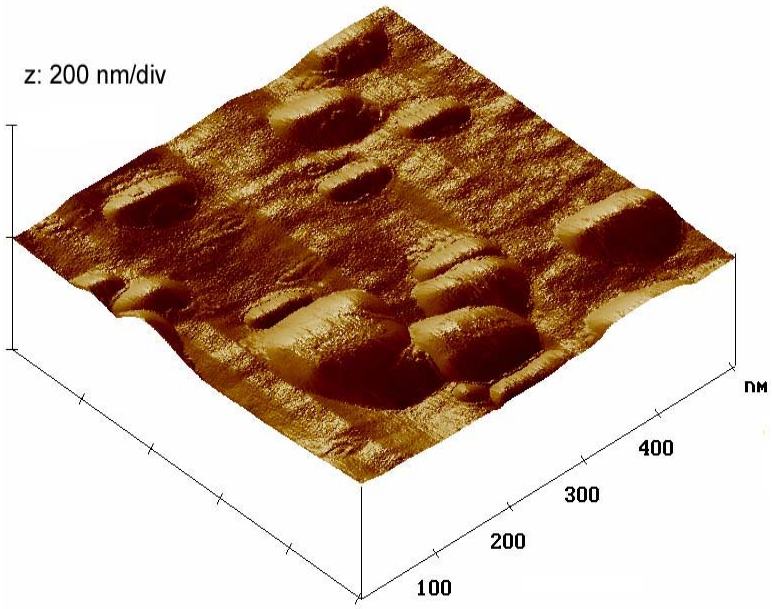

Figure 4.8. AFM image of the initial homoepitaxy sample.

4.3 Heteroepitaxy; initial run and discussion

4.3.1 General

The difficulties noted for GaSb homoepitaxy in the previous section are expected to be considerably more severe for GaSb heteroepitaxy on (001)GaAs. The two materials are chemically compatible, but the lattice mismatch of 7.83% between them is relatively large, which means that the critical thickness is relatively small and that the overlayer material will relax within a few atomic layers. At growth temperatures where the lattice mismatch is large the films will relax by the transformation of the flat film into islands on a pseudo two-dimensional wetting layer. Self-assembled quantum dots can result from this mode of growth, referred to a Stranski-Krastanow [84, 114] (Sec. 2.6.3). Additional tensile strain occurs in the GaSb overlayer on post-growth cooling due to the difference in GaAs and GaSb thermal-expansion coefficients, 5.73×10^{-6} /°C and 7.75×10^{-6}/°C, respectively.

Relaxation will occur through the formation of dislocations, which may or may not propagate through the layer and degrade its properties. The question to be answered is whether real-time optical characterization can provide information about conditions to minimize this degradation. In the later run to be discussed it appears that this is possible.

4.3.2 GaAs initial surface reconstruction

Surface reconstructions of (100) GaAs have been studied extensively during the past few decades for both technological and scientific reasons. The (100) GaAs surface exhibits a wide variety of reconstructions depending on conditions such as temperature or ambient As pressure. [1]. The primary reconstructions are $(2\times4),(4\times2)$, and $c(4\times4)$, which

correspond to terminations of 1, 0 and 2, respectively, layers of As. Among these the (2×4) surface reconstruction has been the most thoroughly investigated, because it is the standard reconstruction for MBE growth. It consists of $\frac{1}{4}$ monolayer (ML) of As dimerized along [110], with every fourth dimer missing to satisfy charge neutrality [115].

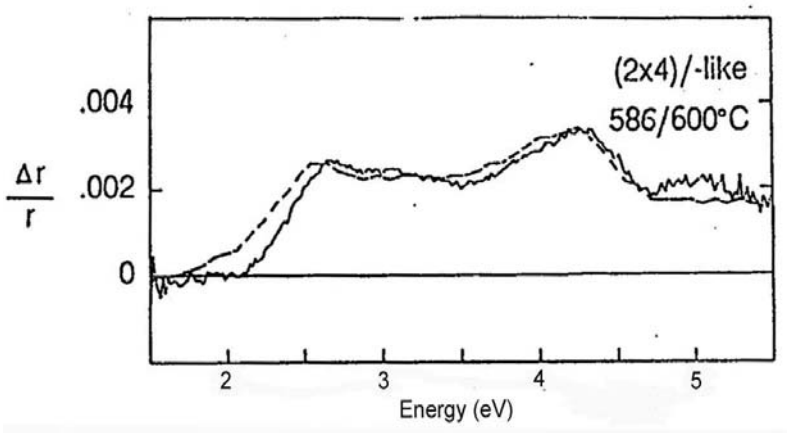

Figure 4.9. RDS spectra of a (100) GaAs surface in UHV (dashed curve) and in an atmospheric-pressure OMCVD reactor (solid curve) (after ref. 1).

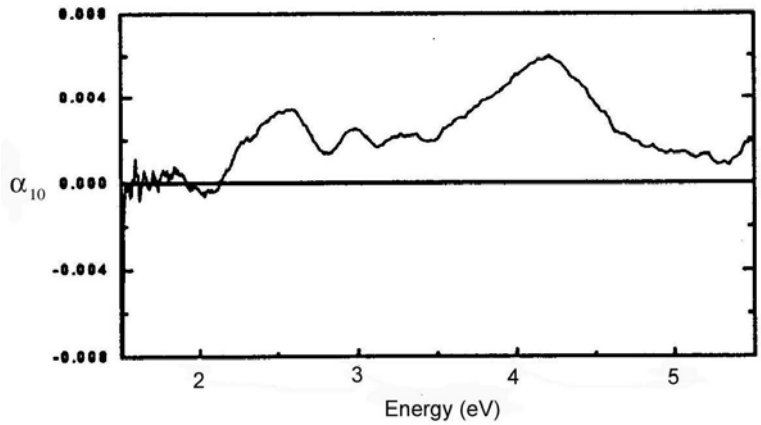

Figure 4.10. α_{10} spectrum of a (2x4) reconstruction of (100) GaAs measured in our reactor.

This reconstruction is formed when the surface is terminated by As, for example by exposing a Ga-terminated (4×2) surface to As. Kamiya et al. [1] were the first to show that the same reconstructions could be obtained in OMCVD, and that in OMCVD growth typically occurred with the surface terminated by 2 layers of As (the c(4x4) reconstruction).

Before our heteroepitaxy experiments we reconfirmed that we could also obtain the As-terminated (2×4)(001) GaAs surface reconstruction by comparing our α_{10} spectra with those reported by Kamiya et al. in ref. [1]. (Fig. 4.9), which is well matched with Kamiya's result. The normal-incidence anisotropy lineshapes $\Delta r/r$ of the (2x4) reconstructions obtained by RDS by Kamiya et al. under MBE and atmospheric-pressure OMCVD growth conditions, shown in Fig. 4.9, can be compared to an α_{10} spectrum in Fig. 4.10, which was obtained on the same reconstruction in our OMCVD system. The lineshapes are clearly related, and show that the amplitude of α_{10} to be about a factor of two larger than the $\Delta r/r$ signals obtained at normal incidence.

4.3.3 Growth results

The $\langle\varepsilon\rangle$ data obtained for a relatively thick layer of GaSb deposited in our initial heteroepitaxy experiment are shown in Fig. 4.11, where they are compared to reference data obtained on the GaAs substrate at the beginning of the run and labeled with the main band-structure features of GaSb. The magnitudes of these spectra are relatively small compared to the GaAs data, and also to the GaSb data shown in Fig. 4.11. A reduced-amplitude spectrum containing all the spectral features of GaSb and none of GaAs is what we expect from a thick layer of GaSb that contains a substantial fraction of voids. Effective-medium theory, which describes a physical mixture of parent material and voids and which we will apply to a later sample, shows this directly.

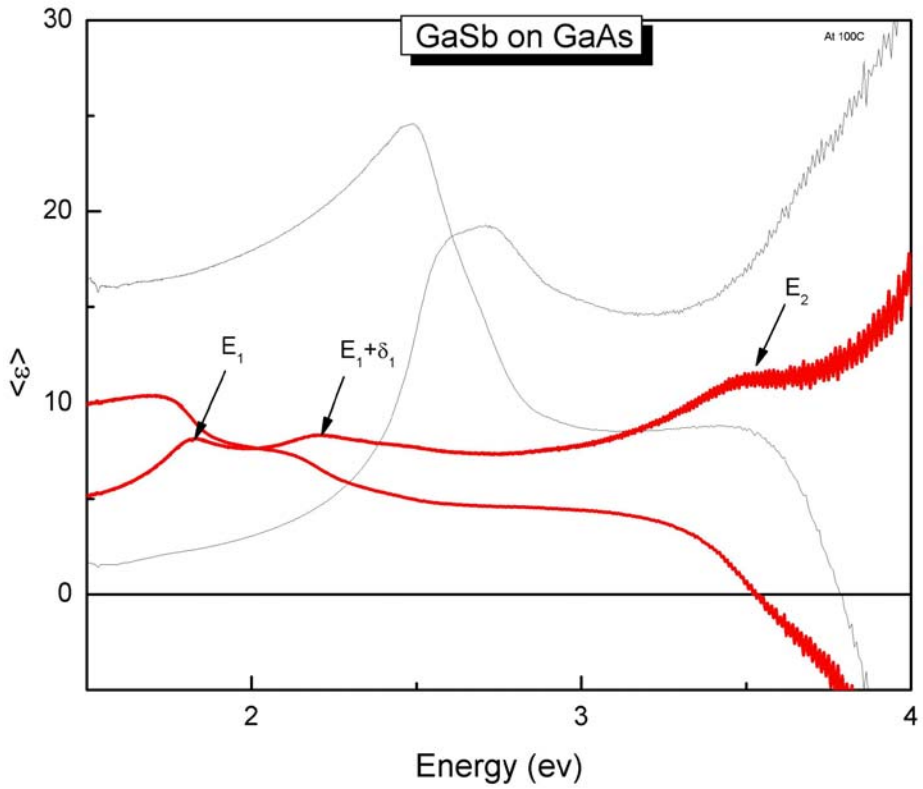

Figure 4.11. Pseudodielectric function of a relatively thick GaSb layer grown heteroepitaxially on GaAs.

4.4.4 Post-growth characterization

Rather than analyze these optical data quantitatively, we restricted our attention to post-growth analyses that would assess the validity of the void-parent material interpretation. To do this we obtained optical and SEM micrographs of the grown layer. Representative optical micrographs are shown in Fig. 4.12 and SEM micrographs in Figs. 4.13 and 4.14. These confirm that the morphology of the GaSb layer as consisting of many small islands. The density of these islands is much higher at the center of the wafer, where the ellipsometric measurements are made, and many of the islands in Fig. 4.14 appear to have coalesced. Most islands at the edge appear circular. However, the islands in the center appear elliptical, suggesting a preferred orientation for growth.

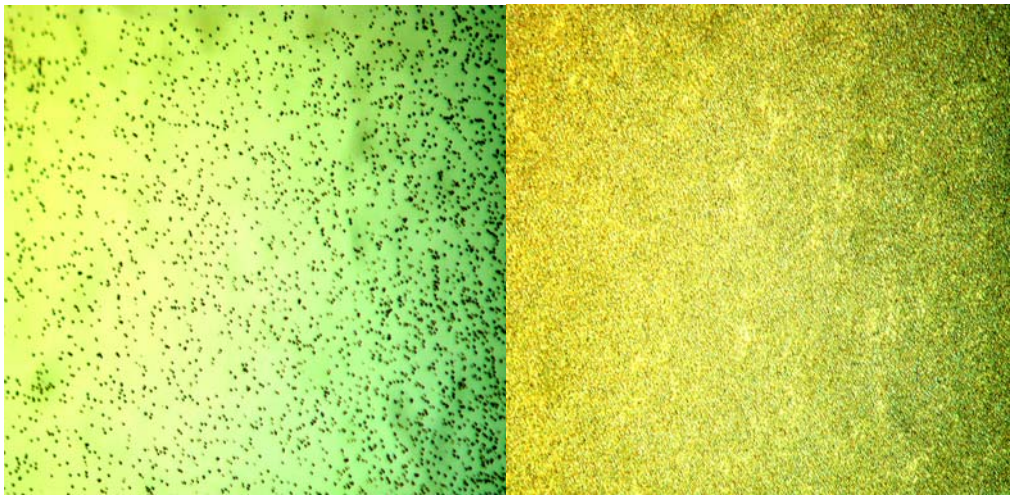

(a) (b)

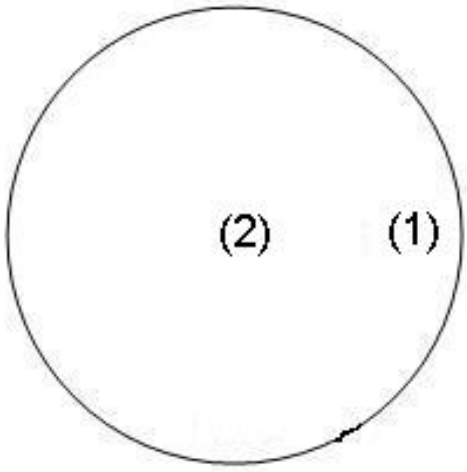

(c)

Figure 4.12. Optical micrographs of the sample discussed in this section. (a) Image of location (1); (b) image of location (2), which corresponds to the location of the ellipsometer beam.

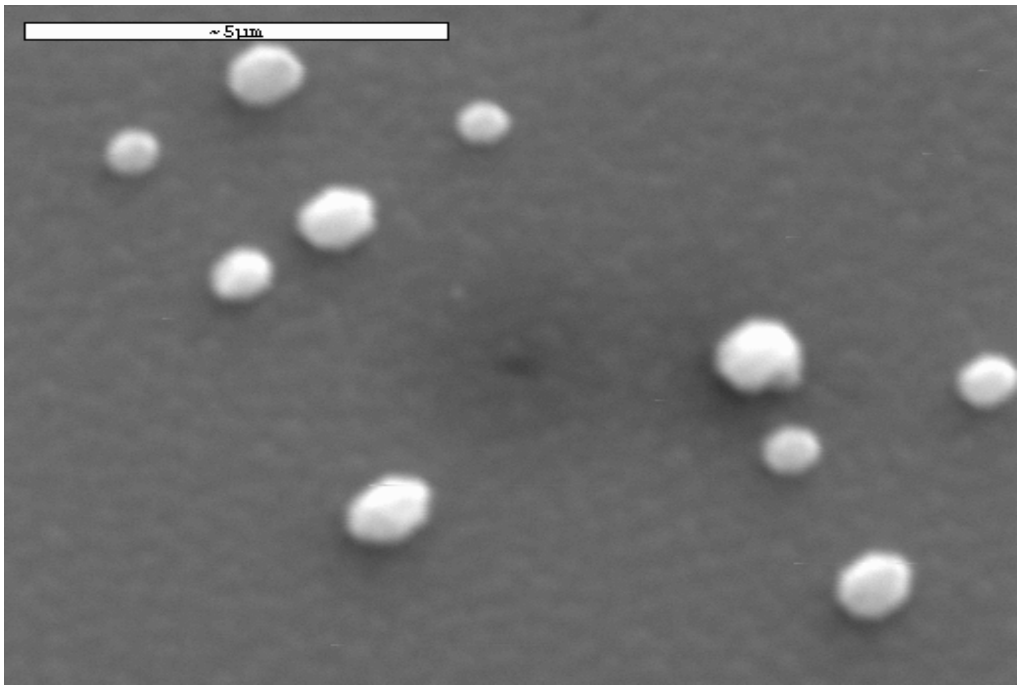

Figure 4.13 . SEM micrograph of a far-edge part of the deposited layer.

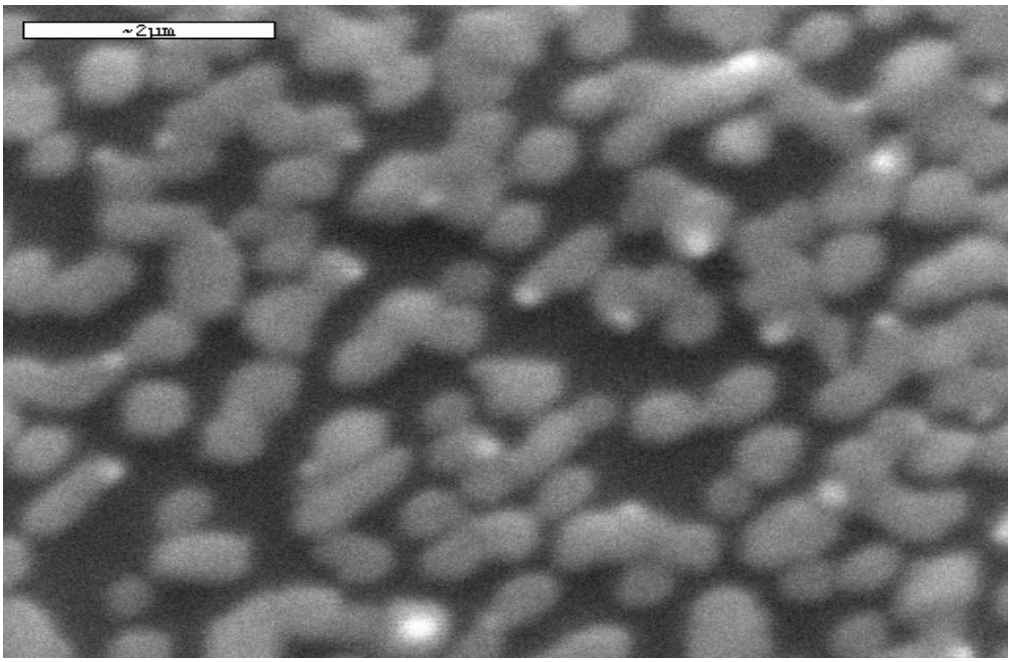

Figure 4.14. SEM micrograph of a central part of the substrate.

The mechanism of island formation at the earliest stage is subsequently replaced by some other evolution mechanism as deposition proceeds. Based upon thermodynamic energy considerations [80] the growth rate of 3D islands would diminish when an island grows to a certain size due to the accumulation of elastic strain energy. As a result, at this stage, smaller islands will grow more rapidly, along with the possible formation of new islands. When the island density increases, the island-induced strain fields in the substrate that help to stabilize coherent larger islands in the first place may begin to interact [81]. At this stage, the interacting strain fields in the substrate and the wetting layer may provide a means to destabilize the initially largest islands by not accommodating as much strain relief in the substrate and thus, from a kinetic viewpoint, decrease the barrier for detachment of atoms from the large islands.

To get a better picture of the amount of Sb present in the film, we performed EDAX measurements. Some results are shown in Figs. 4.15 and 4.16. According to these data the amount of Sb is somewhat different in the different regions. The center region of the wafer showed the highest amount of Sb, consistent with the observed higher density of islands there. These data reveal an rms roughness of 49 nm and a structure that is again similar to what was shown by the other probes.

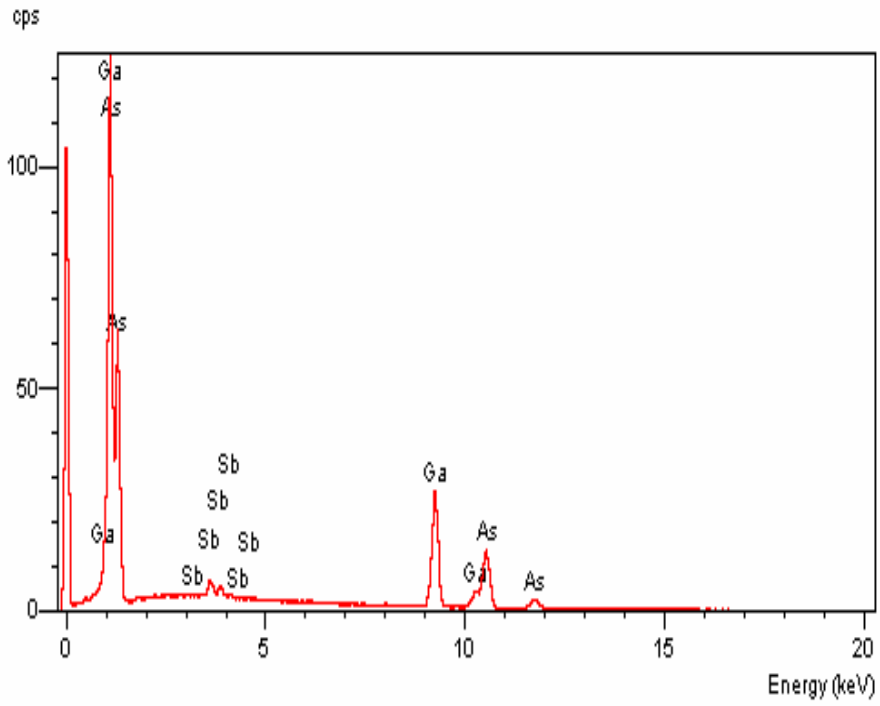

Figure 4.15. EDAX results for the central part of the sample.

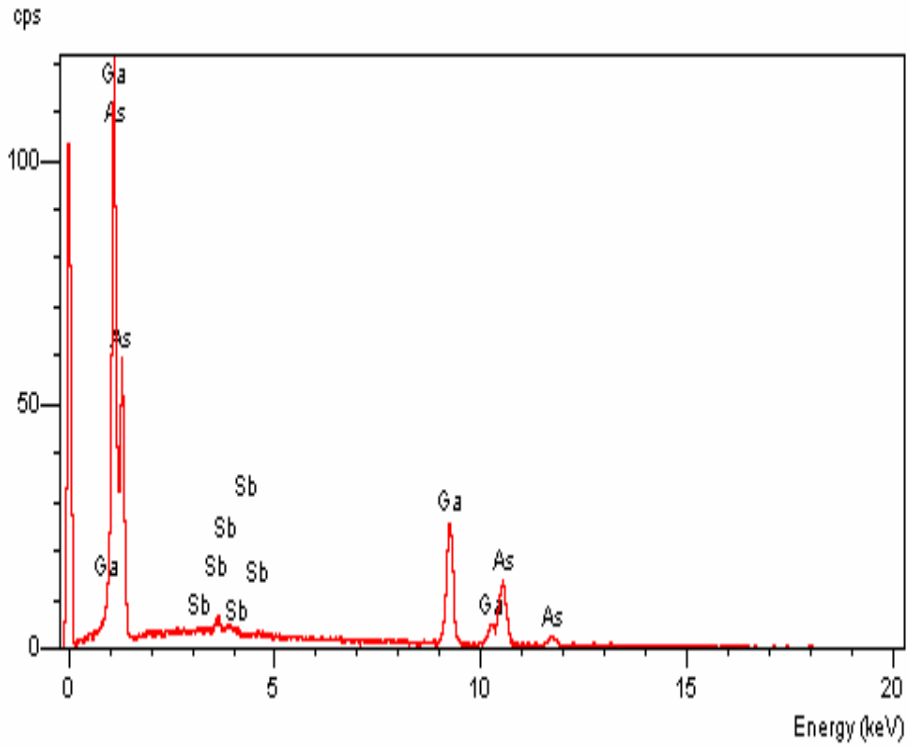

Figure 4.16. The edge part of the wafer.

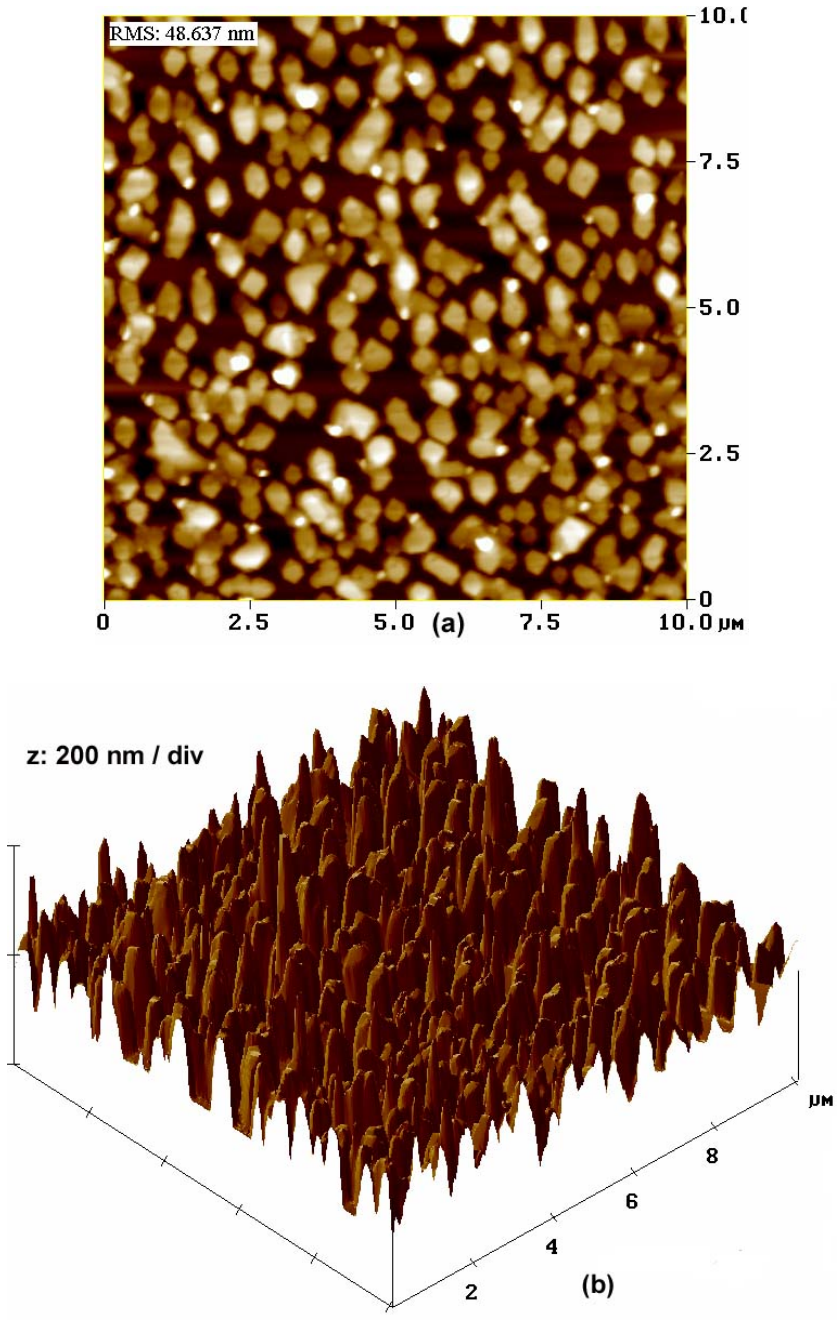

Figure 4.17. AFM images of the Fig. 4. 12 (2) region of the sample.

4.4 Homoepitaxy; final run and discussion

4.4.1 General

As a result of experience gained, we were able to capitalize on real-time optical diagnostics to grow much better material. There were two keys to doing this: (1) ensuring that TMSb was present whenever TMG was introduced to the chamber, thereby avoiding the degradation shown in Sec. 4.2 that occurs when metallic Ga is allowed to accumulate on the surface; and (2) the use of LLS to fine-tune the V/III ratio and therefore optimize the growth surface with respect to macroscopic roughness scattering. The most direct link to surface stoichiometry is through α_{10}, but as shown in the previous section this parameter appears to be too small in the GaSb materials system to be of value as a real-time diagnostic. The connection between surface stoichiometry and the LLS is much weaker and takes much longer to develop, as sufficient material must be grown to be able to detect the roughness.

As in the previously described homoepitaxy experiment, the substrate was an epi-ready nominally undoped (001)GaSb. However, in this experiment growth started normally following oxide desorption. Figure 4.18 shows the $\langle\varepsilon_i\rangle$ spectra obtained in this experiment. We concentrate on the E_2 peak, which occurs at a wavelength of about 300 nm and has an amplitude color-coded in red. As usual, the highest values correspond to the most abrupt (smoothest) surface, but here measured on the microscopic scale. This peak shows a number of high and low spots, corresponding to the results of different V/III flow ratios. Because we cannot actually determine decomposition ratios at the growth surface, the ratio values that follow refer to the TMSb/TMG flow ratio instead. This ratio was varied by varying the TMSb flow under a constant flow of TMG.

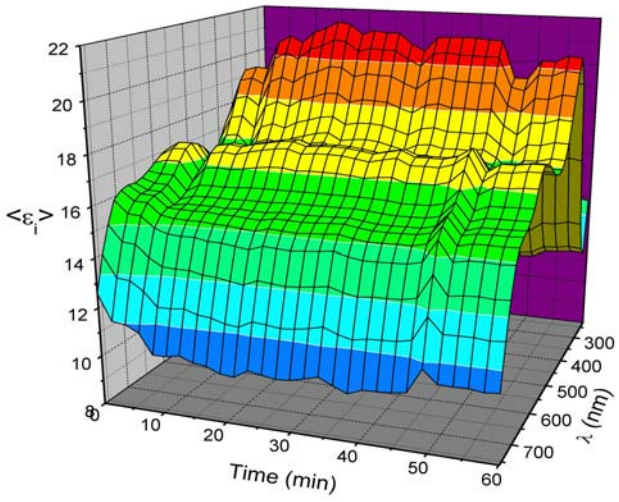

Figure 4.18. 3D dielectric function of GaSb homoepitaxy growth.

We note particularly the flow ratios of 1.6 established at 32 min, 4.1 established at 36 and 54 min, and 6.3 established at 43 min. The smallest and largest are seen to correspond approximately to the onsets of decreases in the E_2 peak, indicating the onset of microscopic roughness. On the other hand, the flow ratio of 4.12 correlates quite well with recovery phases. Since the growing material is identical to the substrate material interference effects are not relevant, so these variations in amplitude can be correlated directly to corresponding variations in the presence of microscopic roughness on the growth surface. What is particularly interesting here is that an adjustment of the flow ratio can reverse the tendency of the surface to roughen, and to initiate a return to the flat condition.

While Fig. 4.18 shows that SE can detect microscopic roughness, we recall that the SE data are affected by many other variables including composition and thickness in multilayer stacks. Accordingly, we also investigated the use of LLS to detect roughness. As a dark-field probe, in principle LLS is not affected by composition or layer thickness. Consequently, if the LLS results can be correlated with those shown in Fig. 4.18 we have an

alternate probe that can be used much more generally, in addition to providing additional information to assist the interpretation of the SE data.

The results, obtained simultaneously with those of Fig. 4.18, are shown in Fig. 4.19. The variations are quite large and correlate quite accurately, although not exactly, with the corresponding variations of the amplitude of the E_2 peak in Fig. 4.18. An exact correlation should probably not be expected because the SE and LLS probes are sensitive to microscopic and macroscopic scattering, respectively. We would expect for example microscopic roughness to form and disappear more quickly than macroscopic roughness owing to the relative scales involved. However, the correlation certainly justifies the interpretation of both responses as due to roughness, and both show that the roughness at the corresponding scales can be reduced as well as enhanced with the proper V/III flow ratio.

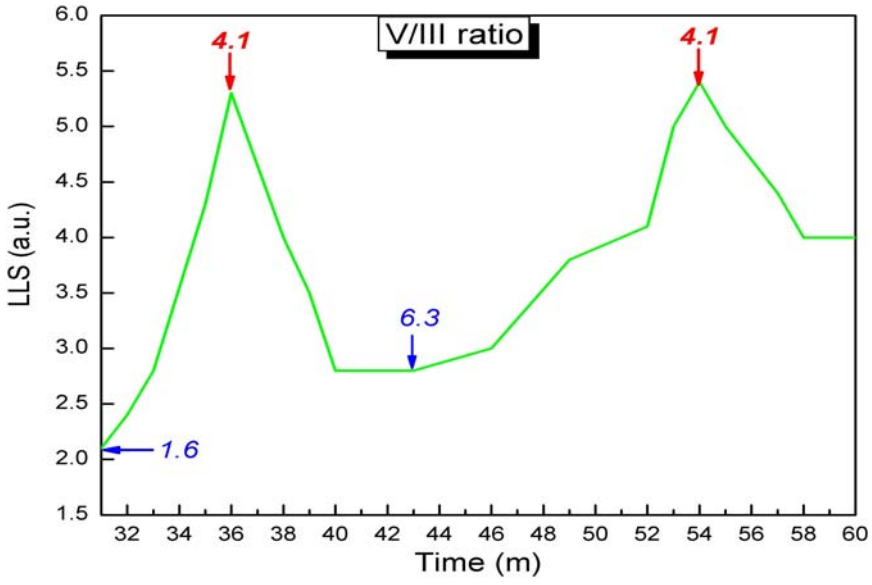

Figure 4.19. Effect of TMSb/TMG flow ratio on macroscopic roughness scattering as determined by LLS.

Post-deposition analyses of this sample show that the deposited layer is much better material. The AFM micrograph, Fig. 4.20, shows an RMS roughness of 0.8 nm at the center

where the layer was monitored. The Nomarski image is shown in Fig. 4.21. An SEM micrograph of a cross section of the sample is shown in Fig. 4.22. The white features are artifacts that were traced to particulate contamination in the reactor and are not relevant for the present analysis. Finally, Fig. 4.23 shows a TEM micrograph of the interface region. It can be seen that the homoepitaxial material continues with no dislocations or grain boundaries.

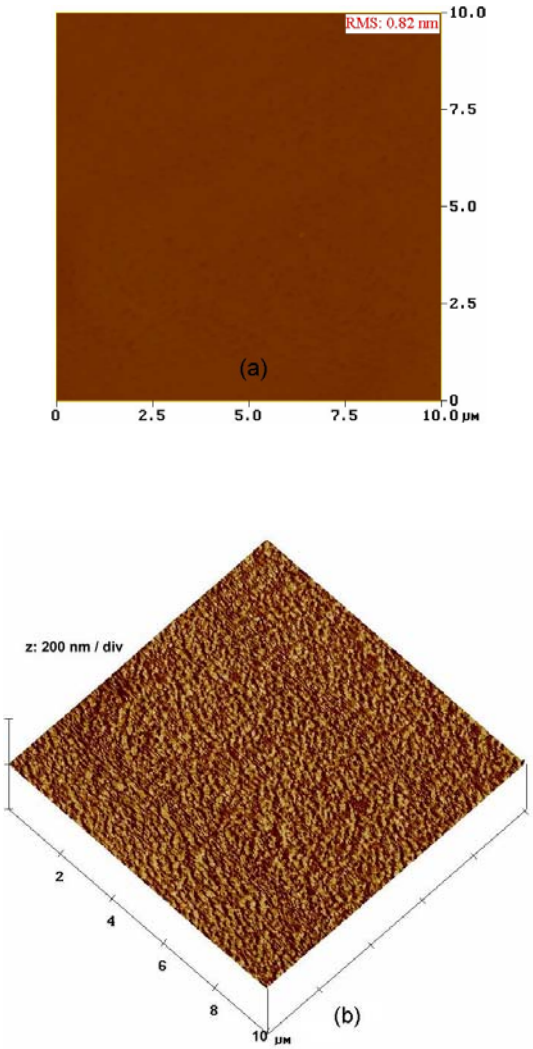

Figure 4.20. AFM images of the homoepitaxial GaSb material: (a) 2D, (b) 3D.

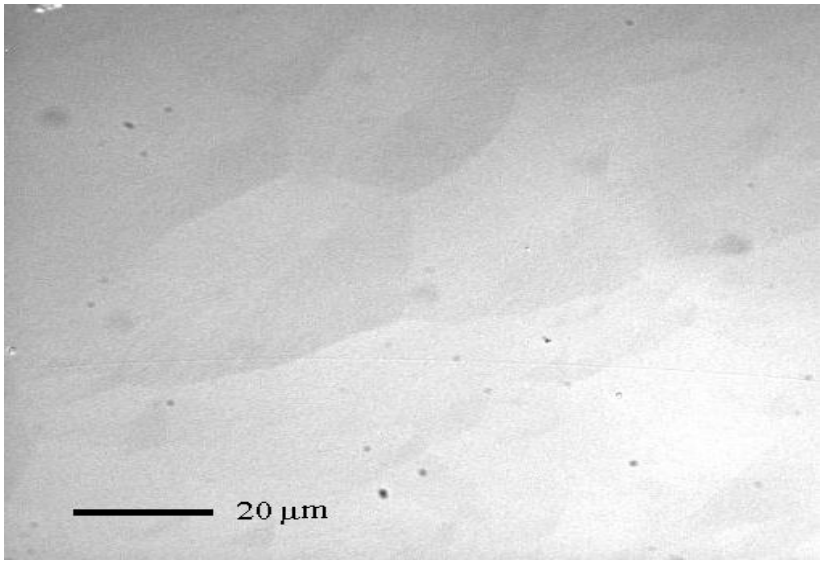

Figure 4.21. Normaski image of as-grown GaSb homoepitaxy.

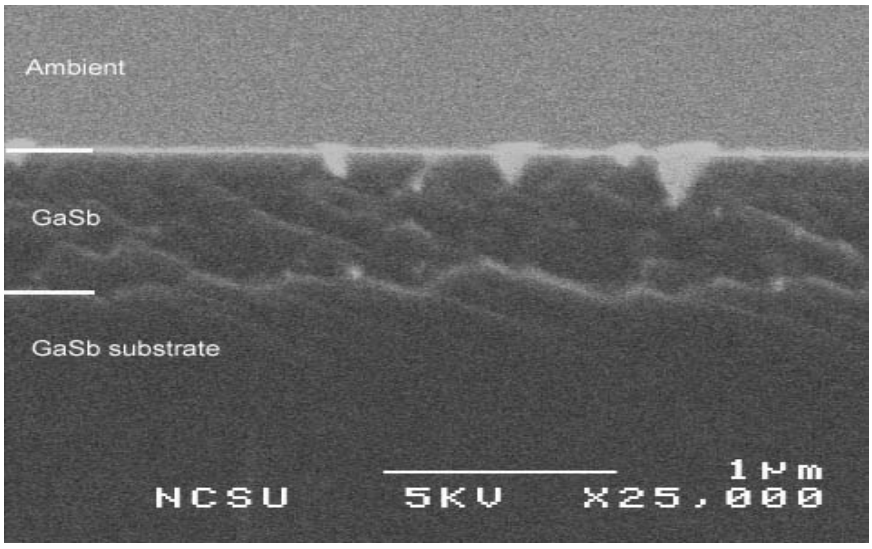

Figure 4.22. SEM image of the homoepitaxial GaSb material.

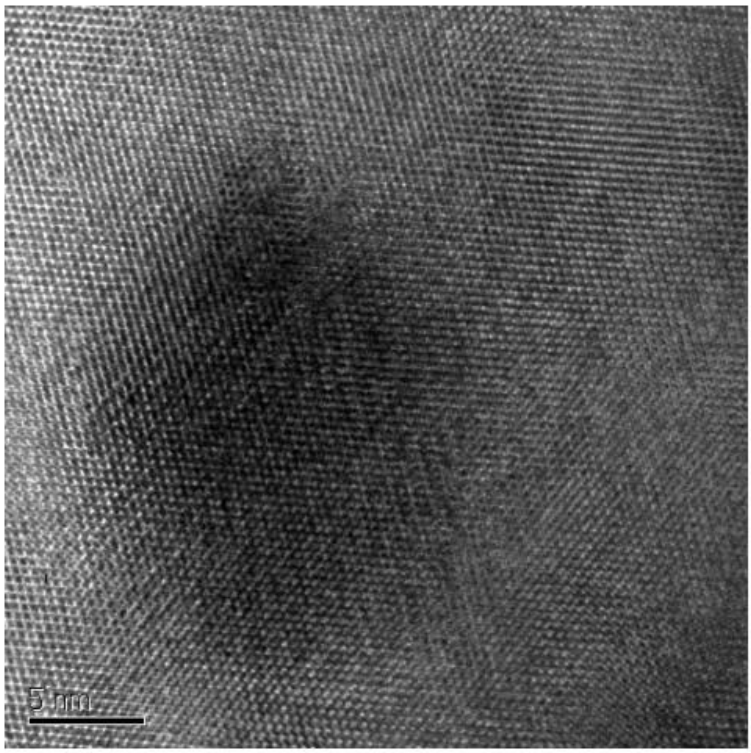

Figure 4.23. TEM image of the interface of the homoepitaxial GaSb material.

4.5 Heteroepitaxy; final run and discussion

4.5.1 General

The result of the growth of a good GaSb layer grown heteroepitaxially on GaAs with real-time monitoring is discussed here. The substrate material is the same as that used in the run described in Sec. 4.2. The same procedure was also followed to remove initial contamination and the oxide overlayers. The real-time growth record is summarized in Figs. 4.24, 4.25, and 4.26, which show the real and imaginary parts of $\langle\varepsilon\rangle$ and the $\langle\varepsilon\rangle$ trajectory at 4.0 eV, respectively. These are shown below and will be discussed in more detail later. The completed sample consisted of a GaAs substrate, a GaAs buffer layer 630 nm thick

grown at an average rate of 5.3 Å/sec, and a heteroepitaxial GaSb overlayer 695 nm thick grown at an average rate of 3.9 Å/sec.

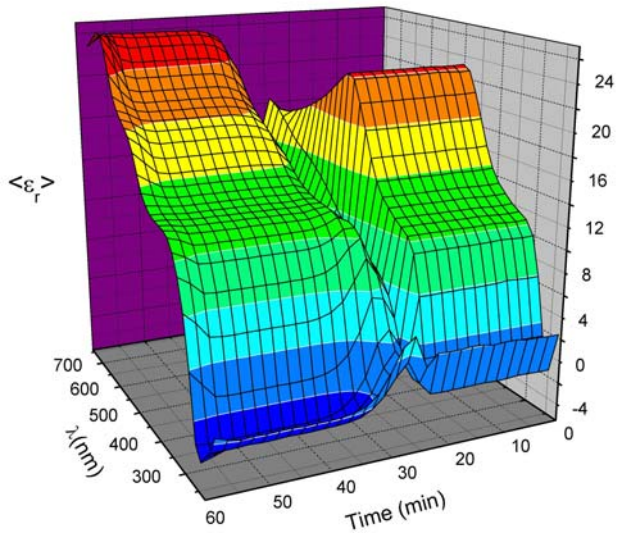

Figure 4.24. Real part of <ε> for GaSb on GaAs.

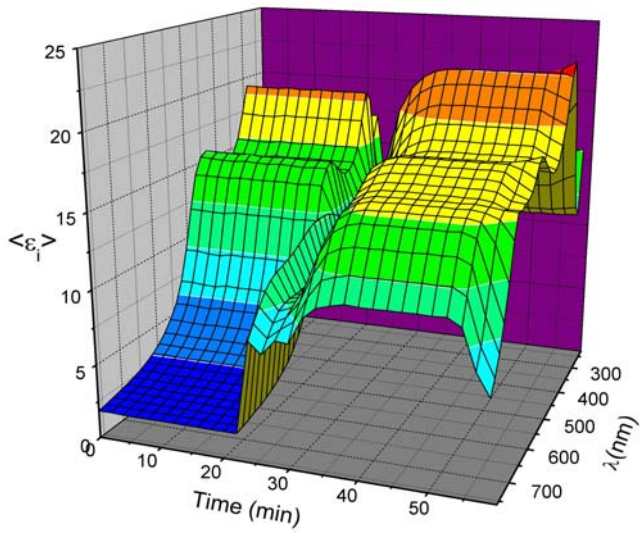

Figure 4.25. Imaginary part of <ε> for GaSb on GaAs.

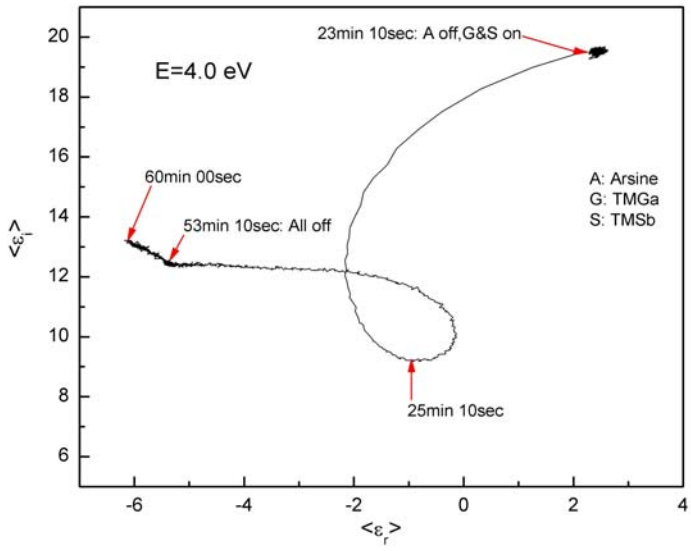

Figure 4.26. Trajectory of real vs. imaginary part of GaSb on GaAs at 4.0 eV.

Deposition began with the 7-min growth of a GaAs buffer layer. Flow parameters were 100 sccm (4.46×10^{-3} mol/sec) AsH_3, 0.3 sccm (1.35×10^{-5} mol/sec) TMGa, and no TMSb. Our intent was then to grow a compositionally graded interface layer by gradually adding TMSb to the precursor flow followed by reducing the flow of AsH_3. To accomplish this the TMSb flow was gradually increased over the next 7 min to 1.24 sccm (5.56×10^{-5} mol/sec). However, as seen in the growth record presented in Figs. 4.24 to 4.25, the <ε> spectra did not change. We next reduced the flow of AsH_3 to 30 sccm (1.34×10^{-4} mol/sec). Again, no change resulted. Finally, at 23 min 10 s into the run we cut off the AsH_3 flow completely with the intention of growing GaSb with the same 4.12 V/III flow ratio that the previous run showed yielded the lowest roughness (Fig.4.19).

The approach succeeded. We grew 695 nm of GaSb that showed excellent epitaxy. TEM micrographs (see below) exhibited the expected dislocations, but these were rather well localized at the interface. Electrical measurements showed the material to be n-type with a carrier concentration of the order of 2 x 10^{16} cm^{-3}, indicating an essentially complete

suppression of Ga antisite defects. While the AFM, XRD, and Nomarski measurements showed the crystalline quality to be less than that obtained in homoepitaxy this is probably not surprising. The fact that the material turned out as well as it did caused us to examine the optical data more carefully, to gain a better understanding of why a mixture of As- and Sb-containing precursors yielded only GaAs over the flow rates accessible to our reactor, and the nature of the heteroepitaxial interface in the nm-scale regime. The structure and formation of interfaces remains an important issue in the growth of III-V heterostructures, since these details affect the morphology of the resulting layer and determine whether heteroepitaxy will be successful or not. To organize a fairly large topic in a logical way we discuss first the post-deposition characterization results, leaving a discussion of the real-time interface data to the end.

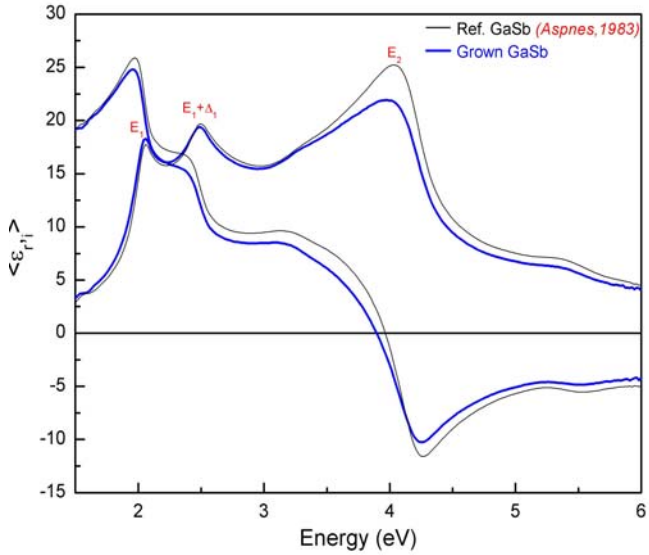

Figure 4.27. Dielectric function of the GaSb layer grown heteroepitaxially on GaAs, compared to reference data on chemically stripped bulk GaSb.

One of the characterization tools that we used was room-temperature SE. The <ε> data obtained for the heteroepitaxial sample after it had been exposed to air are shown in Fig.

4.27. The magnitudes of these spectra are very close to literature reference data [37], which is also shown in the figure. The difference is due to a 1.8 nm thick oxide overlayer, as can easily be shown by the use of the three-phase model. Thus from the perspective of its dielectric function spectrum, the heteroepitaxial overlayer is as good as the bulk material from which the reference spectrum was obtained in Ref. [37].

The surface morphology of the heteroepitaxial layer is illustrated by the AFM data of Fig. 4.28, which present two- and three-dimensional images over a 10×10 μm^2 area, and the Nomarski data of Fig. 4.29. The surface of this heteroepitaxial material is not as smooth as that of the homoepitaxial materials (Sec. 4.4), but this can probably be expected. Both Figs. 4.28(b) and 4.29 show that the roughness is not isotropic but shows a preferred orientation.

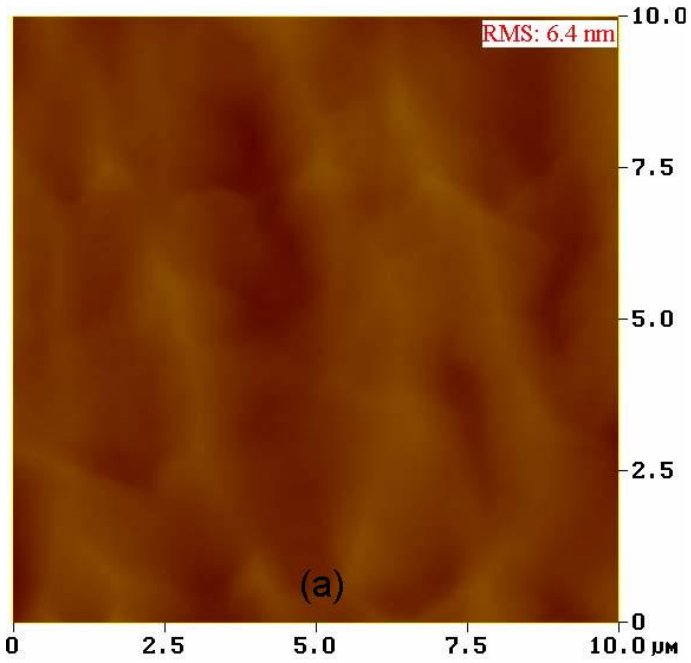

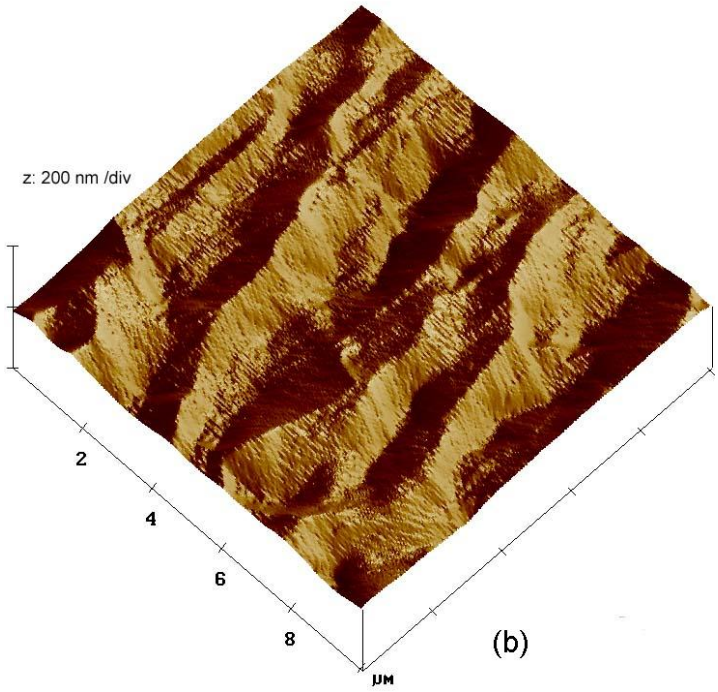

Figure 4.28. AFM images of the GaSb layer grown heteroepitaxially on GaAs. (a): two-dimensional image; (b): three-dimensional image.

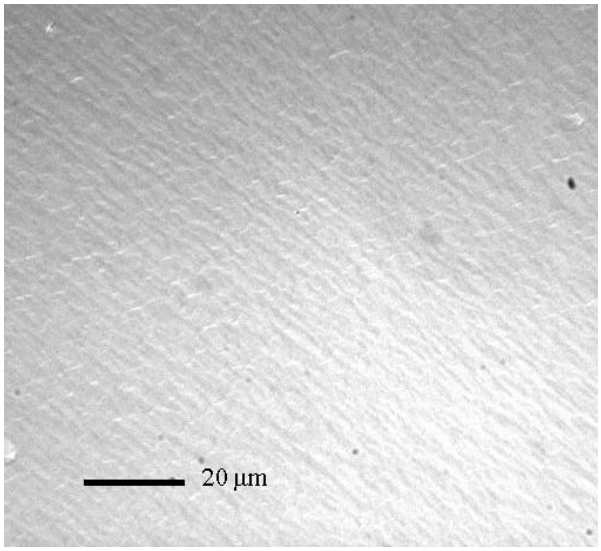

Figure 4.29. Nomarski image of GaSb grown heteroepitaxially on GaAs.

The interface structure is shown in the next two figures, the SEM micrograph of Fig. 4.30 and the TEM micrograph of Fig. 4.31. In contrast to the homoepitaxy result (Fig. 4. 22), the heteroepitaxial sample has an interface of the order of 1 to 2 nm in thickness. The resolution of the SEM micrograph is not sufficient to resolve the interfaces, but the presence of two distinct layers on the GaAs substrate is clear and as a result their thicknesses can be determined with sufficient accuracy. The TEM micrograph shows that the GaAs lattice planes continue across to the GaSb overlayer with the lattice mismatch accommodated by local dislocations only. No threading dislocations appear to be present.

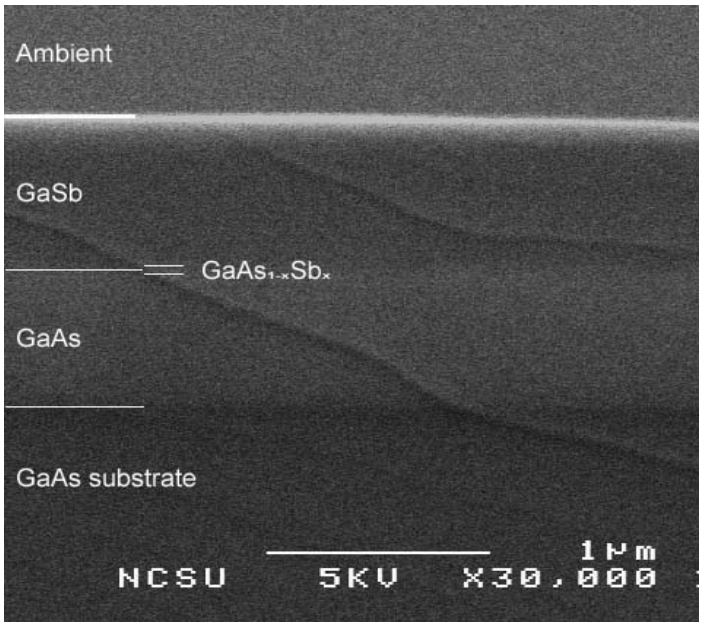

Figure 4.30. SEM cross-sectional image of the GaSb sample grown heteroepitaxially on GaAs.

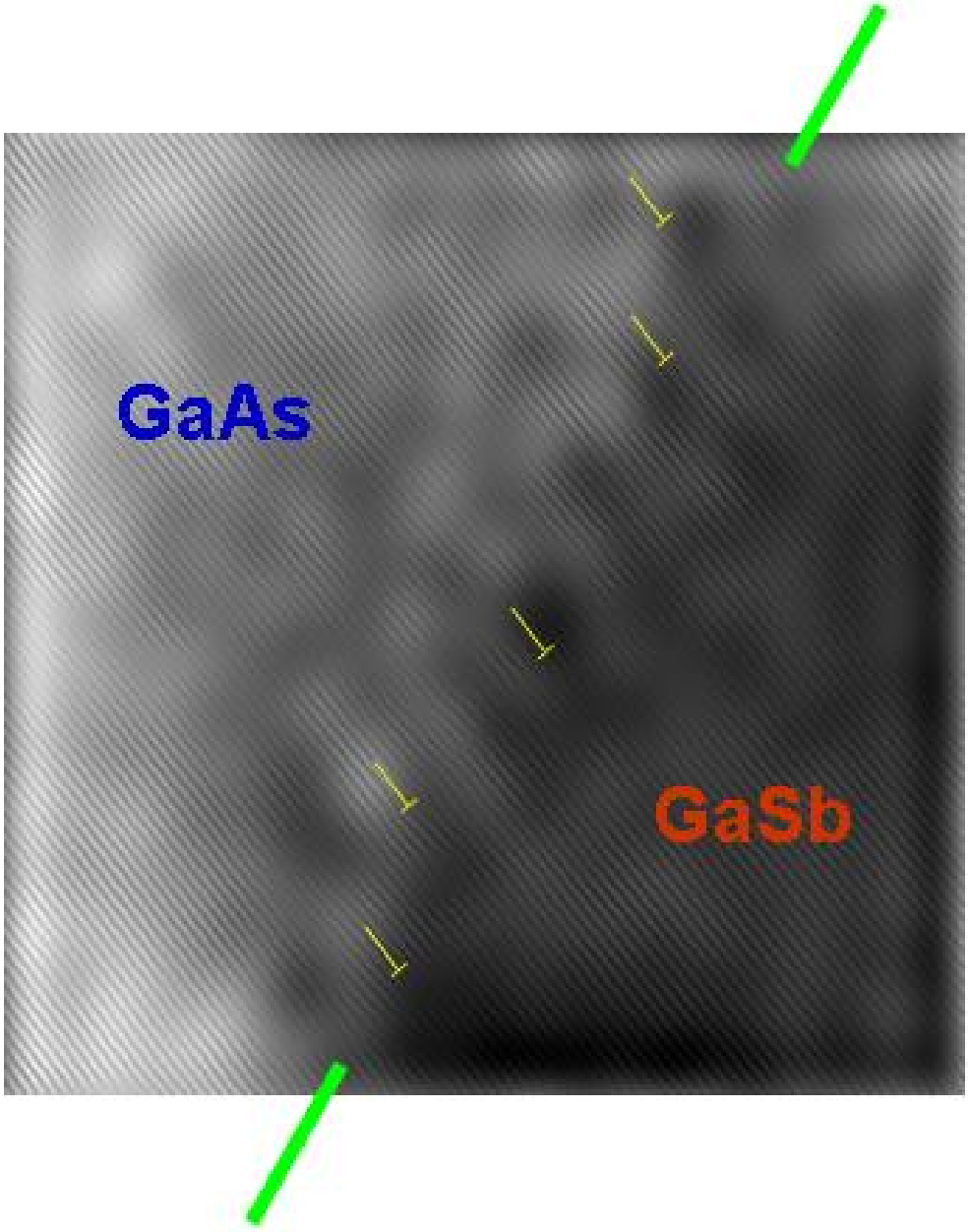

Figure 4.31. TEM micrograph of the GaAs-GaSb interface, with dislocations marked.

The XRD spectra are given in Figs. 4.32 and 4.33, along with an XRD reference file for GaSb. We decided to show both homo- and heteroepitaxial data sets together to facilitate comparison. Both layers show crystallization. However, the width of the rocking curve for the heteroepitaxial sample is broader than that for the homoepitaxial sample. This can be explained as a result of dislocations due to the large lattice mismatch and the resulting compressive strain in the heteroepitaxial material.

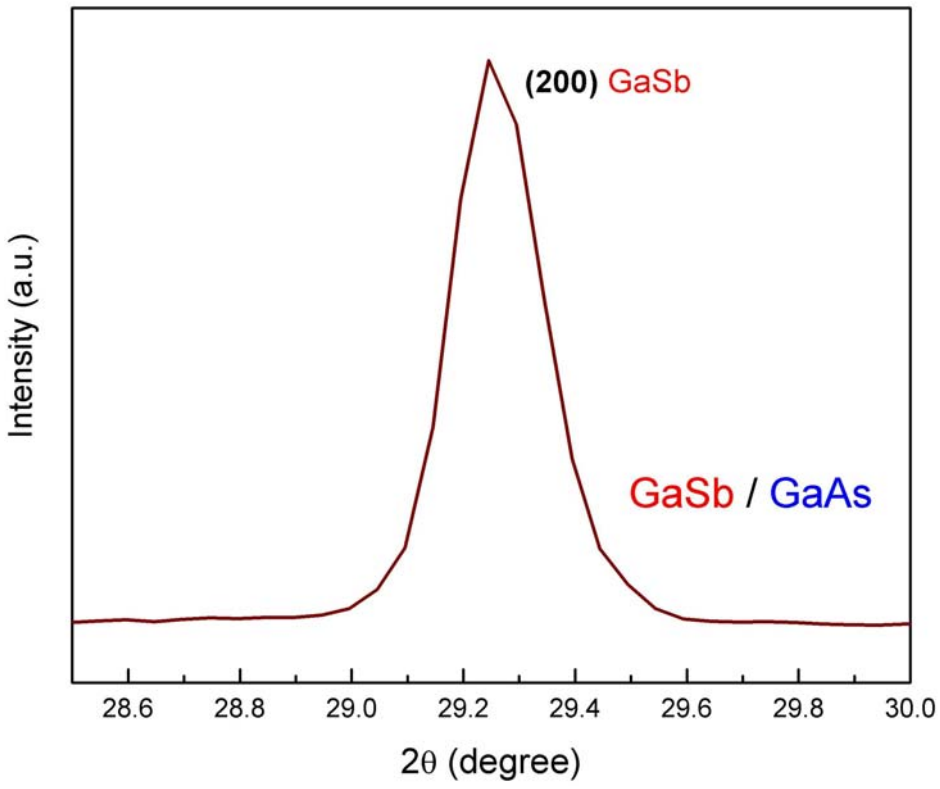

Figure 4.32. XRD data for the final heteroepitaxial sample.

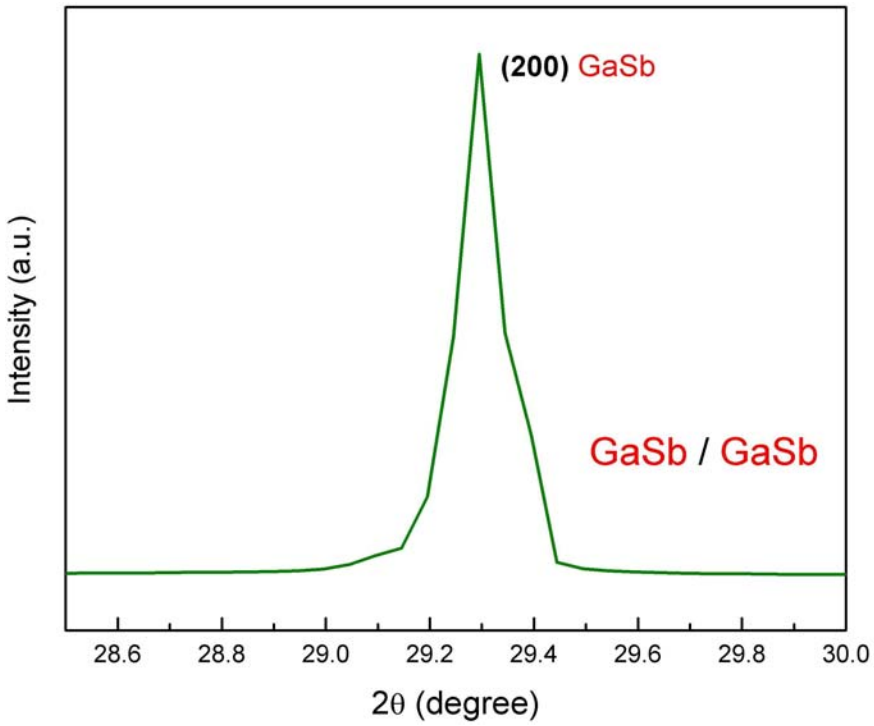

Figure 4.33. XRD data for the final homoepitaxial sample.

GaSb (Gallium antimonide)

Rad. CuKα$_1$ λ 1.5405 **Filter** Ni **d-sp**
Cut off **Int.** Diffractometer **I/I$_{cor.}$**
Ref. *Natl. Bur. Stand. (U.S.), Circ. 539,* **6** 30 (1956)

Sys. Cubic **S.G.** F$\bar{4}$3m (216)
a 6.095 **b** **c** **A** **C**
α **β** **γ** **Z** 4 **mp**
Ref. Ibid.

D$_x$ 5.617 **D$_m$** **SS/FOM** F$_{21}$ = 50(.020,21)

Color Black
Pattern made at 25 C. Spectroscopic analysis shows <0.1% Fe, Si; <0.01% Al, Mg; <0.001% Ba, Ca, Cu, Mn. Dodecahedral cleavage. Validated by a calculated pattern. Ozolinsh et al., *Kristallogr.*, **8** 272 (1963) report: a = 6.09612(9) at 25 C. SZn type. PSC: cF8.

d Å	Int	hkl	2θ
3.52	100	111	25.27
3.048	12	200	29.27
2.156	65	220	41.85
1.838	45	311	49.53
1.759	4	222	51.92
1.524	12	400	60.69
1.399	18	331	
1.363	4	420	
1.244	20	422	
1.1738	10	511	
1.0776	6	440	
1.0304	10	531	
1.0158	1	600	
0.9638	4	620	
0.9294	6	533	
0.9188	2	622	
0.8796	2	444	
0.8534	6	551	
0.8452	2	640	
0.8144	8	642	
0.7936	8	731	

Figure 4.34. Powder diffraction file of GaSb.

As a final check on material quality, we performed electrical measurements on the heteroepitaxial material to determine carrier type and concentration. Most defects are not electrically active in a way that leads to direct identification, but the Ga antisite in GaSb is an exception because each antisite defect generates in principle two holes, making the material strongly p-type if enough are present. Thus a 4-point probe measurement is sufficient to determine whether these antisite defects are indeed present. The grown GaSb overlayer exhibited n-type conductivity and a carrier concentration of $2.4 \times 10^{16}/cm^3$. This reveals that Ga antisite defect was suppressed.

4.5.2 Analysis of the real-time data; details of heteroepitaxial growth.

The first surprising result was our inability to grow a compositionally graded interface with available precursor flows. As mentioned above, there is no evidence of any Sb incorporation into the GaAs buffer layer even though for 14 min both AsH_3 and TMSb were present as precursors, with final relative net flow rates of 30 and 1.24 sccm.

While this is apparent particularly in Fig. 4.35 (the point at about 2 + i19.5 contains 23 min of data), we can emphasize this further by the data shown in Fig. 4.36. This figure is the superposition of 10 real-time spectra obtained at different times during the run, along with some precursor flow settings during this interval. The 10 spectra superimpose to within the width of the trace, which is essentially the noise level of the system. An admixture of even 1% Sb would have resulted in a measurable shift of the E_1 and $E_1 + \Delta_1$ transitions near 2.8 eV. Such a shift is clearly not seen, so we can conclude that the amount of Sb incorporated up to that time is below the level of detection.

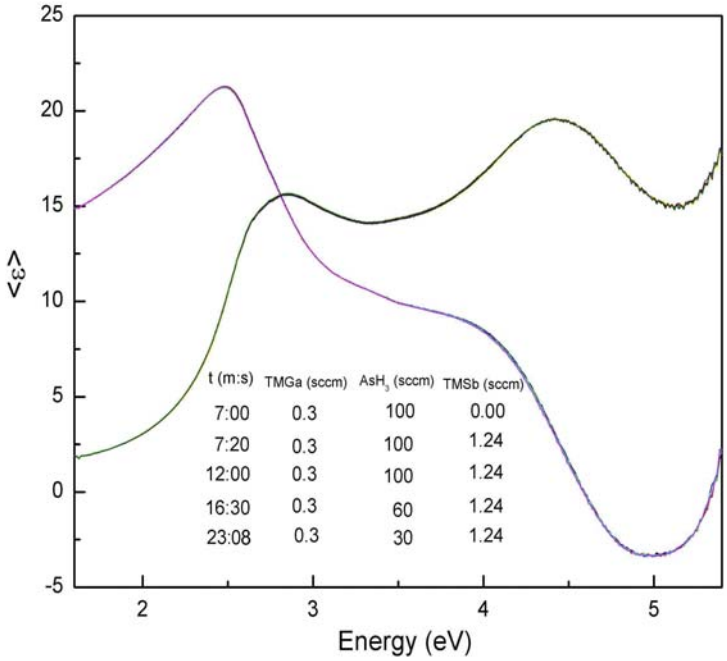

Figure 4.35. Real-time < > spectra of the GaAs buffer layer with precursor flows as indicated.

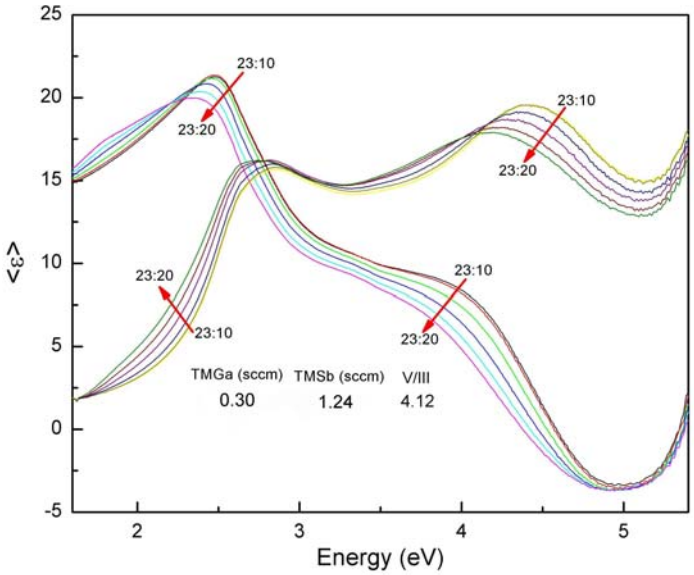

Figure 4.36. Dielectric function spectra of GaSb on GaAs at the beginning of heteroepitaxy. The spectra are separated by 2 s intervals.

These results are actually consistent to what is known about the relative tendency of As and Sb to incorporate in a growing crystal. First, the As-Ga bond is favorable simply through bond strength [116]. The energy of a Ga-As bond in GaAs, 210.0 kJ/mol, is stronger than that of a Ga-Sb bond in GaSb, 191.6 kJ/mol [117]. Therefore, As incorporation will be preferred over Sb incorporation. Cao et al. [118] have reported experimental confirmation in measurements of AlGaSb alloy growth. Second, the difference in anion size and the smaller lattice constant of GaAs will act to exclude Sb. The growth of $GaAs_{1-x}$ Sb_x on InP is complicated by the large miscibility gap of this alloy system, ranging from x ≈0.2 to 0.8 for typical growth temperatures and near-equilibrium growth conditions [119]

We now take a more detailed look at interface formation. Figure 4.35 shows 6 spectra obtained at 2 s intervals just after AsH_3 flow was terminated. The initial spectrum at 23:10 min after the start of the run is characteristic of bulk GaAs at the growth temperature (see Fig. 4.34). The spectrum at 23:12 shows only minor differences. However, significant changes are seen thereafter, with the E_2 peak of $\langle\varepsilon_i\rangle$ shifting to lower values and lower energies, and the E_1 threshold of $\langle\varepsilon_i\rangle$ near 2.5 eV also beginning to shift to lower energies. These behaviors are both characteristic of the growth of a material with lower transition energies and with a lower value of the E_2 peak of $\langle\varepsilon_i\rangle$.

Figure 4.37 shows the results of a detailed analysis of the spectrum obtained at 23:20 min., i.e., after approximately 10 s of deposition (black lines). To do that we assume that the 3-phase model discussed in Ch. 2 is applicable, and use it to model $\langle\varepsilon\rangle$ in terms of the overlayer dielectric function ε_o and thickness d, the void fraction f_v, a possible GaAs fraction f_{GaAs}, wavelength λ, and other system parameters such as the angle of incidence. The result of the fitting process are d, f_v , and f_{GaAs} (if used), where $f_{void} + f_{GaAs} + f_{GaSb} = 1$. Here, ε_o was

generated using the Bruggeman effective medium approximation (EMA), which assumes that the constituents are physically mixed, i.e., that they occur in large enough volumes to retain their own dielectric identities (at least one dimension being of the order of 2 nm in length). The ambient dielectric function is taken to be 1.

The original GaAs spectrum at 23:10 min is shown in green, to provide a measure of the goodness of fit relative to the changes that occurred in these 10 s. Although the 23:10 and the prior 23:08 min spectrum were identical except for noise, we used the prior spectrum to represent the substrate, as it is 2 s further away from any possible contamination with Sb. The first fit was done with the overlayer assumed to consist of only crystalline GaSb and voids. The results showed a 1.93 nm thick layer with 29% voids and 71% GaSb, and the fitting procedure yielded a mean-square residual of 0.5324.

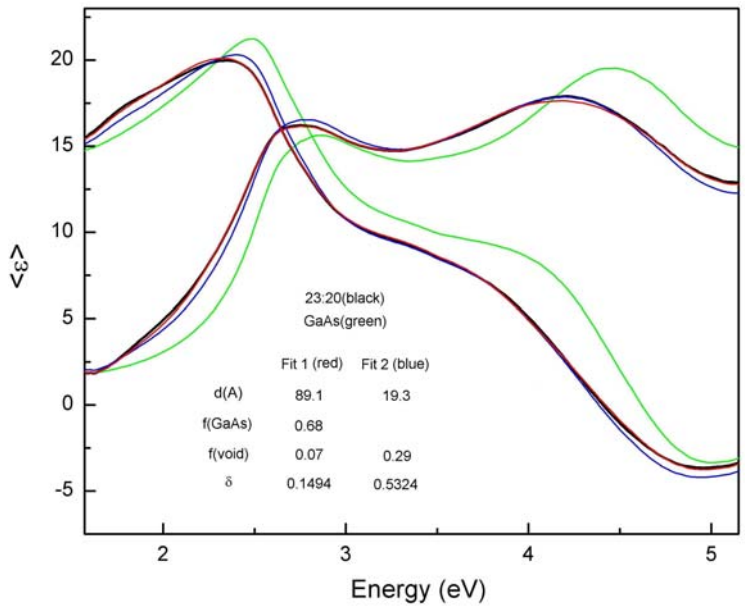

Figure 4.37. Curve fit.

In the second model we assumed that the deposited overlayer contained in addition crystalline GaAs. The fit here is shown as the red line, and indicates a 8.9 nm thick layer with 68% GaAs, 7% void, and therefore 25% GaSb. The residual, 0.1494, is better by more than a factor of 3, indicating that at least during the initial phase of heteroepitaxy a considerable amount of GaAs is still being incorporated into what the fitting model views as the overlayer. This may not be unreasonable owing to the previously demonstrated preference for As incorporation coupled with the fact that gas switching in the OMCVD reactor is certainly not instantaneous. If we multiply the volume fraction of GaSb with the model thickness we obtain an effective GaSb thickness of 2.19 nm.

These thickness values are at first sight surprising, given the average growth-rate value of 3.9 Angstrom/s for the GaSb layer. If GaSb were being incorporated at the average rate we would expect 3.9 nm 10 s after the start of growth. However, we believe that this reduced value is further evidence of GaAs growth during this time, with the preferential incorporation of As and the exclusion of Sb. In this picture the overall thickness of 8.9 nm is also misleading, and is probably a manifestation of the fact that at least some of the mixing might be chemical, i.e., in the form of an alloy mixed on the atomic scale, whereas the Bruggeman model assumes that the mixing is physical.

We assessed this possibility as well by analyzing the 23:20 min spectrum in a second way, assuming the three-phase model is valid and solving for the dielectric function ε_o of the overlayer by equating the model to the data. The model is then solved numerically for ε_o assuming a particular value of d. This avoids making any assumptions about the nature of the overlayer itself. However, since d is not known a priori and as the above data clearly show, probably cannot be inferred from the deposition rate, we invert the model for a range

of thicknesses starting with the effective GaSb layer thickness 2.19 nm estimated from the best-fit parameters and ending with the overall best-fit thickness of 8.9 nm. The resulting spectra are shown in Fig. 4.38. The interesting aspect of these results is that at the lower end of the range ε_o clearly shows the E_1 and $E_1 + \Delta_1$ structures of bulk GaSb, unambiguously indicating the presence of bulk GaSb in the layer. Thus GaSb as relatively pure crystalline material already has a measurable presence within the first 10 s, even if the layer is actually a more complicated mixture of GaAs, GaSb, and voids. It can be added that this amount of GaSb continues to be obtained to within about 20% for different models, probably because this much is needed to reproduce the unambiguous character of the E_1 and $E_1 + \Delta_1$ spectral structures in $\langle\varepsilon\rangle$.

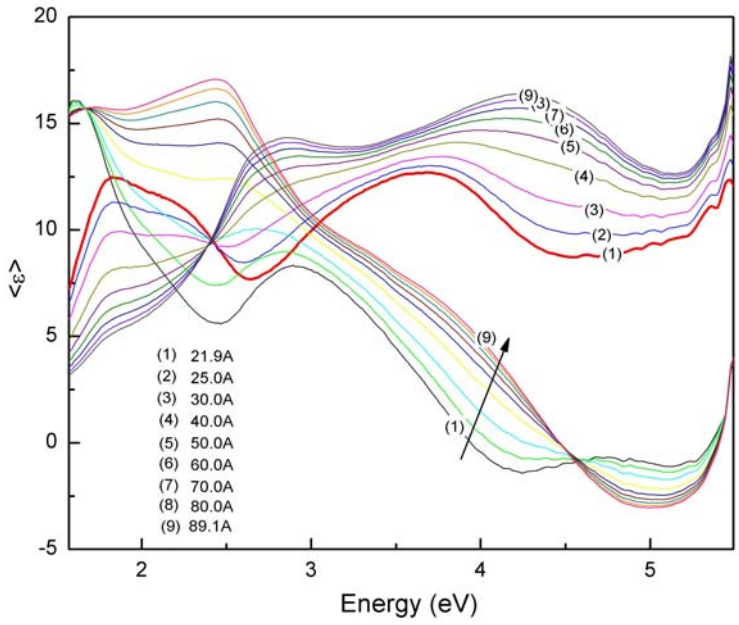

Figure 4.38. Solutions of the three-phase model for the overlayer dielectric function ε_o for different assumed values of the overlayer thickness d.

By performing a similar curve-fitting analysis on the data obtained during the initial phase of heteroepitaxy we can estimate the growth rate of the GaSb fraction. These results

are summarized in Fig. 4.39. We note that the growth rate of the GaSb fraction soon reaches a realistic value, corresponding to the average growth rate expected for the material.

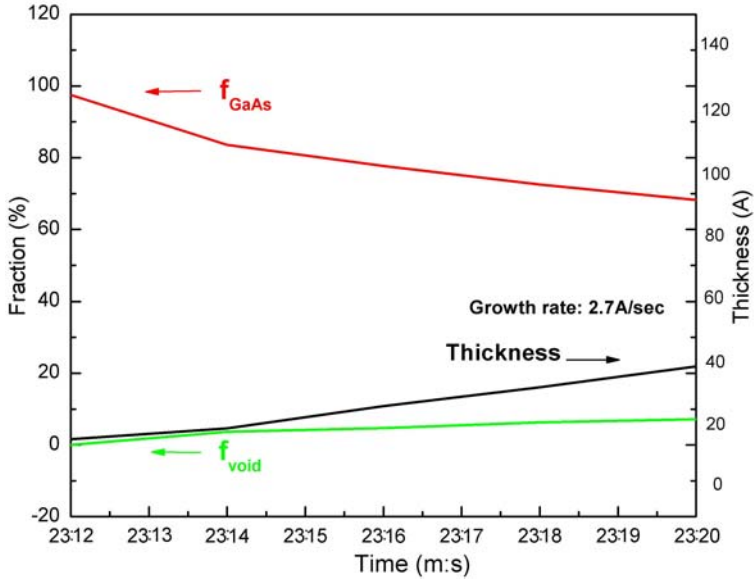

Figure 4.39. The trend of thickness, GaAs fraction, and void fraction in the interface for the initial stage of heteroepitaxy.

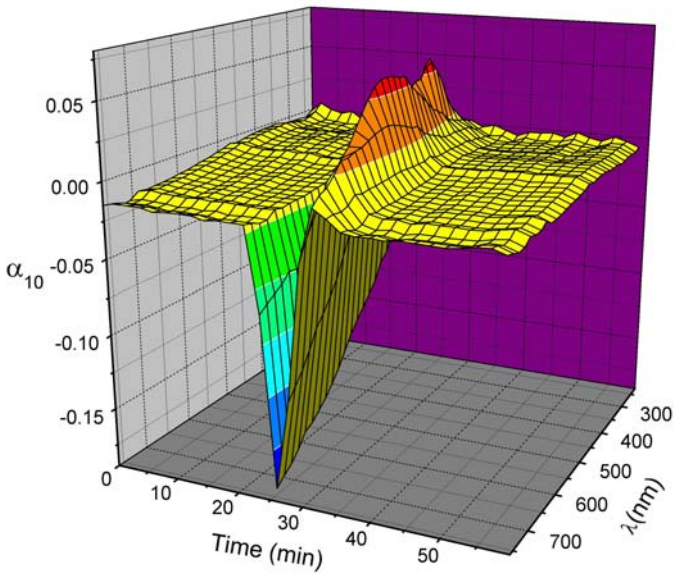

Figure 4.40. α_{10}

Considering the later stages, the data of Figs. 4.24 – 4.26 indicate that the next phase of heteroepitaxy yields greatly reduced values of <ε>, indicating an increasing volume fraction of voids followed by a gradual reduction and convergence to good material. This is expected from Stranski-Krastinov growth, where the islands first form, then increase in both size and height, then coalesce, with the voids finally filling in with further growth. The presence of islands is confirmed by the α_{10} data shown in Fig. 4.40. By comparison of the scale of the signals seen here with the chemical effects shown in Fig. 4.40, it is clear that these large amplitudes must be due to structural rather than chemical effects. The appearance of elongated islands is consistent with the AFM results shown in Fig. 4.28 (b), which also show evidence of a preferred orientation for growth.

4.5.3 GaP growth

It is well known that GaP is not chemically matched to Si but they are nearly lattice-matched heteroepitaxial system.

We investigated the behavior of Ga diffusion prior to the growth of GaP on Si(100) substrate and in particular obtain the first data in a "burst" mode that is nonequilibrium state. GaP was grown at 750^{o}C.

In Fig.4.41 is representative plot of the pseudodielectric function during dosing and recovery. Experiments were performed at 750^{o}C. Completely back to normal state (1), then 0.5 sccm of TMGa was dosed for 1 second, showing deteriorating the surface (2)and (6), then the surface became recovered after 200sccm of PH_3 was dropped giving 397.6 of the V/III mole ratio,(3), (7), continuously being recovered (4), then back to original condition (5).

PH_3 possibly etches Si substrate, then the surface of the substrate got rough, making dielectric function of Si go down. At high temperature, even H_2 may etch Si surface. Obviously, when the surface is rough the mobility decreases.

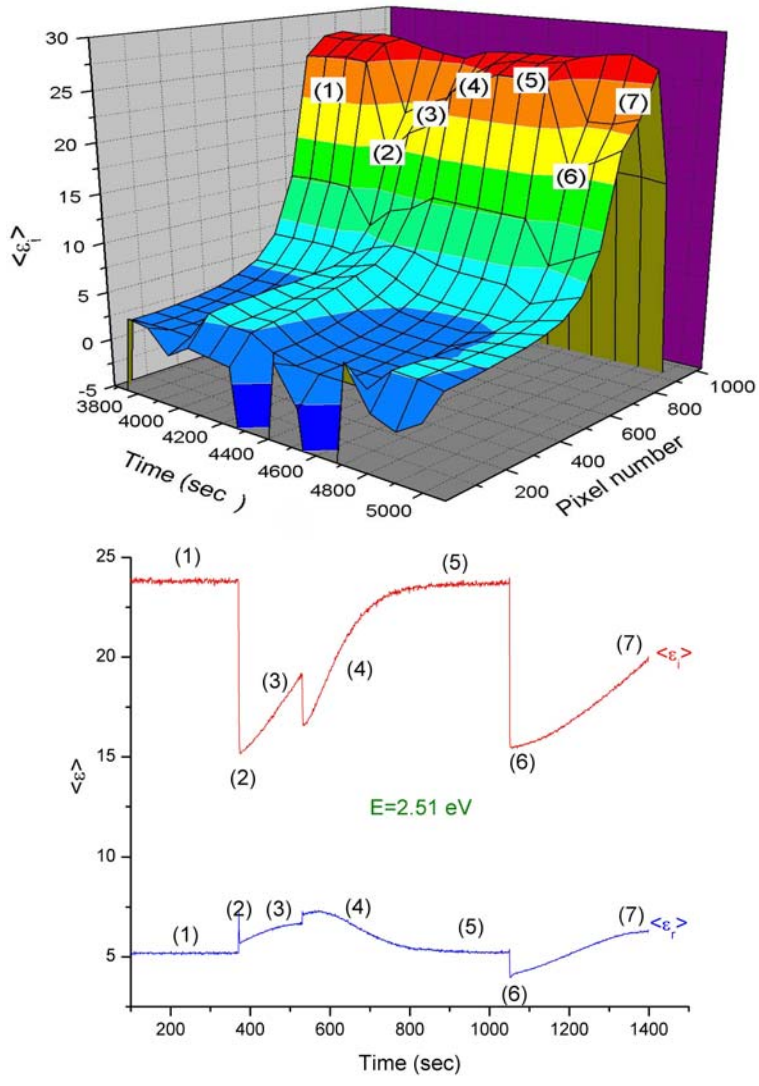

Figure 4.41. GaP growth on Si

Chapter 5 Conclusions

In this work we studied various aspects of the homoepitaxial and heteroepitaxial growth primarily of GaSb, although some work was also done on GaP on Si. Our primary tool was an integrated OMCVD/RDS/SE/LLS system built around a modified commercial Emcore GS3300 OMCVD reactor, which allowed us to get real-time optical data about homoepitaxial and heteroepitaxial growth from 240 to 840 nm at a rate of 4 Hz. The integrated system was originally configured to return spectroscopic ellipsometric and optical-anisotropy data using the same optical beam, which was accomplished by synchronizing the rotation rates of the sample and the rotating compensator of the ellipsometer.

However, we discovered that the optical anisotropy of GaSb, which in principle gives information about the chemical configuration of the outermost layer, was too small to be useful, especially since with arbitrary V/III flow ratios growth resulted in a rough surface that gave larger signals. As a result we added a laser light scattering (LLS) configuration to the system to access macroscopic roughness, and thereby provide indirect information about surface stoichiometry that allowed us to optimize it while growth was occurring.

By comparing our initial and final results in both homoepitaxy and heteroepitaxy, we demonstrated directly that optical diagnostics were necessary to ensure the growth of good GaSb. As additional evidence, this good material was not uniformly deposited over the wafer, but only in the region where we were monitoring it. This confirms what is already well known, that owing to the nonvolatility of Sb good GaSb is not easy to grow. However, by monitoring growth we can adjust conditions in real time to get good material. A key aspect that allowed us to obtain optimum V/III flow ratios was the introduction of LLS as mentioned above. Detailed modeling of the optical data for the initial stages of heteroepitaxy

on GaAs showed a considerable amount of GaAs to be present certainly for the first several nm, but also showed (2) the unambiguous presence of crystalline GaSb. The slower growth rate of GaSb compared to the average value observed for the full 695 nm layer was consistent with the inability of Sb to incorporate into the GaAs during the growth of the buffer layer.

This work also involves at least two other firsts: (1) the first time that SE has been used to examine growth of GaSb in real time, and (2) the first time that LLS has been used to optimize growth conditions during growth. Although real-time optical diagnostics have been used before on GaSb growth, prior work was limited to RDS, which as we have shown does not yield the desired information about chemical bonding because the associated signals are small and tend to be obscured by the much larger structural anisotropies that result from growth with nonstoichiometric surfaces. Not surprisingly, the prior work essentially yielded null results.

Contrary to expectations, our experiments also showed that Sb deposition on the growth surface as a result of TMG decomposition was actually to a certain extent self-limiting, probably because the last stage of TMG decomposition, the ejection of the final methyl group, does not occur unless a surface Ga is available for bonding. This result follows directly from the real-time SE data, which reveals a collapse of $\langle\varepsilon\rangle$ when the surface is exposed to TMG in the absence of TMSb in the carrier stream, but no change when exposed to TMSb in the absence of TMG. This is direct evidence that TMG will react with the surface under any of the conditions used here to deposit excess Ga and thereby degrade the material, but TMSb will react only if Ga is already present. Small differences in the α_{10} spectra for TMG and TMSb exposure support this, indicating that the TMG-exposed surface is terminated with Ga and the TMSb-exposed surface with Sb. That the growth surface is

also terminated by Sb appears to be consistent with the relative reactivities of TMG and TMSb as found from our <ε> data.

Post-deposition analyses by various means including XRD, TEM, SEM, Nomarski, AFM, and electrical-conductivity measurements supported the claim that we were able to grow good material both homoepitaxially and heteroepitaxially. The TEM micrographs showed a relatively narrow (1-2 nm) interface with relatively local dislocations and as a result a good continuation of the GaAs lattice planes into the heteroepitaxial material. One particularly important result was obtained by the electrical measurements, which showed that the heteroepitaxial material was n-type with a carrier concentration of 2×10^{16} cm^{-3}, which is essentially state-of-the-art and in particular shows that we were able to suppress essentially completely the formation of Ga antisite defects, which result in heavily p-type material. Finally, as an example of heterogeneous growth of a chemically mismatched system, we also report some results that we obtained for the growth of GaP on Si. The combination of a polar material on a nonpolar substrate represents another growth challenge, even with a lattice mismatch of only 0.5%, and we decided to take advantage of the time resolution provided by our system to gain some insight into the critical initial stages of growth. Our data reveal, not surprisingly, that the main problem in growing uniform layers of GaP on Si is the high mobility of Ga on the (most probably P-terminated) Si substrate, together with its passive character. Under standard growth conditions the Ga deposited by TMG decomposition essentially immediately forms well-separated islands. The ellipsometric data do not show these islands, but rather responds to the open spaces between. Thus under standard conditions no change appears to be happening in the ellipsometric data except for a gradual

reduction in beam intensity as the growing islands scatter more and more light out of the beam.

The key obviously was to get Ga to deposit more or less uniformly on the terraces, and we found SE to be ideal for this purpose. We found that we could obtain Ga deposition on the terraces if we (1) lowered the temperature as far as possible, (2) preroughened the growth surface on a microscopic scale, and (3) operated the OMCVD reactor in a "burst" mode, where a deliberately set imbalance between vent- and process-line pressures ensured that a large quantity of TMG would arrive at the growth surface in a time of the order of 1 s thereby flooding it with deposited Ga. The combination of (1) and (2) reduced Ga mobility on the surface and (3) increased the density of nucleation sites. Operation with the first deposition being done in a "burst" mode seems to be one way of increasing nucleation-site density, and is also recommended for future exploration.

In summary, our results provided the first insight into the nature of antimonide growth by OMCVD, here the homoepitaxy of GaSb, and indicated a possible way of improving GaP grown on Si. Future work will pursue these promising directions. The results also show that similarly good results will be obtained in investigations of the other low-bandgap materials, InAs and InSb.

Appendix

1. PSA calculation (Bench system)

From the intensity, we can express $\rho = \frac{r_p}{r_s}$ in terms of the relative coefficients α_2 and β_2 of $\cos 2\omega t$ and $\sin 2\omega t$, assuming A= ωt.

$$
\begin{aligned}
I &= |E_x|^2 \_ |E_y|^2 \\
&= E_x^* E_x + E_y^* E_y \\
&= |E_x|^2 \cdot |r_p \cos A \cos P + r_s \sin A \sin P|^2 \\
&= |E_x|^2 \cdot |r_p \cos \omega t \cos P + r_s \sin \omega t \sin P|^2 \\
&= |E_x|^2 (r_p \cos \omega t \cos P + r_s \sin \omega t \sin P)(r_p \cos \omega t \cos P + r_s \sin \omega t \sin P)^* \\
&= |E_x|^2 (r_p \cos \omega t \cos P + r_s \sin \omega t \sin P)(r_p^* \cos \omega t \cos P + r_s^* \sin \omega t \sin P) \\
&= |E_x|^2 \{r_p r_p^* (\cos \omega t \cos P)^2 + r_s r_s^* (\sin \omega t \sin P)^2 + r_p r_s^* \cos \omega t \cos P \sin \omega t \sin P \\
&+ r_s r_p^* \sin \omega t \sin P \cos \omega t \cos P\} \\
&= |E_x|^2 \{r_p r_p^* (\cos \omega t)^2 \cos^2 P + r_s r_s^* (\sin \omega t)^2 \sin^2 P + r_p r_s^* \sin \omega t \cos \omega t \cos P \sin P \\
&+ r_s r_p^* \sin \omega t \cos \omega t \sin P \cos P\} \\
&= |E_x|^2 [\{r_p r_p^* (\cos \omega t)^2 \cos^2 P + r_s r_s^* (\sin \omega t)^2 \sin^2 P] + \{(r_p r_s^*)(r_s r_p^*) \sin \omega t \cos \omega t \cos P \sin P\}]
\end{aligned}
$$

(1.1)

Since

$$\cos 2\omega t = (\cos \omega t)^2 - (\sin \omega t)^2.$$
$$\sin 2\omega t = 2 \sin \omega t \cos \omega t.$$
$$\cos 2\omega t = \cos(\omega t + \omega t) = \cos \omega t \cos \omega t - \sin \omega t \sin \omega t = (\cos \omega t)^2 - \left(1 - (\cos \omega t)^2\right).$$
$$\frac{1 + \cos 2\omega t}{2} = (\cos \omega t)^2 = \left(1 - (\sin \omega t)^2\right) - (\sin \omega t)^2 = 1 - 2(\sin \omega t)^2.$$
$$\frac{1 - \cos 2\omega t}{2} = (\sin \omega t)^2.$$
$$\sin 2\omega t = \sin(\omega t + \omega t) = \sin \omega t \cos \omega t + \cos \omega t \sin \omega t = 2 \sin \omega t \cos \omega t.$$
$$z = r_p r_s^{\,*} = a + iB, z^* = r_s r_p^{\,*} = a - ib.$$
$$z + z^* = 2a \operatorname{Re}(z).$$

Therefore (1.1) becomes

$$|E_x|^2 \left(|r_p|^2 \frac{1 + \cos 2\omega t}{2} \cos^2 P + |r_s|^2 \frac{1 - \cos 2\omega t}{2} \sin^2 P + 2 \operatorname{Re} r_p r_s \sin A \cos A \sin P \cos P \right) \tag{1.2}$$

Since

$$\sin \omega t \cos \omega t = \frac{1}{2} \sin^2 \omega t.$$
$$\sin 2P = \sin(P + P) = \sin P \cos P + \cos P \sin P = 2 \sin P \cos P.$$
$$\sin P \cos P = \frac{1}{2} \sin^2 P.$$

Therefore (1.2)

$$
\begin{aligned}
&|E_x|^2\left(|r_p|^2\frac{1+\cos 2\omega t}{2}\cos^2 P+|r_s|^2\frac{1-\cos 2\omega t}{2}\sin^2 P+2\,\mathrm{Re}\frac{1}{2}\sin 2\omega t\frac{1}{2}\sin 2P\right)\\
&=\frac{1}{2}|E_x|^2\left(|r_p|^2(1+\cos 2\omega t)\cos^2 P+|r_s|^2(1-\cos 2\omega t)\sin^2 P+2\,\mathrm{Re}\frac{1}{2}\sin 2\omega t\frac{1}{2}\sin 2P\right)\\
&=\frac{1}{2}|E_x|^2\left(|r_p|^2\cos^2 P+|r_s|^2\sin^2 P\right)\{1+\frac{|r_p|^2\cos^2 P-|r_s|^2\sin^2 P}{|r_p|^2\cos^2 P+|r_s|^2\sin^2 P}\cos\omega t\\
&+\frac{\mathrm{Re}\left(r_p r_s^*\right)\sin 2P}{|r_p|^2\cos^2 P+|r_s|^2\sin^2 P}\sin\omega t).
\end{aligned}
\tag{1.3}
$$

Since

$$
\alpha_2=\frac{|r_p|^2\cos^2 P-|r_s|^2\sin^2 P}{|r_p|^2\cos^2 P+|r_s|^2\sin^2 P},\beta_2=\frac{\mathrm{Re}\left(r_p r_s^*\right)\sin 2P}{|r_p|^2\cos^2 P+|r_s|^2\sin^2 P},
$$

$$
I_o=\frac{1}{2}|E_x|^2\left(|r_p|^2\cos^2 P+|r_s|^2\sin^2 P\right)
$$

Therefore (1.3) becomes

$$
\begin{aligned}
I&=I_0\left(1+\alpha_2\cos 2\omega t+\beta_2\sin 2\omega t\right)\\
&=I_o\left(1+\frac{\left|\frac{r_p}{r_s}\right|^2-\tan^2 P}{\left|\frac{r_p}{r_s}\right|^2+\tan^2 P}\cos 2\omega t+\frac{2\,\mathrm{Re}\left|\frac{r_p}{r_s}\right|+|\tan P|}{\left|\frac{r_p}{r_s}\right|^2+\tan^2 P}\sin 2\omega t\right)
\end{aligned}
\tag{1.4}
$$

Finally, we get

$$
\begin{aligned}
&|\rho|^2=\left|\frac{r_p}{r_s}\right|^2=\tan^2\Psi.\\
&\mathrm{Re}(\rho)=\tan\Psi\cos\Delta.\\
&\rho=\tan\Psi e^{i\Delta}
\end{aligned}
\tag{1.5}
$$

2. PSCA calculation (Non-rotating sample)

$$\begin{pmatrix} E'_x \\ E'_y \end{pmatrix} = \begin{pmatrix} 1 & 0 \\ 0 & 0 \end{pmatrix} \begin{pmatrix} \cos A & \sin A \\ -\sin A & \cos A \end{pmatrix} \begin{pmatrix} \cos C & -\sin C \\ \sin C & \cos C \end{pmatrix} \begin{pmatrix} 1 & 0 \\ 0 & e^{-i\delta} \end{pmatrix} \begin{pmatrix} \cos C & \sin C \\ -\sin C & \cos C \end{pmatrix} \begin{pmatrix} r_p & 0 \\ 0 & r_s \end{pmatrix} \begin{pmatrix} \cos P & -\sin P \\ \sin P & \cos P \end{pmatrix} \begin{pmatrix} 1 & 0 \\ 0 & 0 \end{pmatrix} \begin{pmatrix} E_x \\ E_y \end{pmatrix} \tag{2.1}$$

Step 1 (Analyzer)

$$\begin{bmatrix} 1 & 0 \\ 0 & 0 \end{bmatrix} \begin{bmatrix} \cos A & \sin A \\ -\sin A & \cos A \end{bmatrix} = \begin{bmatrix} \cos A & \sin A \\ 0 & 0 \end{bmatrix} \tag{2.2}$$

Step 2 (Rotation compensator)

$$\begin{bmatrix} \cos C & -\sin C \\ \sin C & \cos C \end{bmatrix} \begin{bmatrix} 1 & 0 \\ 0 & e^{-i\delta} \end{bmatrix} \begin{bmatrix} \cos C & \sin C \\ -\sin C & \cos C \end{bmatrix} = \begin{bmatrix} \cos^2 C + \sin^2 C e^{-i\delta} & \sin C \cos C - \sin C \cos C e^{-i\delta} \\ \sin C \cos C - \sin C \cos C e^{-i\delta} & \sin^2 C + \cos^2 C e^{-i\delta} \end{bmatrix} \tag{2.3}$$

Since

$\sin 2C = 2\sin C\cos C.$

Therefore

$$\sin C\cos C = \frac{1}{2}\sin 2C$$

and

$$\sin C\cos C - \sin C\cos Ce^{-i\delta} = \frac{1}{2}\sin 2C - \frac{1}{2}\sin 2Ce^{-i\delta} = \frac{1}{2}\sin 2C\left(1 - e^{-i\delta}\right)$$

Since

$$\cos^2 C = \frac{(1+\cos 2C)}{2}, \sin^2 C = \frac{(1-\cos 2C)}{2}$$

Therefore

$$\cos^2 2C = \frac{(1+\cos 4C)}{2}, \sin^2 2C = \frac{(1-\cos 4C)}{2}$$

Therefore Eq. (2.3) becomes

$$\frac{1}{2}\begin{bmatrix} (1+e^{-i\delta}) + \cos 2C(1-e^{-i\delta}) & \sin 2C(1-e^{-i\delta}) \\ \sin 2C(1-e^{-i\delta}) & (1+e^{-i\delta}) - \cos 2C(1-e^{-i\delta}) \end{bmatrix} \tag{2.4}$$

Step 3 (Sample & polarizer)

$$\begin{bmatrix} r_p & 0 \\ 0 & r_s \end{bmatrix}\begin{bmatrix} \cos P & -\sin P \\ \sin P & \cos P \end{bmatrix}\begin{bmatrix} 1 & 0 \\ 0 & 0 \end{bmatrix} = \begin{bmatrix} r_p \cos P & 0 \\ r_s \sin P & 0 \end{bmatrix} = \begin{bmatrix} R_p & 0 \\ R_s & 0 \end{bmatrix} \tag{2.5}$$

Step 4

Combine Eq(2.2), (2.4) ,and (2)

$$\frac{1}{2}\begin{bmatrix} \sin 2C(1-e^{-i\delta})(R_s\cos A + R_p \sin A) + (1+e^{-i\delta})(R_p\cos A + R_s \sin A) & 0 \\ +\cos 2C(1-e^{-i\delta})(R_p\cos A - R_s \sin A) & \\ 0 & 0 \end{bmatrix} \tag{2.6}$$

Therefore

$$E_x = \frac{1}{2}\begin{bmatrix} \sin 2C(1-e^{-i\delta})(R_s \cos A + R_p \sin A) + (1+e^{-i\delta})(R_p \cos A + R_s \sin A) & 0 \\ +\cos 2C(1-e^{-i\delta})(R_p \cos A - R_s \sin A) & \\ 0 & 0 \end{bmatrix} \quad (2.7)$$

$$
\begin{aligned}
&I = \left|E_x\right|^2 + \left|E_x\right|^2 = E_x \cdot E_x^{\,*} + E_y E_y^{\,*} = E_x \cdot E_x^{\,*} \\
&= \frac{1}{2}[\sin 2C(1-e^{-i\delta})(R_s \cos A + R_p \sin A) + (1+e^{-i\delta})(R_p \cos A + R_s \sin A) \\
&+ \cos 2C(1-e^{-i\delta})(R_p \cos A - R_s \sin A)] \\
&\cdot \frac{1}{2}[\sin 2C(1-e^{i\delta})(R_s^{\,*} \cos A + R_p^{\,*} \sin A) + (1+e^{i\delta})(R_p^{\,*} \cos A + R_s^{\,*} \sin A) \\
&+ \cos 2C(1-e^{i\delta})(R_p^{\,*} \cos A - R_s^{\,*} \sin A)] \\
&= \frac{1}{4}[(R_p \cos A + R_s \sin A)(R_p^{\,*} \cos A + R_s^{\,*} \sin A)(1+e^{-i\delta})(1+e^{i\delta}) \\
&+ \sin 2C(R_s \cos A + R_p \sin A)(R_p^{\,*} \cos A + R_s^{\,'*} \sin A)(1-e^{-i\delta})(1+e^{i\delta}) \\
&+ \sin 2C(R_p \cos A + R_s \sin A)(R_s^{\,*} \cos A + R_p^{\,*} \sin A)(1+e^{-i\delta})(1-e^{i\delta}) \\
&+ \sin^2 2C(R_s \cos A + R_p \sin A)(R_s^{\,*} \cos A + R_p^{\,*} \sin A)(1-e^{-i\delta})(1-e^{i\delta}) \\
&+ \cos^2 2C(R_p \cos A - R_s \sin A)(R_p^{\,*} \cos A - R_s^{\,*} \sin A)(1-e^{-i\delta})(1-e^{i\delta}) \\
&+ \sin 2C \cos 2C(R_p \cos A - R_s \sin A)(R_s^{\,*} \cos A + R_p^{\,*} \sin A)(1-e^{-i\delta})(1-e^{i\delta}) \\
&+ \sin 2C \cos 2C(R_s \cos A + R_p \sin A)(R_p^{\,*} \cos A - R_s^{\,*} \sin A)(1-e^{-i\delta})(1-e^{i\delta}) \\
&+ \cos 2C(R_p \cos A + R_s \sin A)(R_p^{\,*} \cos A - R_s^{\,*} \sin A)(1+e^{-i\delta})(1-e^{i\delta}) \\
&+ \cos 2C(R_p \cos A - R_s \sin A)(R_p^{\,*} \cos A + R_s^{\,*} \sin A)(1-e^{-i\delta})(1+e^{i\delta})] \\
&= \frac{1}{4}[\{(1+e^{-i\delta})(1+e^{i\delta})(R_p \cos A + R_s \sin A)(R_p^{\,*} \cos A + R_s^{\,*} \sin A) \\
&+ \frac{1}{2}(1-e^{-i\delta})(1-e^{i\delta})(R_p \cos A - R_s \sin A)(R_p^{\,*} \cos A - R_s^{\,*} \sin A) \\
&+ \frac{1}{2}(1-e^{-i\delta})(1-e^{i\delta})(R_s \cos A + R_p \sin A)(R_s^{\,*} \cos A + R_p^{\,*} \sin A)\} \\
&+ \cos 2C\{(1+e^{-i\delta})(1-e^{i\delta})(R_p \cos A + R_s \sin A)(R_p^{\,*} \cos A - R_s^{\,*} \sin A) \\
&+ (1-e^{-i\delta})(1+e^{i\delta})(R_p \cos A - R_s \sin A)(R_p^{\,*} \cos A + R_s^{\,*} \sin A)\} \\
&+ \sin 2C\{(1-e^{-i\delta})(1+e^{i\delta})(R_s \cos A + R_p \sin A)(R_p^{\,*} \cos A + R_s^{\,*} \sin A) \\
&+ (1+e^{-i\delta})(1-e^{i\delta})(R_p \cos A + R_s \sin A)(R_s^{\,*} \cos A + R_p^{\,*} \sin A)\} \\
&+ \frac{\cos 4C}{2}\{-(1-e^{-i\delta})(1-e^{i\delta})(R_s \cos A + R_p \sin A)(R_s^{\,*} \cos A + R_p^{\,*} \sin A) \\
&+ (1-e^{-i\delta})(1-e^{i\delta})(R_p \cos A - R_s \sin A)(R_p^{\,*} \cos A - R_s^{\,*} \sin A)\} \\
&+ \frac{\sin 4C}{2}\{(1-e^{-i\delta})(1-e^{i\delta})(R_p \cos A - R_s \sin A)(R_s^{\,*} \cos A + R_p^{\,*} \sin A) \\
&+ (1-e^{-i\delta})(1-e^{i\delta})(R_s \cos A + R_p \sin A)(R_p^{\,*} \cos A - R_s^{\,*} \sin A)\}]
\end{aligned}
\tag{2.8}
$$

I_{dc} Term

$$
\begin{aligned}
I_{dc} &= \frac{1}{4}[\{(2+2\cos\delta)(|R_p|^2\cos^2 A+|R_s|^2\sin^2 A+R_pR_s^*\sin A\cos A+\\
&R_sR_p^*\sin A\cos A)\}+\{\frac{1}{2}(2-2\cos\delta)(|R_p|^2\cos^2 A+|R_s|^2\sin^2 A\\
&-R_sR_p^*\sin A\cos A-R_pR_s^*\sin A\cos A\\
&+|R_p|^2\cos^2 A+|R_s|^2\sin^2 A+R_pR_s^*\sin A\cos A+R_sR_p^*\sin A\cos A\}]\\
&=\frac{1}{4}[\{(2+2\cos\delta)(|R_p|^2\cos^2 A+|R_s|^2\sin^2 A+2\,Re(R_pR_s^*)\sin A\cos A)\}\\
&+\{\frac{1}{2}(2-2\cos\delta)\cdot 2(|R_p|^2+|R_s|^2)\}]\\
&=\frac{1}{4}[\{2(1+\cos\delta)(|R_p|^2\cos^2 A+|R_s|^2\sin^2 A+\sin 2A\,Re(R_pR_s^*)\}\\
&+\{(1-\cos\delta)(|R_p|^2+|R_s|^2)\}]
\end{aligned}
\tag{2.9}
$$

α_2 Term

$$
\begin{aligned}
a_2 &= \frac{1}{4}\{2i\sin\delta(|R_p|^2\cos^2 A-|R_s|^2\sin^2 A+R_pR_s^*\sin A\cos A-R_sR_p^*\sin A\cos A\\
&-|R_p|^2\cos^2 A+|R_s|^2\sin^2 A-R_sR_p^*\sin A\cos A+R_pR_s^*\sin A\cos A)\}\\
&=\frac{1}{2}i\sin\delta\{(2R_pR_s^*\sin A\cos A-2R_sR_p^*\sin A\cos A)\}\\
&=-\sin\delta\sin 2A\,\mathrm{Im}(R_pR_s^*)
\end{aligned}
\tag{2.10}
$$

Therefore

$$
\alpha_2=\frac{a_2}{I_{dc}}=-\frac{\sin\delta\sin 2A\,\mathrm{Im}(R_pR_s^*)}{\frac{1}{4}[\{2(1+\cos\delta)(|R_p|^2\cos^2 A+|R_s|^2\sin^2 A+\sin 2A\,\mathrm{Re}(R_pR_s^*)\}+\{(1-\cos\delta)(|R_p|^2+|R_s|^2)\}]}
$$

(2.11)

β_2 Term

$$
\begin{aligned}
b_2 &= \frac{1}{4} 2i \sin\delta (\left|R_p\right|^2 \sin A\cos A + \left|R_s\right|^2 \sin A\cos A + R_s R_p{}^* \cos^2 A + R_p R_s{}^* \sin^2 A) \\
&- (\left|R_p\right|^2 \sin A\cos A + \left|R_s\right|^2 \sin A\cos A + R_p R_s{}^* \cos^2 A + R_s R_p{}^* \sin^2 A) \\
&= \frac{1}{4} 2i \sin\delta \{R_s R_p{}^* (\cos^2 A - \sin^2 A) + R_p R_s{}^* (\sin^2 A - \cos^2 A)\} \\
&= \frac{1}{2} i \sin\delta \{\cos 2A (R_s R_p{}^* - R_p R_s{}^*)\} \qquad (2.12) \\
&= \frac{1}{2} i^2 \sin\delta (\cos 2A 2 \operatorname{Im} R_s R_p{}^*) \\
&= -\sin\delta \cos 2A \operatorname{Im} R_s R_p{}^* \\
&= \sin\delta \cos 2A \operatorname{Im} R_p R_s{}^*
\end{aligned}
$$

Therefore

$$
\begin{aligned}
\beta_2 = \frac{-\sin\delta \cos 2A \operatorname{Im} R_s R_p{}^*}{\frac{1}{4}[\{2(1+\cos\delta)(\left|R_p\right|^2 \cos^2 A + \left|R_s\right|^2 \sin^2 A + \sin 2A \operatorname{Re}(R_p R_s{}^*)\} \\
+ \{(1-\cos\delta)(\left|R_p\right|^2 + \left|R_s\right|^2)\}]}
\end{aligned}
\qquad (2.13)
$$

α_4 Term

$$
\begin{aligned}
a_4 &= \frac{1}{4}\cdot\frac{1}{2}\{\,2(1-\cos\delta)(-|R_p|^2\sin^2 A-|R_s|^2\cos^2 A-R_pR_s^{*}\sin A\cos A \\
&-R_sR_p^{*}\sin A\cos A+|R_p|^2\cos^2 A+|R_s|^2\sin^2 A-R_sR_p^{*}\sin A\cos A \\
&-R_pR_s^{*}\sin A\cos A)\} \\
&=\frac{1}{4}(1-\cos\delta)\{|R_p|^2(\cos^2 A-\sin^2 A)+|R_s|^2(\sin^2 A-\cos^2 A) \\
&-(2R_pR_s^{*}\sin A\cos A+2R_sR_p^{*}\sin A\cos A)\} \\
&=\frac{1}{4}(1-\cos\delta)(|R_p|^2\cos 2A-|R_s|^2\cos 2A-2\,Re\,R_pR_s^{*}\sin 2A) \\
&=\frac{1}{4}(1-\cos\delta)\{\cos 2A(|R_p|^2-|R_s|^2)-2\,Re\,R_pR_s^{*}\sin 2A\}
\end{aligned}
\tag{2.14}
$$

Therefore

$$
\begin{aligned}
\alpha_4 = \frac{(1-\cos\delta)\{\cos 2A(|R_p|^2-|R_s|^2)-2\,\mathrm{Re}\,R_pR_s^{*}\sin 2A\}}{\{2(1+\cos\delta)(|R_p|^2\cos^2 A+|R_s|^2\sin^2 A+\sin 2A\,\mathrm{Re}(R_pR_s^{*})\}} \\
+\{(1-\cos\delta)(|R_p|^2+|R_s|^2)\}
\end{aligned}
\tag{2.15}
$$

β_4 Term

$$
\begin{aligned}
b_4 &= \frac{1}{4}[\{(1-\cos\delta)(|R_p|^2 \sin A\cos A - |R_s|^2 \sin\cos A \\
&+ R_p R_s^{*} \cos^2 A - R_s R_p^{*} \sin^2 A)\} \\
&+ \{(1-\cos\delta)(|R_p|^2 \sin A\cos A - |R_s|^2 \sin\cos A - R_p R_s^{*} \sin^2 A + R_s R_p^{*} \cos^2 A)\}] \\
&= \frac{1}{4}(1-\cos\delta)(2|R_p|^2 \sin A\cos A - 2|R_s|^2 \sin A\cos A \\
&+ \cos^2 A(R_p R_s^{*} + R_s R_p^{*}) - \sin^2 A(R_s R_p^{*} + R_p R_s^{*}) \\
&= \frac{1}{4}(1-\cos\delta)(\sin 2A|R_p|^2 - \sin 2A|R_s|^2 + 2\,Re(R_p R_s^{*})(\cos^2 A - \sin^2 A) \\
&= \frac{1}{4}(1-\cos\delta)(\sin 2A|R_p|^2 - \sin 2A|R_s|^2 + 2\,Re(R_p R_s^{*})\cos 2A \\
&= \frac{1}{4}(1-\cos\delta)\{(|R_p|^2 - |R_s|^2)\sin 2A + 2\,Re(R_p R_s^{*})\cos 2A\}
\end{aligned}
$$

(2.16)

Therefore

$$
\beta_4 = \frac{(1-\cos\delta)\{(|R_p|^2 - |R_s|^2)\sin 2A + 2\,\mathrm{Re}(R_p R_s^{*})\cos 2A\}}{\{2(1+\cos\delta)(|R_p|^2\cos^2 A + |R_s|^2 \sin^2 A + \sin 2A\,\mathrm{Re}(R_p R_s^{*})\} + \{(1-\cos\delta)(|R_p|^2 + |R_s|^2)\}} \tag{2.17}
$$

Therefore

$$
I = I_{dc}(1 + \alpha_2 \cos 2c + \beta_2 \sin 2C + \alpha_4 \cos 4C + \beta_4 \sin 4C) \tag{2.18}
$$

References

1I.Kamiya, D.E.Aspnes, L.T.Flores and J.T.Harbison, Phys. Rev.B, 1992. **46**(15): p. 859.

2D.E.Aspnes, Phys.Stat.Sol.(a), 2001(4): p. 1353-1360.

3J.T.Zettler, M.Pristovsek, T.Trepk, A.Shkrebtii, E.Steimetz, M.Zorn and W.Richter, Thin Solid Films, 1998(313): p. 537.

4D.E.Aspnes, W.E.Quinn and S.Gregory, Appl.Phys.Lett, 1990(57): p. 2707.

5D.E.Aspnes, W.E.Quinn, MC.Tamargo, M.A.Pudensi, S.A.Schwarz, M.J.S.P.Brazil and S.Gregory, Appl.Phys.Lett, 1992(60): p. 1244.

6C.H.Kuo, M.D.Boonzaayer, M.F.DeHerrera, D.K.Schroder, G.N.Maracas and B.Johs, J.Cryst.Growth, 1997. **170**: p. 281.

7G.N.Maracas, C.H.Kuo, S.Anand, R.Droopad, C.R.L.Sohie and T.Levola, J.Vac.Sci.Technol.A, 1995(13): p. 727.

8B.Johs, D.Doerr and S.Pittal, Thin Solid Films, 1993(233): p. 293.

9A.Aardvark, N.J.Mason and P.J.Walker, Prog.Crystal and Growh Charact, 1997. **35**(2-4): p. 207-241.

10A.G.Milnes and A.Y.Polakov, Solid-State Electron., 1993(36): p. 803.

11A.Subekti and E.M.Goldys, Phys.Chem.Solids, 2000(61): p. 537-544.

12C.A.Wang, S.Salim, K.F.Jensen and A.C.Jones, J.Cryst.Growth, 1997. **170**: p. 55-60.

13C.H.Chen, C.T.Chiu, L.C.Su, K.T.Huang, J.Shin and G.B.Stringfellow, J.Electron.Mater., 1993(22): p. 87.

14C.V.Eichelstreiber, M.Behet, M.Heuken and K.Heime, J.Cryst.Growth, 1997. **170**: p. 783-787.

15K.Hjelt and I.Tuomi, J.Cryst.Growth, 1997. **170**: p. 794-798.

16K.Moller, Z.Kollonitsch, Ch.Giesen, M.Heuken, F.Willig and T.Hannappel, J.Cryst.Growth, 2003. **248**: p. 244-248.

17F.Dimroth, C.Agert and A.W.Bett, J.Cryst.Growth, 2003. **248**: p. 265-273.

18R.M.Biefeld, Mat.Sci.and Eng., 2002. **R36**: p. 105-142.

19P.S.Dutta and H.N.Bhat, J.Appl.Phys., 1997. **81**(9): p. 5821-5870.

20F.S.Juang and Y.K.Su, Prog.Crystal and Growh Charact, 1990. **20**: p. 285-312.

21A.W.Bett and O.V.Sulima, Semicon.Sci.Technol., 2003. **18**: p. S184-S190.

22R.M.Biefeld, Mat.Sci.and Eng., 2002(R36): p. 105-142.

23O.J.Pitts, S.P.Watkins, C.X.Wang, J.A.H.Stotz and M.L.W.Thewalt, J.Electron.Mater., 2001. **30**(11): p. 1412-1416.

24G.B.Stringfellow, *Organometallic Vapor-Phase Epitaxy*. 2nd ed. 1999, New York: Academic Press.

25S.K.Haywood, A.B.Henriques, N.J.Mason, R.J.Nicholas and P.J.Walker, Semicon.Sci.Technol., 1988(3): p. 315-320.

26G.Muller, J.Cryst.Growth, 1990. **99**: p. 12-42.

27W.G.Breiland, M.E.Coltrin, J.Randall, H.Q.Hou, H.K.Moffat and J.Y.Tsao, Mat.Sci.and Eng., 1999(R24): p. 241-274.

28R.L.Moon, J. Cryst.Growth, 1997(170): p. 1-10.

29D.R.Olander, J.Heat Transfer,Trans.ASME, 1962(84): p. 185.

30I.A.Frolov, P.B.Boldyrevski, B.Druz and E.B.Sokolov, Inorg.Mater., 1977(13): p. 632.

31D.E.Aspnes, J.P.Harbison, A.A.Studna, L.T.Florez and M.K.Kelly, J.Vac.Sci.Technol.A, 1998(6): p. 1237.

32J.T.Zettler, Prog.Crystal and Growth Charact., 1997. **35**.

33D.E.Aspnes, J.Vac.Sci.Technol.B, 1985. **3**(5): p. 1498-1506.

34J.Kinsky, C.Schultz, D.Pahlke, A.M.Frisch, T.Herrmann, N.Esser and W.Ritcher, Appl.Surf.Sci., 1998(228): p. 123-124.

35E.Colas, D.E.Aspnes, R.Bhat, A.A.Studna, J.P.Harbison, L.T.Florez, M.A.Koza and V.G.Keramidas, J.Cryst.Growth, 1991.

36P.Y.Yu and M.Cardona, Fundamentals of Semiconductor: Physics and Materials Properties,Sringer,Berlin, 1996.

37D.E.Aspnes and A.A.Stunda, Phys. Rev.B, 1983. **27**(2): p. 985-1009.

38R.M.A.Azzam and N.M.Bashara, Ellipsometry and Polarized Light, 1987.

39B.O.Seraphin and H.E.Bennett, *Optical Properties of III-V Compound, edited by R.K.Willardson,A.C.Beer.* 1967: p. 93.

40B.R.Bennett, B.V.Shanabrook, P.M.Thibado, L.J.Whitman and R.Magno, J.Cryst.Growth, 1997. **175-176**: p. 888-893.

41J.R.Chelikowsky and M.L.Cohen, Phys. Rev.B, 1976. **14**: p. 556.

42M.Cardona, *Modulation Spectrosopy*. Vol. 11. 1969, New York: Academic Press.

43D.E.Aspnes, Physica B, 1983. **117-118**: p. 359-361.

44J.X. C. Herzinger B. Johs, D.Doctor,K. Elloit, G. Olson, D. Chow, J. Roth, I.T.Ferguson, M. Pelezynski, C.H. Kuo,and S. Johnson, MRS Proceedings, 1998(502): p. 3.

45D.E.Aspnes, Electronics and Optics, 1982. **89**: p. 249-262.

46D.E.Aspnes, Surf.Sci., 1994(307-309): p. 1017.

47C.R.Abernathy, Mat.Sci.and Eng., 1995(R14): p. 203-254.

48B.Johs, J.X.C.Herzinger, D.Doctor, K.Elliot, G.Olson, D.Chow, J.Roth, I.T.Ferguson, M.Pelezynski, Ch.Kuo and S.Johnson, MRS Proceedings, 1998. **502**: p. 3.

49G.B.Stringfellow, Reports on Progress in Physics, 1982(45): p. 469.

50J.R.Arthur, Structure and Chemistry of Solid Surfaces, 1969.

51A.Y.Cho, J.Appl.Phys., 1970(41): p. 2780.

52J.N.Baillargeon, A.Y.Cho, R.J.Pearah and K.Y.Cheng, J.Vac.Sci.Technol.B, 1994(12): p. 1106.

53D.J.Mobray, O.P.Kowalski, M.S.Skolnick, M.C.Hopkinson, J.P.David and A.G.Cullus, J.Appl.Phys., 1994(75): p. 2029.

54G.B.Stringfellow, J.Cryst.Growth, 1984. **70**: p. 133-139.

55J.A.Venables, G.D.T.Spiller and M.Hanbucken, Rep.Prog.Phys., 1984. **47**: p. 399-459.

56D.Hill and D.J.Bacon, Introduction to Dislocation, 1997: p. 18.

57D.Hill and D.J.Bacon, Introduction to Dislocation, 1997: p. 50.

58J.D.Weeks and G.H.Gilmer, Adv.Chem.Phys., 1979(40): p. 357-405.

59M.Ichimura, K.Higuchi, Y.Hattori and T.Wada, J.Appl.Phys., 1990. **68**(12): p. 6153-6158.

60J.A.Van Vechten, J.Electrochem.Soc., 1975. **122**: p. 423.

61V.A.Shchukin and D.Bimberg, Rev.Mordern Phys., 1999. **71**(4): p. 1125-1171.

62C.A.Swenson, J.Phys.Chem.Ref.Data, 1983. **12**(2): p. 179.

63D.L.Smith, Thi Film Deposition, 1997: p. 46.

64W.L.Sarney, L.Salamanca-Riba, J.D.Bruno and R.L.Tober, J.Cryst.Growth, 2002. **46**: p. 1643-1649.

65G.K.White and M.I.Minges, Thermophysical properties of Some Key Solids, 1985.

66M.Okaji, Int.J.Thermophys., 1988. **9**(96): p. 1101.

67G.W.Iseler, J.Cryst.Growth, 1977. **41**: p. 146.

68H.G.Bruhle, H.Neumann and G.Kuhn, Solid State Commun., 1980(34): p. 225.

69N.Yamanoto, H.Horinaka and T.Miyauchi, Jap.J.Appl.Phys., 1997. **225**(18).

70V.Kumar and B.S.R.Sastry, Cryst.Res.Technol., 2001. **36**(6): p. 565-569.

71J.Han, M.H.Crawford, R.J.Shul, S.J.Hearne, E.Chason, J.J.Fiegiel and M.Banas, MRS Internet J.Nitride Semicond.Res.4S1.G7.7, 1999.

72T.Wang, N.Moll, K.Cho and J.D.Joannpoulos, Phys.Rev.Lett., 1999. **82**(16): p. 3304-3307.

73D.C.Tran, G.H.Siegel and B.Bendow, Lightwave Tech.LT2536, 1984(226): p. 663.

74A.Subekti, E.M.Goldys and T.L.Tansley, J.Phys.and Chem.Sol., 2000(61): p. 537-544.

75J.Y.Tsao, J.Cryst.Growth, 1991. **110**: p. 595.

76Y.Dong, D.W.Scott, Y.Wei, A.C.Gossard and M.J.Rodwell, J.Cryst.Growth, 2003. **256**: p. 223-229.

77D.Dobosz, Z.R.Zytkiewicz, E.Papis, E.Kaminska and A.Piotrowska, J.Cryst.Growth, 2003. **253**: p. 102-106.

78A.S.Bracker, M.J.Yang, B.R.Bennett, J.C.Culbertson and W.J.Moore, J.Cryst.Growth, 2000. **220**: p. 384-392.

79B.Z.Nosho, B.R.Bennett, E.H.Aifer and M.Goldenberg, J.Cryst.Growth, 2002. **236**: p. 155-164.

80E.Hall and H.Kroemer, J.Cryst.Growth, 1999. **203**: p. 297-301.

81R.Grey, F.Mansoor, S.K.Haywood, N.J.Mason G.Hill and P.J.Walker, Optical Materials, 1996. **6**: p. 69-74.

82D.A.Allwood, N.J.Mason and P.J.Walker, J.Cryst.Growth, 1998. **195**: p. 163-167.

83C.Goletti, U.Resch-Esser, J.Foeller, N.Esser, W.Richter, B.Brar and H.Kroemer, Surf.Sci., 1996. **352-354**: p. 771-775.

84R.M.Graham., A.C.Jones, N.J.Mason, S.Rushworth, A.Salesse, T.Y.Seong, G.Booker, L.Smith and P.J.Walker, Semicon.Sci.Technol., 1993(8): p. 1797-1802.

85Motlan, E.M.Goldys and T.L.Tansley, J.Cryst.Growth, 2002. **236**: p. 621-626.

86O.J.Pitts, S.P.Watkins, C.X.Wang, V.Fik and K.L.Kavanagh, J.Cryst.Growth, 2003. **254**: p. 28-34.

87C.J.Vineis, C.A.Wang, K.F.Jensen and W.G.Breiland, J.Cryst.Growth, 1998. **195**: p. 181-186.

88H.M.Manasevit and K.L.Hess, J.Electrochem., 1979(126): p. 2031.

89C.B.Cooper, R.R.Saxena and M.J.Ludowise, J.Electron.Mater., 1995(24): p. 1563.

90R.J.Menna, D.R.Capewell, R.U.Martinelli, W.Ayers, R.Moulton, J.Palmer and G.Olsen, J.Cryst.Growth, 1994. **141**: p. 310-313.

91C.H.Chen, C.T.Chiu, L.C.Su, K.T.Huang, J.Shin and G.B.Stringfellow, J.Cryst.Growth, 1992. **124**: p. 142.

92I.A.Sheka, I.S.Chaus and T.T.Mityureva, *The Chemistry of Gallium*. 1966: Elsevier Publishing Company.

93J.R.Durig and K.K.Chatterjee, J.Ramann Spectr., 1981(11): p. 168.

94C.W.Bock and M.Trachtman, J.Cryst.Growth, 1994. **141**: p. 95.

95M.Trachtman, S.Beede and C.W.Bock, J.Phys.Chem., 1995(99): p. 15028.

96M.Tirtowidjojo and R.Pollard, J.Cryst.Growth, 1988. **93**: p. 108-114.

97M. Norishita S. Oikawa. M.Tsuda, M.Mashita,and Y. Kuniya., J.Cryst.Growth., 1998. **93**(93): p. 471.

98H.Tanaka and J.Komeno, J.Cryst.Growth, 1988. **93**: p. 116.

99S.Oikawa, M.Tsuda, M.Norishita, M.Mashita and Y.Kuniya, J.Cryst.Growth, 1998. **183**: p. 471.

100R.E.Winters and R..W.Kser, J.Organometal.Chem., 1967. **10**(7-14).

101T.L.Cottrell, The strengths of chemical bonds, Butterworths, London,2nd ed.,, 1958.

102A.Subekti, M.J.Peterson, E.M.Goldys and T.L.Tansley, Appl.Surf.Sci., 1999(140): p. 190-196.

103K.Flock, Ph.D Thesis, 2003.

104S.D.Hersee and J.M.Ballingall, J.Vac.Sci.Technol.A, 1990(8): p. 800.

105D.R.Lide (Editor in Chief), *Handbook of Chemistry and Physics*. 2001-2002: CRC Press, Boca Raton/New York, 82nd edition.

106Manufacturer, Shipley, 2002.

107R.Luckerath, P.Tommack, A.Hertling, H.J.Koss, P.Balk and K.F.Jesen, J.Cryst.Growth, 1988. **93**: p. 151-158.

108C.E.M.Campos and P.S.Pizani, Appl.Surf.Sci., 2002. **200**: p. 111-116.

109G.E. Franklin, A.Samsavar D.H.Rich, E.S.Hirschorn and F.M.Leibsle, Phys. Rev.B, 1990. **41**: p. 12619-12627.

110K.M.Schirm, P.Soukiassian, P.S.Mangat, Z.Hurych, L.Soonckindt and J.J.Bonnet, J.Vac.Sci.Technol.B, 1992. **10**: p. 1867.

111M.Levinshtein, S.Rumyantsev and M.Shur, *Handbook Series on Semiconductor Parameters*. Vol. 1. 1996.

112M.Patrini, G.Guizzetti, M.Galli, R.Ferrini, A.Bosacchi, S.Franchi and R.Magnanini, Solid State Commun., 1997. **101**(2): p. 93-98.

113R.M.Graham., A.C.Jones, N.J.Mason, S.Rushworth, L.Smith and P.J.Walker, J.Cryst.Growth, 1994. **145**: p. 363-370.

114Y.Nabetani, T.Ishikawa, S.Noda and A.Sasaki, J.Appl.Phys., 1994(76): p. 347.

115M.D.Pashley, K.W.Haberern, W.Friday, J.M.Woodall and P.D.kirchner, Phys.Rev.Lett., 1988. **60**: p. 2176.

116Y.Oda, N.Watanabe, H.Yokoyama and T.Kobayashi, Appl.Surf.Sci., 2003. **216**: p. 532-536.

117J.C.Bailar, H.J.Emeleus, Sir R.Nyholm and A.F.T-Dickenson, *Comprehensive Inorganic Chemistry*. 1973, New York: Pergamon Press.

118D.S.Cao, Z.M.Fang and G.B.Stringfellow, J.Cryst.Growth, 1991. **113**: p. 441-448.

119M.J.Cherng, G.B.Stringfellow and R.M.Cohen, Appl.Phys.Lett, 1984. **44**: p. 677.